Electrochemical Hydrogen Absorption by Zr-Cu-Al-Ni Metallic Glasses

DISSERTATION

Zur Erlangung des akademischen Grades

Doctor rerum naturalium
(Dr. rer. nat.)

vorgelegt

der Fakulität Mathematik und Naturwissenschaften
der Technischen Universität Dresden

von
M. Sc. Nahla Ismail Abdel Salam
geboren am 17. 11. 1969 in Kairo - Ägypten

Gutachter : **Prof. Dr. W. Plieth**
Prof. Dr. L. Schultz
Prof. Dr. S. Mostafa

Tag der Einreichung : 13.02.2002
Tag der Verteidigung : 10.06.2002

Contents

List of symbols

AES	Auger Electron Spectroscopy
α	Expansion coefficient [K^{-1}]
BGMs	Bulk Metallic Glasses
CBMS	Chill Block Melt Spinning
CCT	Continuous Cooling Transformation
C_p	Specific heat [J/K]
C_0	Hydrogen charge concentration at the sample surface [$\mathrm{mC/cm^2}$]
D_*	Diffusion coefficient [m^2/s]
ΔT_x	Undercooled liquid region ($\Delta T_x = T_x - T_g$) [K]
DSC	Differential Scanning Calorimetry
DTA	Differential Thermal Analysis
E_A	Activation energy of crystallisation [eV]
E_a	Hydrogen activation energy [$\mathrm{m^2K/s}$]
E_c	Cathodic potential [V]
EDX	Energy Dispersive X-Ray-Analysis
E'	Mixed potential [V]
E_n	Energy site
η	Polarisation potential [V]
ETM	Early Transition Metal
G	Gibbs free energy [J]
GFA	Glass Forming Ability
$\rho(\mathrm{r})$	Radial distribution function
H	Heat of enthalpy [J]
H_{abs}	absorbed hydrogen
H_{ads}	adsorbed hydrogen
$H_{2,ads}$	adsorbed molecular hydrogen
$(\mathrm{H_2O})_\mathrm{v}$	Water vapour
HER	Hydrogen Evolution Reaction
H/M	hydrogen to metal atomic ratio
i	Hydrogen-charging current density [$\mathrm{mA/cm^2}$]
i_a	Polarisation-anodic current density [$\mathrm{mA/cm^2}$]
i_c	Polarisation-cathodic current density [$\mathrm{mA/cm^2}$]
i_d	Transient current density from pulse test [$\mathrm{mA/cm^2}$]
$i_{l,c}$	Polarisation-limiting cathodic current density [$\mathrm{mA/cm^2}$]
I_n	Rate of homogeneous nucleation of a crystalline phase
i_o	Exchange current density [$\mathrm{mA/cm^2}$]
J	Flux density of the diffusing species [$\mathrm{m^3/s^2}$]
k_B	Boltzmann constant
Ln	Lanthanides
LTM	Late Transition Metals
MA	Mechanical Alloying
OCP	Open Circuit Potential [V]

P	Hydrogen pressure [MPa]
q_a	Anodic charge density [mC/cm^2]
R_c	Critical cooling rate [K/s]
RQ	Rapid Quenching
S	Entropy [J/K]
SCE	Saturated Calomel Electrode
SEM	Scanning Electron Microscopy
SQ	Slow Quenching
T	Absolute temperature [K]
t_b	Permeation test, break-through time [s]
t_c	Pulse test, cathodic charging time [s]
t_d	Pulse test, transient time [s]
TDA	Thermal Desorption Analysis
TEM	Transmission Electron Microscopy
T_g	Glass transition temperature [K]
T_m	Melting temperature [K]
TM	Transition Metals
TTT	Time Temperature Transformation
T_x	Crystallisation temperature [K]
XRD	X-Ray Diffraction
V	Volume [m^3]

Chapter 1

Introduction

In the last 40 years, the development of metastable alloys has attracted the attention of scientists and technologists since it is expected to exhibit interesting properties opening new fields of applications. Metastable materials are classified into three categories: amorphous materials characterised by a short range ordered atomic structure; nanocrystalline materials which have 100 nanometres grain diameter or less; certain quasicrystalline materials with the characteristic five-fold symmetry.

Amorphous alloys with a large variety of compositions provide atomic configurations which are different from those of crystalline alloys. These new atomic configurations yield various interesting properties such as good mechanical, interesting physical and unique chemical properties [1, 2, 3, 4]. Metallic glasses are amorphous alloys which are characterised by a glass transition and an undercooled liquid region before crystallisation.

Amorphous materials were first successfully produced in 1960, when Duwez prepared amorphous Au-Si alloys by rapid solidification [5]. Since then, preparation of various amorphous alloys has progressed. In the beginning, Fe-, Co- and Ni-based alloys were prepared followed by Pd- and Pt-based alloys [3]. In advance, much effort has been devoted to ease the conditions of preparing metallic glasses in bulk-shape. Inoue et al. reported new multicomponent ternary alloy systems for example, Mg-TM-Ln [6] (Ln= lanthanide metal; TM=transition metal), and Zr-TM-Al [7] which have a very high glass-forming ability (GFA) corresponding to a convenient critical cooling rate (R_c) for preparation from the melt. Further increase in the GFA and decrease of R_c were reached by developing quaternary amorphous alloys, e.g. based on Zr-TM-Al [8] such as $Zr_{55}Cu_{30}Al_{10}Ni_5$ and $Zr_{65}Cu_{17.5}Al_{7.5}Ni_{10}$ metallic glasses which allows the preparation of bulk amorphous alloys with thicknesses exceeding 10 mm. The progress of multicomponent systems opens the door for the development of quaternary and quinary alloys, easily shaped in different bulk forms [9, 10, 11, 12, 13].

Recently, in many studies the structural relaxation [14], phase transformation and crystallisation processes [14] of Zr-Cu-Ni-Al systems were investigated. Furthermore, the addition of oxygen to these systems was found to have a significant effect on the thermal stability [15], the crystallisation behaviour [16] and even on the preparation of the amorphous phase [15, 17].

It is almost impossible to produce alloys without any hydrogen, as it is formed or absorbed by many metallic materials during preparation, electro-chemical treatment or during corrosion. The presence of hydrogen in metals arises the problem of mechanical degradation, in other words "hydrogen embrittlement". Therefore, it is of great importance to study the effect of hydrogen in metals, such as hydrogen solubility and diffusivity [18, 19, 20, 21, 22]. Amorphous alloys consisting of a combination of early and late transition metals (ETM/LTM), for example binary Ni-Zr alloys, were found to be good hydrogen absorbers. This encouraged more detailed studies of the criteria for hydrogen absorption in amorphous alloys [23, 24, 25]. Hydrogen was used as a probe to explore the short range order atomic arrangement of metallic glasses. Investigations [26, 27, 28, 29] focused on Ni-Zr metallic glasses suggested that hydrogen atoms occupy successively tetrahedral interstitial sites. In fact, various investigations of hydrogen in Zr-based alloys have been progressed, yet most of them deal with the binary systems [30, 31, 32], some investigations deal with the ternary [33, 34] and only limited studies have been done on quaternary alloys [35]. It was noticed that hydrogen induces a phase separation in the Zr-Ni and Zr-Ni-Cu systems [32, 33], and also increases the electrical resistivity of the Zr-Ni system [36, 37]. Studies on the amorphous and quasicrystalline phase of Zr-Cu-Ni-Al system have reported that hydrogen is not fully desorbed from these systems and deteriorates its thermal stability [35, 38, 39].

Since the Zr-based alloys are good hydrogen absorbers, the aim of this work is to study the effect of electrochemically absorbed hydrogen on the stability of the amorphous phase of Zr-Cu-Al-Ni alloys, and on their thermal and crystallisation behaviours. The hydrogen reaction mechanism on the surface of the amorphous alloy is also investigated. Besides, the reversibility of the absorbed hydrogen and the mobility of hydrogen in melt-spun ribbons are studied.
In this work, different advanced techniques were used. Some of these techniques are applied to amorphous alloys for the first time to give information on the reversible and irreversible hydrogen absorption mode. The results of this work provide better understanding of hydrogen in quaternary Zr-based metallic glass systems.

Chapter 2

Theoretical background

2.1 Fundamentals of metallic glasses

2.1.1 Thermodynamics

The relative stability of a system at constant temperature and pressure is determined by its Gibbs free energy (G), which is defined by the well-known relation;

$$G = H - TS \tag{2.1}$$

Where H is the enthalpy, T is the absolute temperature, and S is the entropy of the system. From the thermodynamic point of view, a system changes until a stable equilibrium state is attained corresponding to the absolute minimum of G, or mathematically, $dG = 0$. According to equation 2.1 the highest stability, i.e. the lowest G, is attained at low enthalpy and/or high entropy depending on temperature.

The general definition of an equilibrium state is illustrated schematically in Fig. 2.1. For a given system with various possible atomic configurations, the stable equilibrium configuration (A) is the one where the Gibbs free energy curve has its absolute minimum. At this point small changes in the arrangement of atoms to a first approximation do not result in a change in G. However, other configurations like B, also correspond to a local minimum in the free energy curve with $dG = 0$. These configurations with a lower but only temporary stability are in a metastable equilibrium state, as they do not have the lowest possible value of G. The intermediate states for which $dG \neq 0$ are unstable. If the atoms are arranged in an intermediate state, for example as a result of thermal fluctuations, they will rapidly rearrange into one of the free energy minima. Sometimes, metastable states are very short-living, so transformations take place spontaneously, at other times they exist indefinitely, as shown in Fig. 2.1. The reason for this is the presence of the free energy 'hump' between the metastable and the stable states which must be overcome in order to transfer to the stable state. Kinetics obviously plays a central role in the study of transformation rates, so that, in general, higher 'humps' or energy barriers lead to slower transformation rates [40]. Crystalline materials are typically in a stable equilibrium state (configuration A), whereas amorphous materials, nanocrystalline materials, and most of the quasicrystalline materials are considered metastable (configuration B).

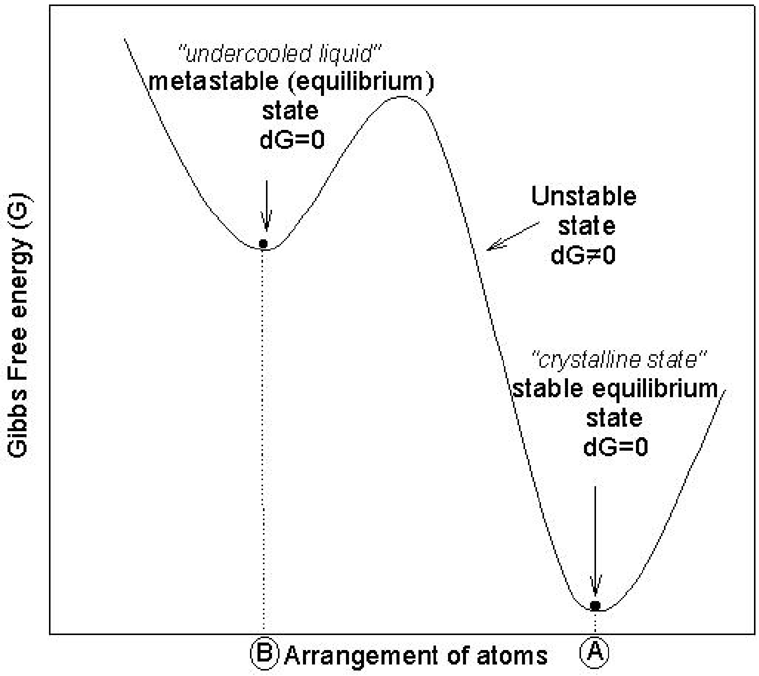

Figure 2.1: A schematic illustration of the variation of Gibbs free energy (G) with the arrangement of atoms in a material system [40]

2.1.2 The amorphous phase

The term "amorphous" is a greek expression meaning disordered. The atomic arrangement in an amorphous solid is schematically illustrated in Fig. 2.2 for a simple case that all atoms are of the same chemical species and the same size.

The radial distribution function ($\rho(r)$), obtained from X-ray or neutron diffraction measurements or NMR spectroscopy, gives information about the nearest and the next nearest neighbour atoms lying in a spherical coordination shell (shaded area in Fig. 2.2) around the considered atom (the black atom in Fig. 2.2). "r" is the vector between two atoms.

The diffraction pattern which results from measuring $\rho(r)$ is represented in the upper part of Fig. 2.2. The peak position gives information about the average distance between the regarded atom and the neighbouring atoms in a way that the first peak position resembles the nearest neighbour coordination shell, the second peak position corresponds to the second nearest neighbour shell and so on. The peak width gives information about the distribution (disorder) of the atoms lying in one coordination shell relative to the regarded atom. The peak area is related to the average number of atoms lying in a coordination shell, i.e. the average coordination number.

Obviously, there is a degree of regularity of arrangement of atoms around the regarded atom in the first coordination shell, and the degree of atomic disorder increases in the successive shells till the pattern displays a continuum. According to these results, the amorphous phase is considered not totally disordered but it exhibits a distinct *short-range order* structure [3, 41].

The amorphous structure can be described in terms of radial distribution function as :

$$g(r) = \sum_{R} \frac{nR}{n} \partial \left(r - R \right)$$

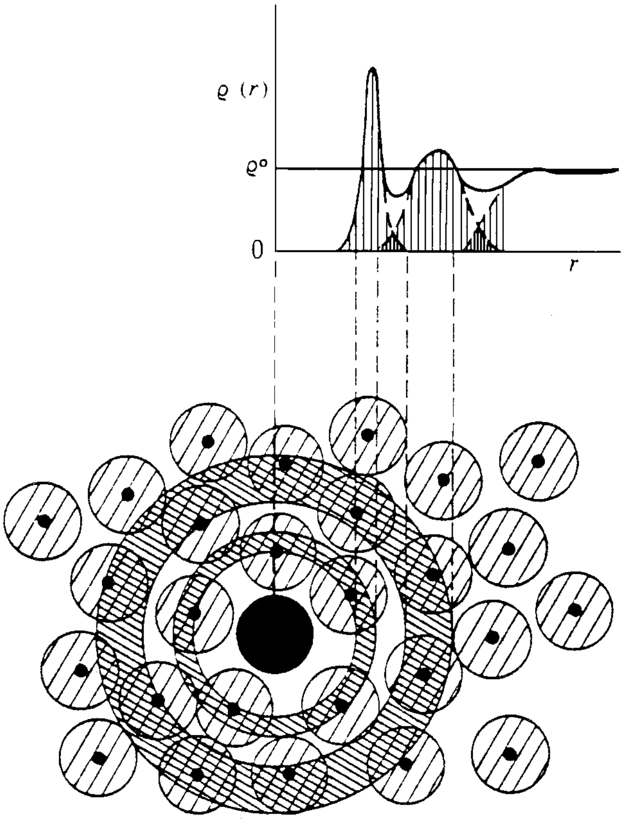

Figure 2.2: Schematic illustration of atomic arrangements in an amorphous solid and the corresponding radial distribution function ($\rho(r)$.)[41]

An amorphous phase can be formed by different methods. One of these methods is rapid solidification from the melt (see section 3.1). The kinetics of amorphous phase formation is explained by *time-temperature-transformation* (TTT) diagrams [42, 43] as shown in Fig. 2.3. TTT diagrams are constructed by isothermal annealing at various discrete temperatures measuring the elapsed time required to crystallise the material. A 'nose-shaped' curve is produced representing the crystalline phase formation. The time and the temperature at the tip of the nose correspond to the fastest rate of transformation. On the other hand, continuous cooling conditions yield *continuous cooling transformation* (CCT) diagrams. One example is represented by the dotted line in Fig. 2.3 [3, 43, 44]. This curve is constructed by cooling the melt at different cooling rates and measuring the elapsed time required for crystallisation for each cooling rate. From this curve it is possible to predict the necessary cooling rate required to produce amorphous material from the melt. The CCT curve will coincide with the TTT curve at one point and the lower part of the curve is not accessible by continuous cooling. Also, it is possible that if the cooling rate is high enough, the material won't crystallise. The lines of the TTT and the CCT curves typically correspond to a given fraction of crystallites, e.g. volume percent fraction.

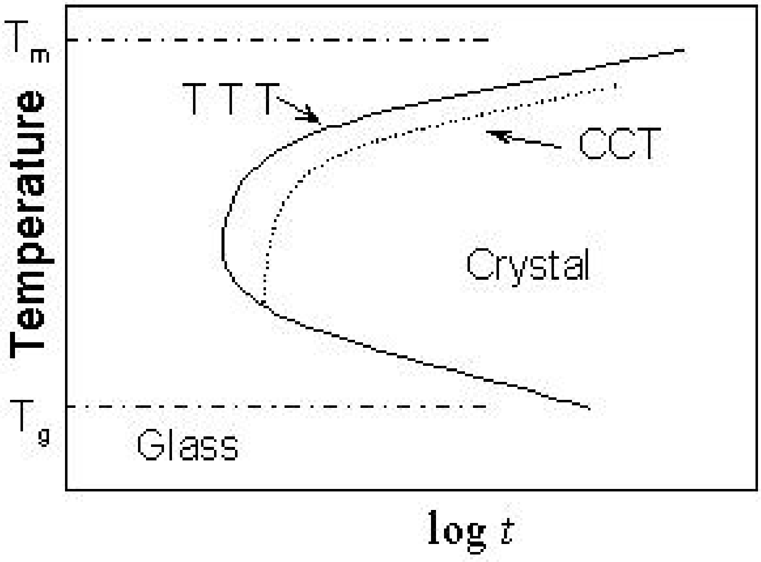

Figure 2.3: Schematic illustration of TTT and CCT diagrams [45].

2.1.3 Glasses and glass-forming ability

A glass is defined as an amorphous material, characterised by showing a glass transition upon heating and before crystallisation. Suppose a liquid has been cooled rapidly enough to prevent crystallisation, the cooling behaviour can be represented in terms of the change of first-order thermodynamic variables (volume V, enthalpy H, or entropy S).

The variation of volume with temperature upon cooling from the melt for amorphous and crystalline material is illustrated in Fig. 2.4. The dotted line represents the variation of volume with temperature due to crystalline phase formation, where a sharp sudden decrease in the melt volume occurs at the melting point temperature T_m. In comparison, the first order thermodynamic variable V exhibits a continuous change with temperature upon the formation of the amorphous phase. It shows a change of slope on the transition from liquid to glass. The *range* of temperature over which this transition takes place is called the glass transition (or transformation) temperature T_g. Second order variables, for example expansion coefficient $\alpha = \frac{1}{V}\left(\frac{\partial V}{\partial T}\right)$ or specific heat $C_p = (\frac{\partial H}{\partial T})_p$, change discontinuously at T_g (see bottom right insert to Fig. 2.4). Since T_g is not a sharply defined temperature but occurs over a range of temperatures, it is convenient to define T_g as a temperature at which the extrapolated liquid and glass lines intersect (see top left insert to Fig. 2.4). Furthermore, T_g depends on the rate of cooling, in a way that, for a fast cooling rate T_g' will take place at lower temperature than for a slow cooling rate T_g'' (see top left insert to Fig. 2.4). From the thermodynamic point of view, the glassy state is *unstable*, and when it is held at a temperature below T_g it will always tend to approach the metastable equilibrium state of the undercooled liquid. Calorimetric methods are used as standard

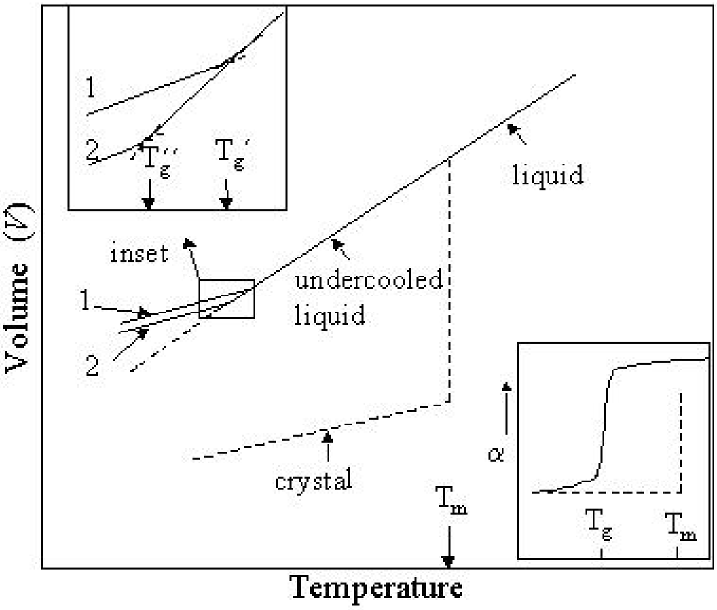

Figure 2.4: Schematic illustration of the change in volume with temperature through the glass-transition temperature[46]

methods to determine T_g, e.g. differential scanning calorimetry (DSC) offers a detailed study of the dependence of T_g on the heating rate and on the previous thermal history (see section 3.6.2).

In general, glass forming liquids tend to be either 'strong' or 'fragile' liquids. These labels refer to the ability of the liquid to withstand changes in the medium range order. Strong glass forming liquids, such as the covalent network materials, e.g. SiO_2 (strong bonding), are resistant to such change. On the other hand, fragile glass forming liquids are characterised by predominantly non-directional (ionic or Van der Waals') bonding, i.e. weak bonding, e.g. toluene [47, 48]. Viscosity measurements are used to distinguish between those two glass forming liquid types.

The development of three-dimensionally shaped glasses, i.e. alloy compositions with very high glass forming ability (GFA), has been an aim for scientists and technologists in order to produce "bulk metallic glasses" (BMGs) as engineering materials. The achievement of a system with a large GFA is proposed by Inoue [49] in three general empirical rules as follows :

(1) Multicomponent system consisting of more than three elements.

(2) Different atomic size ratio of more than 12% among the main three elements.

(3) Large negative heat of mixing among the main three elements.

These rules can be discussed in terms of thermodynamics, kinetics and structural point of views. From the *thermodynamical point of view*, a large GFA is obtained under the condition of low free energy $\Delta G(T)$ for the transformation from the liquid to the solid phase. Regarding the Gibbs free energy relation

$$\Delta G = \Delta H_f - T\Delta S_f \tag{2.2}$$

low ΔG values are obtained in case of low ΔH_f and large ΔS_f, where ΔH_f and ΔS_f are enthalpy and entropy of fusion, respectively. ΔS_f is expected to be large in multicomponent alloy systems. An increase in ΔS_f causes an increase in the degree of dense random packing which is also favourable for a decrease in ΔH_f and an increase in the solid/liquid interfacial energy. From the *kinetic point of view*, Turnbull [50] derived a relation between the rate of homogeneous nucleation of a crystalline phase (I_n) and the reduced temperature (T_g/T_m) as follows;

$$I_n = k/\eta \cdot exp\left[-b\alpha_n^3\beta_n/T_r\,(1-T_r)^2\right] \tag{2.3}$$

Where k is constant, η is the viscosity, b is a shape factor, α and β are dimensionless parameters, T_r=T_g/T_m is the reduced temperature. From this relation it was found that when $T_g/T_m \geq 0.6$, I_n is highly suppressed. While from the *structural point of view*, the presence of elements with significantly different atomic sizes (about 12%) in a multicomponent system which have large negative heats of mixing causes an increase of random packing density in the undercooled liquid. This leads to the achievement of a large liquid/solid interfacial energy. In addition, it increases the difficulty of an atomic arrangement of the constituent elements on a long range scale which, by their turn, suppress crystalline phase nucleation and crystal growth respectively [10, 49, 51]. The history of the development of amorphous alloys up to recently discovered BMGs is shown in Fig. 2.5. Earlier, amorphous Fe-, Co- and Ni- based alloys were prepared using cooling rates of $R_c > 10^4$ K/s leading to the production of amorphous samples with thicknesses around 0.1 mm. Then, Pd- and Pt-based alloys were produced at rates above 10^2 K/s [3] leading to amorphous samples with a maximum thickness of 1 mm. Further, efforts were focused on the developing of amorphous systems with convenient R_c, corresponding to a high GFA in order to facilitate the production of real bulk-shaped metallic glasses. In the 1990s, ternary alloys, e.g. Ln-Mg-TM [6], Ln-Al-TM [52] and Zr-Al-TM [7] systems were developed with R_c in the range from 10^2 to 10^3 K/s corresponding to $T_g/T_m \approx 0.6$ (see Fig. 2.5). Shortly after that, the quaternary and quinary alloys, e.g. Zr-Al-Cu-Ni [8] and Zr-Al-Co-Ni-Cu [53] were produced requiring a R_c in the range of only 1 to 10^2 K/s, therefore, it allows the preparation of bulk amorphous samples with diameters up to several centimeters by conventional casting techniques (see section 2.1.5). Furthermore, the multicomponent amorphous alloys exhibit high reduced glass transition temperatures ($T_g/T_m \geq 0.6$) according to Turnbull's equation [2.3]. Also, they show a relatively large difference ΔT_x between T_g and T_x up to more than 100 K upon heating ($\Delta T_x = T_x - T_g$), this is often named "supercooled liquid region". Those multicomponent systems have high GFA almost comparable to that of oxide glasses (see Fig. 2.5).

Fig. 2.6 illustrates the development in the progress in amorphous phase formation, which has lead to the development of BMG alloys. This figure illustrates schematic TTT diagrams, which show the shift of the "nose", i.e. the crystallisation nucleation curve, to more elapsed cooling time from fast quenching to slow cooling. The figure includes two solid arrow curves, illustrating the cooling during *rapid quenching* (RQ) at $\sim 10^6$ K/s and *slow quenching* (SQ at $\sim 10^2$ K/s. Curve (a) symbolizes the TTT diagram of the early glasses requiring RQ for preparation, in other words, high cooling rates. Further advance in the kinetics of the glass formation is revealed by curve (b) which symbolizes the preparation of glasses by SQ. Finally,

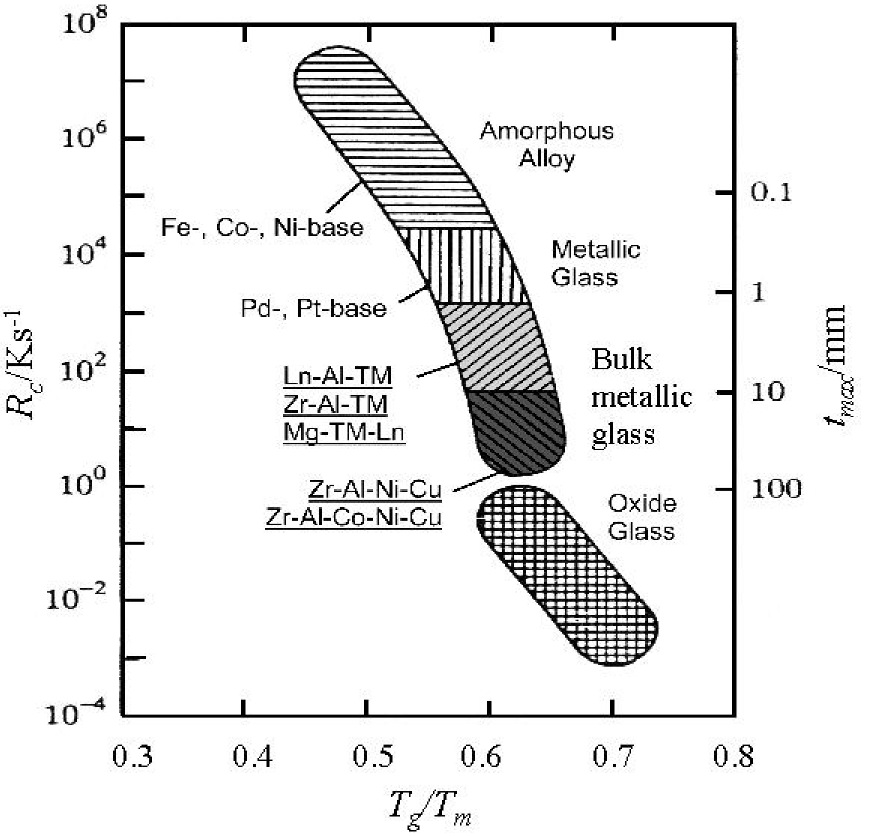

Figure 2.5: Relation between the critical cooling rate (R_c) for glass formation (left-Y-axis), the maximum sample thickness (t_{max}) (right-Y-axis) and the reduced glass transition temperature (T_g/T_m), the data of oxide glasses are shown for comparison[10].

curve (c) symbolizes the TTT diagram of BMGs formation at much lower cooling rates which are convenient for application [9].

2.1.4 Oxygen in Zr-based amorphous alloys

Detailed studies on the effect of small oxygen concentrations, less than 1 at.%, on phase formation and thermal stability of bulk $Zr_{55}Cu_{30}Al_{10}Ni_5$ and $Zr_{65}Cu_{17.5}Al_{7.5}Ni_{10}$ metallic glasses [15, 16, 17] revealed that oxygen influences drastically the thermal stability and the crystallisation mode of the amorphous $Zr_{65}Cu_{17.5}Al_{7.5}Ni_{10}$ alloy composition. However, it has no significant effect on the thermal stability and crystallisation mode of an amorphous $Zr_{55}Cu_{30}Al_{10}Ni_5$ alloy.

In the DSC scan of the $Zr_{55}Cu_{30}Al_{10}Ni_5$ alloy , (Fig. 2.7 [17]; at 40 K/min), oxygen leads to a small reduction of the undercooled liquid region (ΔT_x) so that the glass transition temperature T_g is slightly increased and the single sharp exothermic crystallisation peak shifts to lower temperature values and broadens.

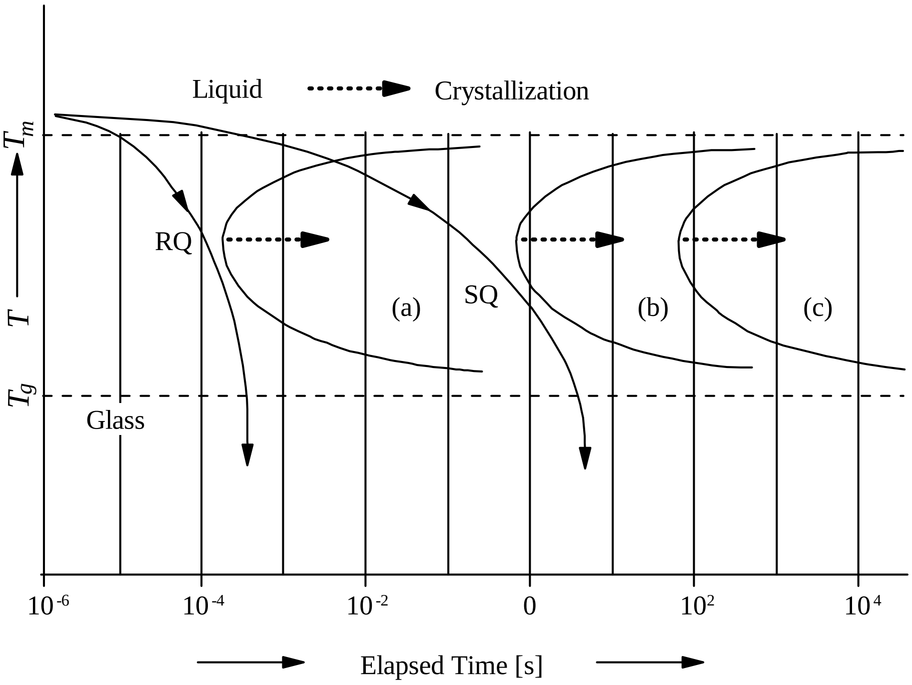

Figure 2.6: Schematic TTT diagrams comparing the crystallisation kinetics of (a) rapidly quenched, (b) slower quenched, and (c) bulk-glass-forming alloys [9].

On the other hand, the DSC scan of the $Zr_{65}Cu_{17.5}Al_{7.5}Ni_{10}$ alloy sample, shown in Fig. 2.7 [17], oxygen significantly reduces ΔT_x, this is mainly due to the splitting of the exothermic crystallisation peak to two peaks for a higher oxygen content which points to a change in the crystallisation sequence.

The first exothermic peak formed by the $Zr_{65}Cu_{17.5}Al_{7.5}Ni_{10}$ alloy is related to an oxygen-triggered nano-quasicrystalline phase and a $NiZr_2$-type f.c.c.-phase. The second exothermic peak is due to the subsequent transformation of these metastable phases to stable phases.

2.1.5 Methods of preparation of amorphous alloys

Various methods were developed to prepare amorphous alloys in different shapes and types, for example, as ribbons, bulk-shaped samples, powders or thin films. In principle, a high average sample quench rate can be achieved by promoting rapid heat removal from the bulk. This can be achieved by maximising the contact area between melt and cooling medium by rapidly increasing the liquid alloy surface area. In this section, some basic principles of these methods will be described which are used to fabricate different forms of amorphous alloys.

1. **Fabrication of amorphous ribbons**

    - **Melt spinning** is utilised for the fabrication of thin amorphous ribbons by bringing a stream of molten alloy in contact with a rapidly moving substrate, so that a pressurised orifice chill block melt spinning (CBMS) ejects the molten alloy [3, 46, 54]. The most common substrates are copper wheels. It is possible to control the ribbon width and thickness by controlling the orifice size and the distance between the orifice and the wheel. In this work, ribbons satisfy our experimental desires (see section 3.1).

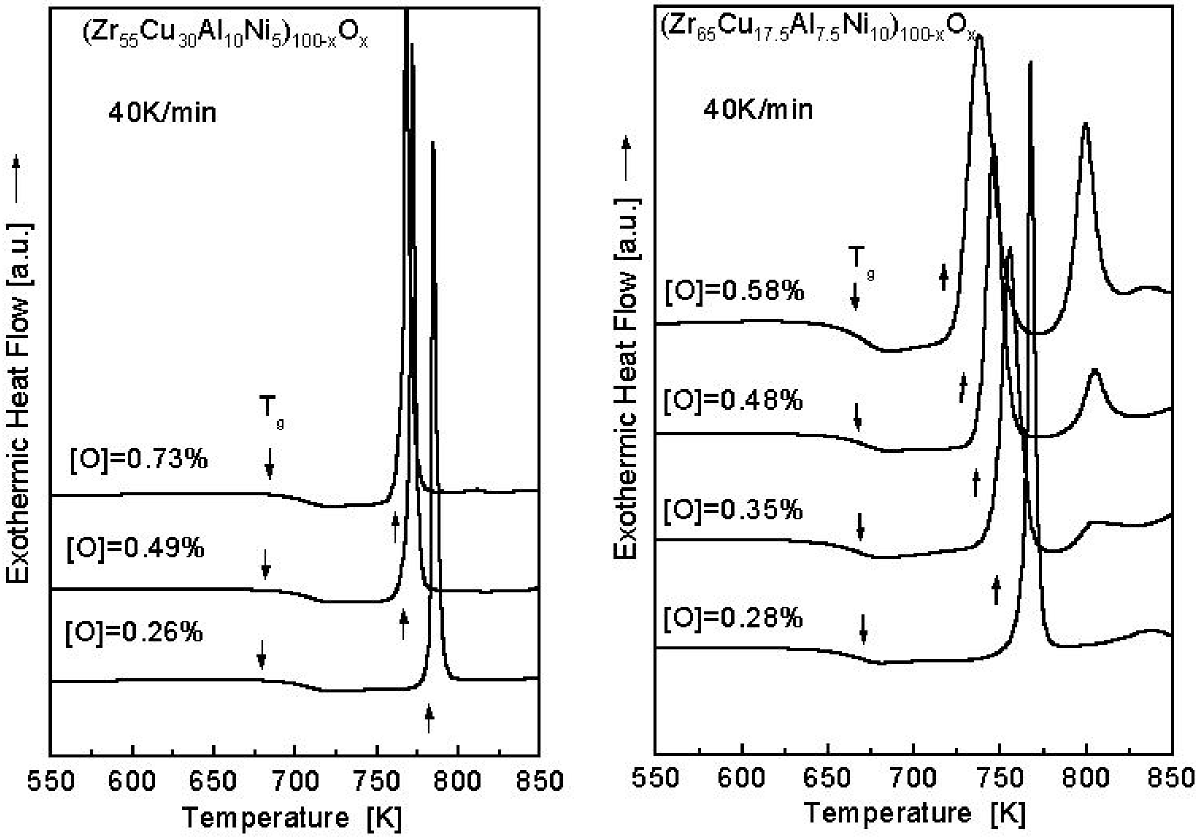

Figure 2.7: DSC scans (heating rate 40 K/min) for amorphous $(Zr_{55}Cu_{30}Al_{10}Ni_5)_{100-x}O_x$ and amorphous $(Zr_{65}Cu_{17.5}Al_{7.5}Ni_{10})_{100-x}O_x$ ribbons (x=oxygen content) [17].

- **Splat quenching** is a method which causes rapid flattening and quenching of a molten alloy droplet by squeezing between two low-temperature substrate surfaces, e.g. copper, diamond [55]. This method produces thin amorphous splats.

2. **Fabrication of amorphous powder**

   - **Gas atomisation and gas water atomisation** are used for production of amorphous powders. By *gas atomisation*, the molten alloy stream is atomised by a gas jet [3]. While by *gas-water atomisation*, the molten alloy droplets formed by gas atomisation are quenched in streams of high velocity water to produce finer particles [56].
   - **Mechanical alloying (MA)** is a solid state reaction process utilised to produce amorphous powder. MA is performed in a high-energy ball mill in an inert gas atmosphere, so that the master alloy powder particles are trapped by the colliding balls, heavily deformed and cold welded, leading to the formation of characteristically layered particles. Further milling refines the microstructure so that the refinement process is a logarithmic function of time. Finally, in many cases, a true alloying takes place via interdiffusion due to temperature rise by milling which favours the amorphous phase formation [57, 58, 59].

3. **Fabrication of bulk amorphous samples**

   - **Casting** the chill block melt spinning CBMS is also used to produce BMGs by die casting, so that the ejected melt is casted in to a cold copper mould instead of facing the rotating wheel. This method is successfully used to produce BMGs in various geometrical shapes.
   - **Mechanical alloying** can also be used to prepare BMGs in a way that the amorphous powder produced by MA is hot compressed in the undercooled liquid region [60].

4. **Fabrication of thin films**

   - **Sputtering and evaporation methods** [61] are used to produce amorphous films. A vapour steam of the sample condenses on a cold substrate. These are used if the alloy contains elements of high T_m and high chemical reactivity, e.g. rare earth elements [62].
   - **Chemical deposition and electrodeposition** are used to prepare various metal-metalloid amorphous films in a way that the metal–metalloid (e.g. phosphorus or boron) amorphous films are deposited from an electrolytic bath. By this method, it is possible to prepare thin films of 10-30 at.% phosphorus or boron [63].

2.2 Hydrogenation

2.2.1 Hydrogen electrode reactions

Hydrogen reactions on a solid surface can take place either from the gas phase, or by electrochemical cathodic reduction. Gas phase reactions are represented in the following equation array :

$$\mathrm{H_{2,g}} \rightleftharpoons \mathrm{H_{2,ads}} \rightleftharpoons \mathrm{2H_{ads}} \tag{2.4}$$

$$\mathrm{H_{ads}} \rightleftharpoons \mathrm{H_{abs}} \tag{2.5}$$

Adsorption of hydrogen from the gas phase is represented by reaction (2.4), so that a molecular hydrogen is adsorbed on the metal surface ($H_{2,ads}$), then dissociated to two adsorbed hydrogen atoms (H_{ads}). It is possible that two adsorbed atoms may recombine and desorb, this is resembled by the reverse of reaction (2.4). In case of solid material which has a high negative heat of solution of hydrogen, absorption of hydrogen may take place and H_{abs} diffuses into the bulk of the material, reaction (2.5).

Electrolytic hydrogenation may take place from acidic, neutral or alkaline solutions. Hydrogenation from an acidic medium is represented by reaction (2.6) which shows that a proton is reduced on the metal surface and gets adsorbed as hydrogen atom. Hydrogenation from alkaline or neutral media is represented by reaction (2.7) so that the reduction of a water molecule on the metal surface results in the formation of an adsorbed hydrogen atom and the hydroxyl ion diffuses into the bulk of the solution. These adsorption processes are named *Volmer reaction*:

$$\mathrm{H^+ + e^- \rightarrow H_{ads}} \qquad \textit{acidic medium} \tag{2.6}$$

$$\mathrm{H_2O + e^- \rightarrow H_{ads} + OH^-} \qquad \textit{neutral or alkaline media} \tag{2.7}$$

Desorption of molecular hydrogen may take place either chemically by the combination of two adsorbed hydrogen atoms (known as *Tafel reaction*; reaction (2.8)), or electrochemically by the reduction of a water molecule to a hydroxyl ion and a hydrogen atom which combines with adsorbed hydrogen atom to form molecular hydrogen, reaction (2.9) and this reaction is known as *Heyrowsky reaction.*
Tafel reaction :

$$\mathrm{H_{ads} + H_{ads} \rightarrow H_2} \tag{2.8}$$

Heyrowsky reaction :

$$\mathrm{H_{ads} + H_2O + e^- \rightleftharpoons H_2 + OH^-} \tag{2.9}$$

In case of hydrogen absorbing-material, the absorption of hydrogen, which can be represented in the same form as reaction [2.5], is a competing process to the desorption process. The predomination reaction is dependent on the overpotential (η) and hence, logarithmically on the current density (*log i*) according to the *Tafel equation*:

$$\eta = a + b \ \log i \tag{2.10}$$

where a and b are constants.

2.2.2 Thermodynamic properties of hydrogen-metal systems

Pressure-composition isotherms have been used to compare the absorption behaviour of hydrogen from the gas phase of amorphous and hydride-forming crystalline materials. The amorphous alloys considered in this case are those having a negative heat of solution of hydrogen, i.e. they accessible to hydrogen absorption. They are classified into three groups: 1) alloys of early and late transition metals (ETM/LTM) e.g. Zr-Ni alloys; 2) alloys of rare earth metals (RE) and LTM (Co, Ni); and 3) metals with metalloid elements (P, Si, etc.) [64].

A schematic p-x-T curve is shown in Fig. 2.8, where p is the hydrogen pressure and x is the concentration of hydrogen in the material. It is obvious that the main difference between the crystalline and the amorphous isotherms is the plateau formed by crystalline alloys, so that at a certain applied hydrogen pressure the solubility of hydrogen in the material increases. This is attributed to phase separation, mostly because of hydride(s) precipitation. On the other hand, in the amorphous state, the hydrogen concentration is found to increase gradually with hydrogen pressure [64, 25]. This phenomenon suggests the formation of a solid solution of hydrogen in the amorphous state. This encourages more study activities to be done to understand the solubility of hydrogen in amorphous structures. In most of the amorphous systems, hysteresis effects have been also observed during absorption/desorption cycles (see the arrows in Fig. 2.8) which is considered quite unusual as the amorphous alloys are suggested to have no phase separation. Yet this may be due to changes in the surface composition caused by hydrogen, which leads to changes in the kinetics of absorption/desorption, or to

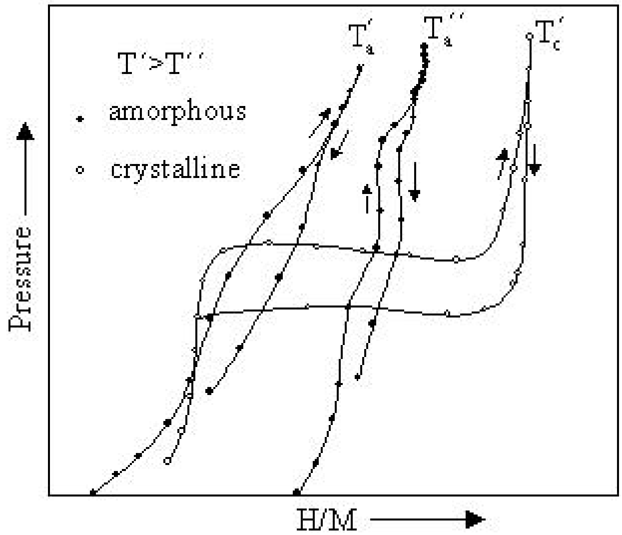

Figure 2.8: Pressure-composition isotherms (p-x-T) curve for hydrogen absorption by a hydride-forming crystalline alloy and its conjugative amorphous alloy e.g. $Zr_{50}Ni_{50}$, (↑) is for absorption curve, and (↓) is for desorption curve).[64]

some structural relaxation. These effects are not fully understood yet. Moreover, the solubility of hydrogen in the amorphous material increases by lowering the temperature as $T' > T''$.

Sievert's law [65] of ideal hydrogen solution is essentially created for crystalline materials. It states that the hydrogen concentration in the material is directly proportional to the square root of the applied hydrogen gas pressure,

$$x \propto \sqrt{P_{H_2}} \tag{2.11}$$

It can also be applied to amorphous alloys for a single homogeneous system at low concentration. Investigations done on the $Ni_{100-x}Zr_x$ binary amorphous system revealed that the range of application of Sievert's law depends on the amorphous composition. So, by increasing x, i.e. by increasing the Zr content, Sievert's law is applied over a wider range of hydrogen-to-metal (H/M) values [25]. Deviation from Sievert's law at higher hydrogen concentrations, which is mostly positive, can be attributed to an energy sites distribution in amorphous alloys which allows hydrogen to enter successively higher energy states.

2.2.3 Energy-site distribution

In crystalline materials, hydrogen atoms in a solid solution practically occupy two types of interstitial sites – octahedral and tetrahedral sites, depending on the structure. For example, fcc, hcp and bcc crystal structures are known to form these site(s). Moreover, hydrogen atoms may occupy vacancies and microstructural defects like dislocations and grain boundaries [66, 67]. In 1987, Harris et al [28] have proposed a model of energy-site distribution in the amorphous binary Ni-Zr system. They have also proposed a suggestion for the hydrogen absorption capacity of amorphous ETM-LTM alloys. This model which was constructed by estimating the hydrogen chemical potential using electrochemical measurements is considered a basic concept for other groups of amorphous alloys as well. They suggested a chemically random alloy composition $A_{1-x}B_x$ (A=LTM and B=ETM) with a structure composed of packed, distorted tetrahedra. The lowest energy hydrogen sites are those surrounded by four-ETM atoms, so that; $E_4 < E_3 < E_2 < E_1 < E_0$, where E_n is the energy of an hydrogen atom in $A_{4-n}B_n$ interstitial sites as seen in Fig. 2.9.

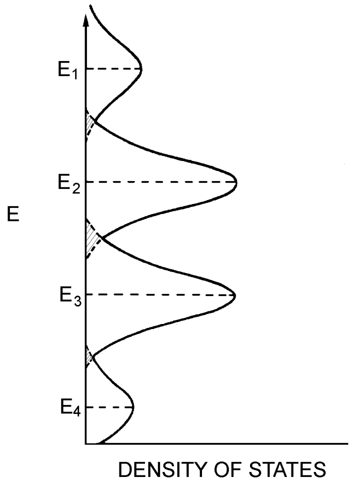

Figure 2.9: Schematic of the density states for hydrogen in tetrahedral interstitial sites [28]

Applying this model on Ni-Zr amorphous alloys, the hydrogen interstitial site energy levels are as follows; Zr_4, Zr_3Ni, Zr_2Ni_2, $ZrNi_3$, Ni_4 [28].
Experimentally, by neutron diffraction and scattering applied to Zr-Ni amorphous alloys, Batalla [27] suggested the occupation of Zr_4 and Zr_3Ni type energy sites [26, 68, 69, 70]. The energy distribution of the hydrogen sites is due to the distortions of the ideal tetrahedral structure in the local glass environment. In this model, the capacity of the different hydrogen energy sites was predicted, however, not all of these sites can be occupied by hydrogen because of the strong repulsive interaction between neighbouring hydrogen atoms at short distances [27, 29, 71, 72].

2.2.4 Diffusion

Diffusion is the natural movement of species, charged or neutral, in matter (solid, liquid and gas) without the effects of an electric field [73]. The rate of diffusion depends on the concentration gradient, this is expressed by *Fick's first law*:

$$J = -D\frac{\partial c}{\partial x} \tag{2.12}$$

where J is the flux of species, $\partial c/\partial x$ the concentration gradient in direction x and D is the proportionality constant known as the *diffusion coefficient.*
Diffusion is a thermally activated process and can be described by an *Arrhenius equation.* For a wide temperature range, D can be expressed in the form :

$$D = D^o exp\frac{-E_a}{k_B T} \tag{2.13}$$

where D^o is a constant and k_B is the Boltzmann constant. Therefore, E_a is calculated from the slope of *1/T* vs *log D* which is called Arrhenius plot. Hydrogen diffuses in metals by jumping between certain energy wells of interstitial sites [64].

In disordered systems, no well defined energy levels exist and, instead, a distribution of energy sites occurs. A model for hydrogen diffusion in disordered systems was proposed by Kirchheim et al. [18, 19, 74, 75] . They proposed that the random packing arrangement of atoms and the distribution of energy sites result in many different atomic configurations of saddle points and a distribution of saddle point energies of hydrogen. However, this situation is drastically simplified by assuming a constant saddle-point energy as shown in Fig. 2.10, which shows the potential trace for an interstitial in amorphous materials with a constant saddle-point energy and a distribution of equilibrium energies. G_k is the energy of site k; G^0 is an arbitrary reference energy and Q^0 is the activation energy for jumping from a reference site. Hydrogen in the high energy site (G^0) needs a small E_a to overcome the energy barrier and hydrogen in the low energy site (G_k) needs a large E_a to overcome the energy barrier.

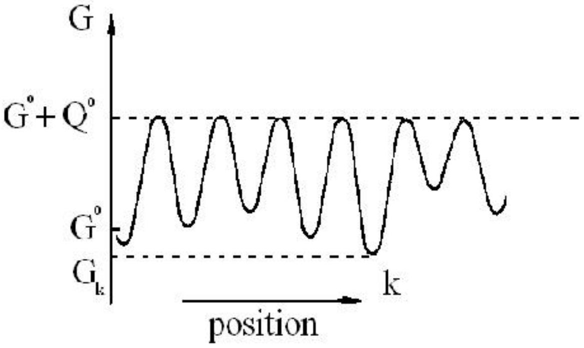

Figure 2.10: Potential trace of hydrogen in disordered systems with a constant saddle point energy[18]

Another advanced model has been proposed by Brouwer et al [76] in 1988, which describes hydrogen diffusion in terms of the chemical and physical structure of the initially and finally occupied sites taking into account interstitial-interstitial interactions in concentrated alloy systems. The results of this model are in good agreement with the experimental results. In fact, the actual mechanism of hydrogen diffusion in amorphous alloys is highly complicated and not accurately statistically estimated yet.

Chapter 3

Experimental

3.1 Sample preparation

Two alloy compositions were chosen for this study, tabulated in table 3.1:

Table 3.1: The atomic percent composition of the alloy samples used.

at.%	Zr	Cu	Al	Ni	(O)
I	55	30	10	5	0.12—0.75
II	65	17.5	7.5	10	0.13—0.82

Pre-alloyed ingots were prepared from the pure elements Zr, Al, Cu and Ni with purities of 99.99%. The components were chemically cleaned by etching in acid solutions, then mixed by arc-melting in a copper mould under a zirconium-gettered argon atmosphere. For reaching high homogeneity the ingot was remelted twice. Different oxygen contents were introduced with the starting elements (mainly with zirconium) and by variation of the oxygen partial pressure of the argon atmosphere upon melting.
The prepared ingots were used as starting materials for melt-spinning. This process was carried out in a single-roller Bühler melt-spinner under argon atmosphere by the help of Dr. Gebert. The pre-alloyed materials were placed in a graphite crucible and the nozzle of the crucible was facing a rotating Cu wheel as shown schematically in Fig. 3.1. The chamber of the melt-spinner was evacuated, then filled with argon, and the material in the crucible was heated inductively up to 1200 – 1300°C, i.e. about 300°C above the melting temperature of the alloys, before the melt was ejected over the rotating wheel, with 1800 rpm, using an argon overpressure for ejection. By this way, ribbons with 3 mm width and 40 μm thickness were obtained. The ribbon side, which was in contact with the wheel, was quite rough while the upper side appeared very smooth and bright. Ribbons prepared under the described quenching conditions were found to be fully amorphous independent of the oxygen content.

Before characterising the as-prepared ribbons or applying any tests, the surface of the as-prepared ribbons was ground by emery papers of 600 and 800 grades to remove the oxide layer and to decrease the surface roughness, then the samples were ultrasonically cleaned in acetone

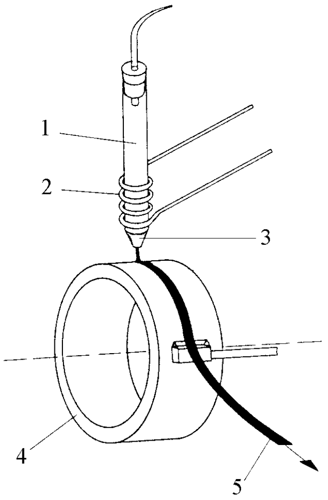

Figure 3.1: A schematic illustration of a single-roller melt-spinning device [77]; (1) argon pressure; (2) induction coil; (3) alloy melt; (4) copper wheel and (5) ribbon.

and dried.

3.2 Oxygen analysis

The determination of the *oxygen concentration* in the as-prepared ribbons was performed using LECO, TC-436 DR analyser, where the samples were melted in. Then, oxygen was detected by an infra-red detector and quantified in mass percentage. This analysis was performed in the analytical department by H. Busskamp.

3.3 Hydrogenation process

The samples were cathodically charged by hydrogen at room temperature in order to prepare samples with different hydrogen concentrations by applying current densities of -1,-5,-10,-20 and -40 mA/cm^2. The cell arrangement is shown in Fig. 3.2. It was filled with 0.1 M NaOH solution of pH=13 with an addition of $5 * 10^{-5}$ mol/l arsenic trioxide as hydrogen promoter. The NaOH solution was prepared from Merck KGaA NaOH pellets of purity $\geq$ 99% and the hydrogen promotor was prepared from Fluka As_2O_3 powder of purity $>$ 99.5%.
A Pt foil was used as a counter electrode and a Potentiostat/Galvanostat PS 5.1 of Sensortechnik Meinsberg GmbH was applied for charging with hydrogen.

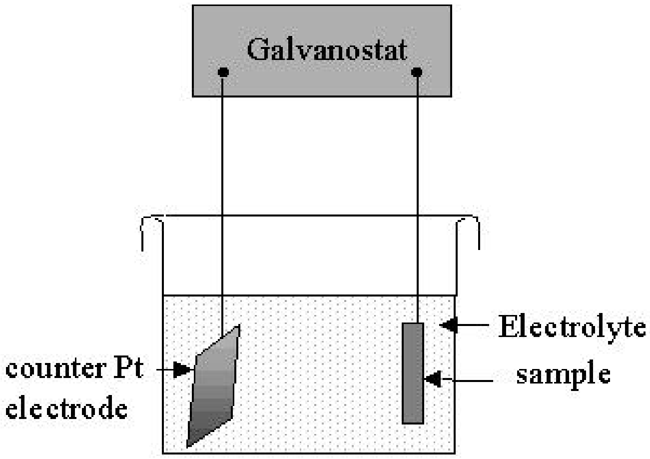

Figure 3.2: Typical schematic electrochemical charging cell.

3.4 Hydrogen analysis

The *hydrogen concentration* in the specimens was measured by the hot extraction method using a LECO, RH-402 analyser. First, the device was purified with nitrogen gas, then hydrogen was extracted by heating up to 1000 K. The change of the thermal conductivity of the gas was measured and from that the hydrogen concentration in the gas mixture was estimated in parts per million (ppm). The atomic hydrogen to metal ratio was calculated by applying the simple relation:

$$\left[\frac{\mathrm{H}}{\mathrm{M}}\right] = \frac{\text{Molecular weight of sample} * [\mathrm{H}]_{\mathrm{ppm}}}{10^6} \tag{3.1}$$

where $[\mathrm{H}]_{\mathrm{ppm}}$ is the hydrogen concentration in parts per million.

3.5 Electrochemical methods

3.5.1 Polarisation test

The polarisation tests were carried out by means of a typical 3-electrode arrangement, using a saturated calomel electrode (SCE) as reference electrode, in a deaerated 0.1 M NaOH + $5 * 10^{-5}$ mol/l As_2O_3 solution and a Pt counter electrode similar to that used for hydrogenation.

The *current density-potential curves* were displayed using a constant potential rate of 2 mV/sec. From the Tafel plot region, the exchange current density (i_o) was estimated at the intersection of the extrapolated anodic and cathodic Tafel slopes, as well as the mixed potential (E') corresponding to i_o.

The *cyclic voltametry measurements* were performed by sweeping the potential in the cathodic region for five forward and backward cycles with a scanning rate of 10 mV/sec.

Some experiments were performed using a rotating disc electrode BM-EDI 101 from Radiometer Copenhagen connected to a CTV 101 speed control unit in order to study the mass transfer effect. Rotating speeds of 1000 and 2000 rpm were used .

3.5.2 Potentiostatic double-pulse technique (PDP)

This method provides qualitative and quantitative information on the reversible and irreversible hydrogen absorption mode. The cell was arranged similar to the polarisation cell using a deaerated 0.1 M NaOH + $5 * 10^{-5}$ mol/l As_2O_3 solution similar to that mentioned in hydrogenation. The principle of the PDP technique is shown schematically in Fig. 3.3 [78]. The sample was charged with hydrogen at a constant cathodic potential E_c for a time t_c. The potential is then stepped in the positive direction to a value, E_{an} (5 to 10 mV negative to the open-circuit potential) to avoid measuring anodic currents for any other contribution, e.g. oxide layer formation. Thus, the anodic current transients (i_d) obtained were due to the oxidation of hydrogen as it diffuses back to the entry surface. The transients were integrated to determine the anodic charge (q_a) corresponding to each charging potential. The open-circuit potential of the sample was measured immediately before each pulse.

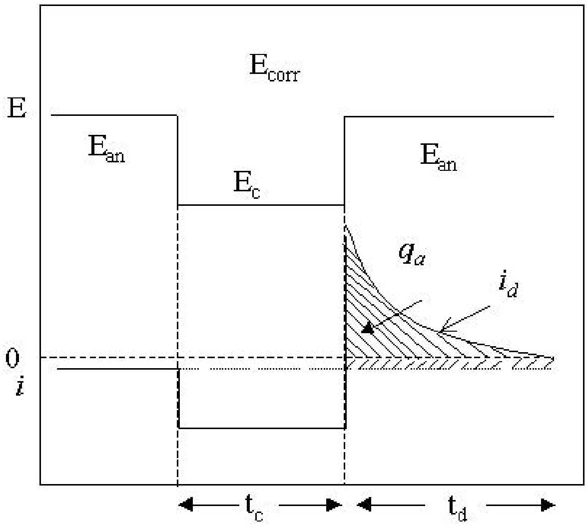

Figure 3.3: Schematic potential steps and current response during the PDP experiment [79]
.

A mathematical model was used in the data analysis, to determine the hydrogen diffusion and the hydrogen concentration, from the analysis of Fick's second law [80, 79] given as:

$$i_d = FD_*^{1/2}C_0\pi^{-1/2}[t_d^{-1/2} - (t_d + t_c)^{-1/2}] \tag{3.2}$$

F is Faradays constant, D_* is the diffusion coefficient, C_0 is the concentration of hydrogen atoms at the sample surface left after the anodic transient, and t_d is the anodic transient time. Hence the product $D_*^{1/2}C_0$ can be estimated from the slope of i_d vs the time term, and if either the solubility or the diffusivity is known, the other parameter can be evaluated.
The E_c was selected at -1, -1.2 and -1.5 V, t_c for 1– 4 minutes so that only small hydrogen concentrations were allowed to enter the samples. Anodic transients were measured for 5 minutes.

3.5.3 Permeation technique

The electrochemical permeation method has been widely used in the studies of hydrogen diffusion. It is based on the Devanathan and Stachurski [81] arrangement. A membrane (specimen) separates two electrolytes with separate counter and separate reference electrodes as shown in Fig. 3.4. At one side the specimen is charged by hydrogen (entrance side), then hydrogen diffuses through the specimen and is detected on the other side (detection side). The detection side of the specimen had been cathodically plated with a thin film of palladium to avoid any potential contribution from metal oxidation [78]. Deaerated 0.1 M NaOH + $5 * 10^{-5}$ mol/l

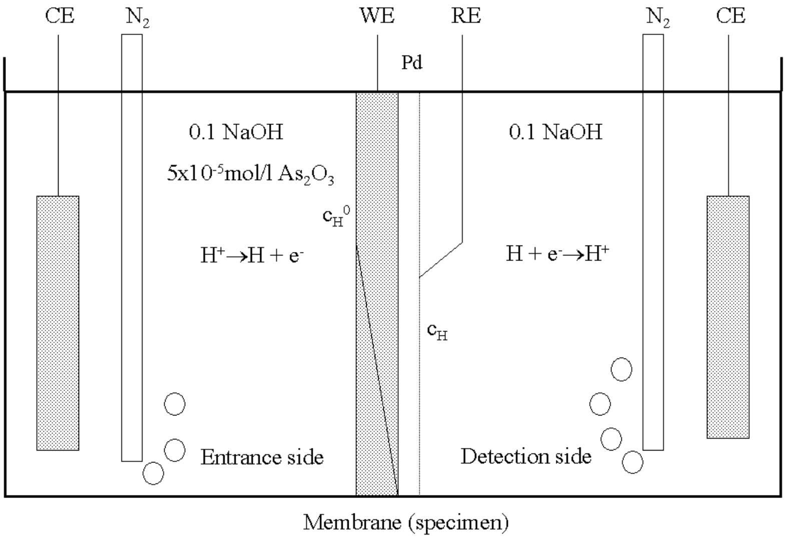

Figure 3.4: A permeation cell to study the diffusion of hydrogen through a specimen membrane [78].

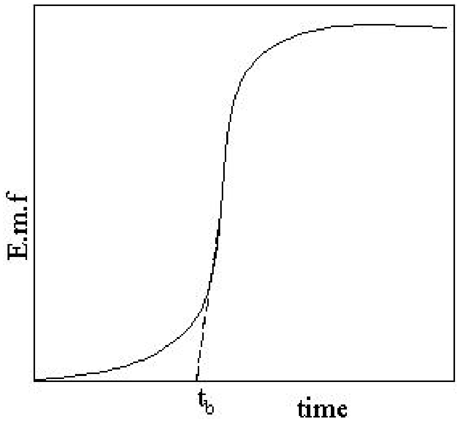

Figure 3.5: Variation in anodic potential with time for a sample membrane [78].

As_2O_3 solution similar to the charging solution was used. Cathodical galvanostatic pulses of

-1mA/cm^2 for 2 and 5 seconds were used to charge the specimens with hydrogen and on the detection side (the dull side of the ribbon) the potential change was followed.
The time needed for hydrogen to arrive at the detection side, named *break-through time* (t_b) (see Fig. 3.5) was used to estimate the diffusion coefficient by applying the relation:

$$t_b = 0.5\frac{L^2}{\pi^2 D_*} \tag{3.3}$$

where L is the thickness of the specimen.

3.6 Thermal analysis

3.6.1 Thermal desorption analysis (TDA)

Thermal desorption analysis (TDA) has been utilised to get information about hydrogen site occupation, hydride formation and transformation. The samples were annealed under an ultra-high vacuum atmosphere, i.e. the pressure was 10^{-8} mbar, with a constant heating rate of 20 K/min starting from 300 K till 1023 K. During heating, hydrogen, oxygen and water were detected simultaneously by means of a quadrupole mass spectrometer.

3.6.2 Differential scanning calorimetry (DSC)

A Perkin Elmer differential scanning calorimeter (DSC 7) has been utilised to study the thermal properties of the as-prepared and of the hydrogen charged amorphous specimens. DSC gives information about the glass transition (T_g), the undercooled liquid region, the crystallisation temperature (T_x) and the melting temperature (T_m).
The DSC principle is based on *power compensation* between a sample and a reference during heating with a constant heating rate, so that the energy absorbed or evolved by the sample is balanced to keep the temperature difference (ΔT) between the reference and the sample equal to zero. This is named "null balance" principle [43].
The power (energy per unit time) needed to keep the sample holder temperature identical to that of the reference holder is made directly in differential power units [milliwatts (mW)] as shown in Fig. 3.6. Accordingly, T_g displays an endothermic event, over a range of temperature, also T_m displays an endothermic event, while T_x exhibits an exothermic event. It is possible to estimate the heat release, i.e. the enthalpy (ΔH), by integrating the power so that an endothermic process, e.g. T_m and T_g, yield negative ΔH. To measure the change in energy and temperature Pt-resistance heaters and thermometers are used in DSC 7.
Fig. 3.6 examplifies the definition of the glass transition by the intersection of the tangents of the baseline and of the endothermic curve. Hence, the so-defined onset temperature of the glass transition (T_g^{on}) is given at the intersection of the two tangents. The onset of the crystallisation temperature T_x was defined by the intersection of the extrapolated base line and the exothermic signal tangent of the crystallisation peak. The measurements were done under argon atmosphere of 99.99% purity. All measurements were done using a constant rate temperature-scan with a heating rate of 20 K/min starting from 310 K.

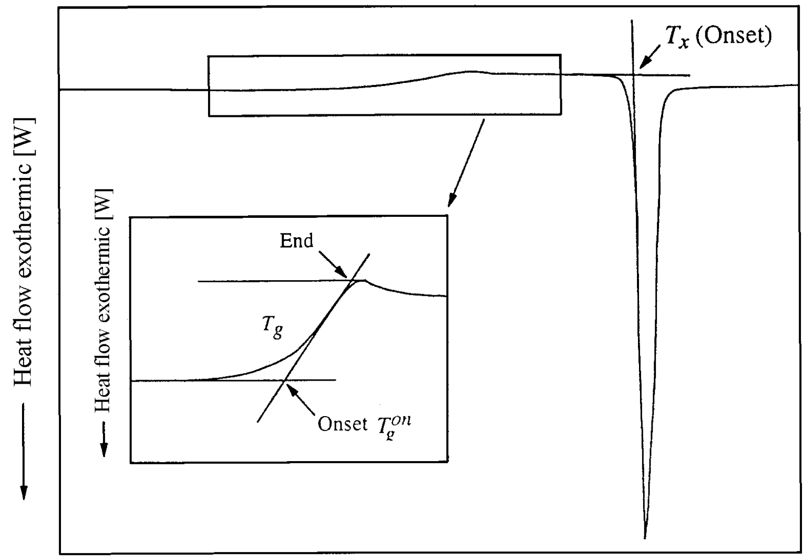

Figure 3.6: Schematic DSC trace showing the T_g onset and the T_x onset as typical for metallic glasses.

3.7 Characterisation methods

3.7.1 X-ray diffraction (XRD)

The phase analysis of the melt-spun ribbons and of the samples after hydrogen charging and annealing was performed by X-ray diffraction (XRD) using a Phillips PW 1050 diffractometer with Co K_α radiation of wave length $K_{\alpha 1} = 1.78897$ Å operating in Bragg-Brentano-geometry. The XRD method is based on the principle that X-rays can be diffracted by the regularly spaced atoms of a crystal, acting as scattering centres when the X-ray wave length is equal to the interatomic distance in the crystal [82]. The given diffraction pattern of scattered intensity versus 2θ (the scattering angle) for a crystalline solid shows sharp peaks occurring at certain angles corresponding to crystalline phase(s). The width of the peak is a measure of the particle size, so that the width increases when the particle size decreases. For an amorphous phase, the lack of periodicity of the atomic structure, i.e. a long-range order structure, results in the appearance of one or two broad maxima in the diffraction pattern with low intensity, as a weak scattering occurs in all directions. Therefore, high resolution measurements, which require long measuring time, are necessary to characterise the amorphous phase accurately. The angle step size chosen for all measurements was 0.05°. The time of measuring was 20 seconds per step for amorphous phase characterisation and 8 seconds per step for the crystalline phases analysis.

3.7.2 Auger electron spectroscopy (AES)

The surface composition of the uncharged and the hydrogen charged ribbons was investigated by Auger electron spectroscopy (AES) sputter profiling. The analysis was performed with a PHI

660 Auger microprobe applying 10 keV as primary energy, 100 nA electron current and a 30° angle of incidence of the electrons. Depth profiling was done by sputtering using argon ions at 60° to the sample normal with an energy of E=1.5 keV. These investigations were done by Dr. S. Baunack.

3.7.3 Electron microscopical investigations

(i) Scanning electron microscopy (SEM)

Scanning electron microscopy (SEM) investigations were utilised to image the surface topography of the uncharged and the hydrogen charged ribbon samples. For these purposes, a JEOL JSM-6400 type SEM operating at 25 kV was used. The images were obtained using the secondary electron mode. These investigations were done by Dr. A. Güth.

(ii) Transmission electron microscopy (TEM)

The bulk microstructure of the samples was characterised in high resolution up to nanometer scale using transmission electron microscopy (TEM). The investigations were carried out with a JEOL 2000 FX at an acceleration voltage of 200 kV. TEM samples were prepared from the ribbons by ion beam thinning using a Gatan PIPS system. The images were taken in the bright-field mode.

Selected area diffraction (SAD) and energy dispersive X-ray (EDX) analysis were performed for phase analysis. Average concentrations were taken out of ten EDX measurements. These investigations were done by Dr. J. Thomas and K. Mickel.

Chapter 4

Hydrogenation effect on Zr-based alloys

4.1 Room temperature hydrogenation

The melt-spun amorphous $Zr_{55}Cu_{30}Al_{10}Ni_5$ and $Zr_{65}Cu_{17.5}Al_{7.5}Ni_{10}$ ribbons contain trace amounts of hydrogen the H/M=(0.0025 – 0.015) without applying any absorption method indicating a rather high hydrogen absorption ability of these alloys.
Upon electrochemical charging of the ribbons at room temperature at current densities of -5, -10, -20 and -40 mA/cm^2 their properties change in a way that up to about H/M=0.12, the ribbons seem to lose their high ductility. Further hydrogen absorption, up to about H/M=0.75, the ribbons become spiral-shaped-deformed and more brittle due to the internal stresses caused by the hydrogen absorption. Charging to H/M > 0.9, the silvery bright original colour becomes darker and dull, and the ribbon edges undergo cracking as shown in Fig. 4.1. The $Zr_{55}Cu_{30}Al_{10}Ni_5$ ribbons undergo self-degradation when the hydrogen concentration exceeds H/M=1.5, while for $Zr_{65}Cu_{17.5}Al_{7.5}Ni_{10}$ ribbons, this was observed when the hydrogen concentration exceeds H/M=1.65.

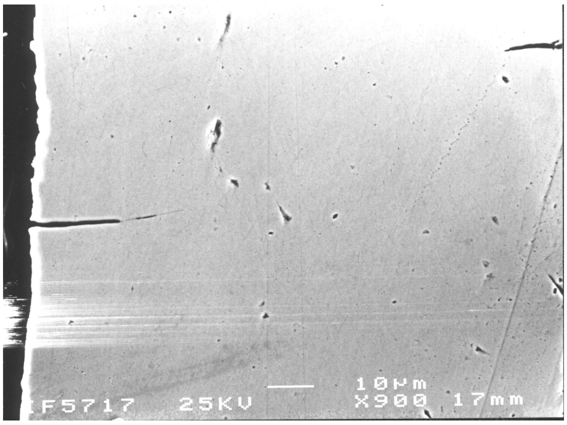

Figure 4.1: SEM image of a $Zr_{55}Cu_{30}Al_{10}Ni_5$ ribbon sample charged to H/M= 0.8.

Although the amorphous $Zr_{65}Cu_{17.5}Al_{7.5}Ni_{10}$ alloy ribbon absorbs more hydrogen than $Zr_{55}Cu_{30}Al_{10}Ni_{5}$, i.e. up to a maximum H/M=1.65 as compared to 1.5 for $Zr_{55}Cu_{30}Al_{10}Ni_{5}$ alloy composition, its rate of hydrogen absorption is lower than that of the $Zr_{55}Cu_{30}Al_{10}Ni_{5}$ alloy especially within the first 24 hours as shown clearly in Fig. 4.2. This may be due to a slower surface activation process of the $Zr_{65}Cu_{17.5}Al_{7.5}Ni_{10}$ alloy for hydrogen absorption.

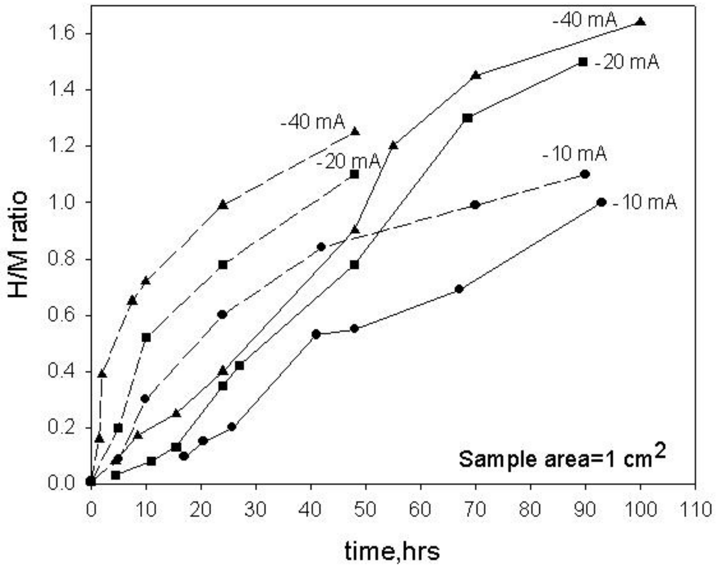

Figure 4.2: Hydrogen absorption rate of the amorphous $Zr_{55}Cu_{30}Al_{10}Ni_{5}$ alloy (dashed-curves) and the amorphous $Zr_{65}Cu_{17.5}Al_{7.5}Ni_{10}$ alloy (solid-curves).

The XRD patterns of amorphous $Zr_{65}Cu_{17.5}Al_{7.5}Ni_{10}$ samples, illustrated in Fig. 4.3, for an as-quenched ribbon and for a ribbon charged up to H/M= 1.3 using a fast charging rate corresponding to a current density of -20mA/cm^2 for 60 hours show that the amorphous structure is preserved upon charging. However, the characteristic broad maxima of the amorphous state shift to lower scattering angle values in comparison to the uncharged alloy, indicating an expansion in the amorphous structure by hydrogen absorption. This becomes even more pronounced with increasing hydrogen concentration. On the other hand, the pattern of a $Zr_{65}Cu_{17.5}Al_{7.5}Ni_{10}$ ribbon hydrogen charged to the same H/M ratio at -1mA/cm^2 (much slower rate) for 600 hours, reveals the main peaks of Zr-hydride and Cu and/or Cu-rich phase(s) such as cubic Cu_4Al and Cu_9Al_4.
This result is confirmed by EDX analysis upon TEM investigations of a charged sample which shows an enrichment of Cu and / or Cu-rich phases in the amorphous matrix. Additionally an Al-rich area is detected.

Surface composition of both the $Zr_{55}Cu_{30}Al_{10}Ni_{5}$ and the $Zr_{65}Cu_{17.5}Al_{7.5}Ni_{10}$ alloys charged up to H/M=0.95, using even a charging current density rate of -20 mA/cm^2 was investigated by AES measurements. The surface of the charged samples was found to alter significantly from the as-prepared ones in a way that, the oxide layer is highly reduced, a depletion of the Zr concentration (possibly due to Zr-hydride formation) and enrichment of Cu and Al are always detected on the surface of the charged samples, while the Ni concentration is not affected by

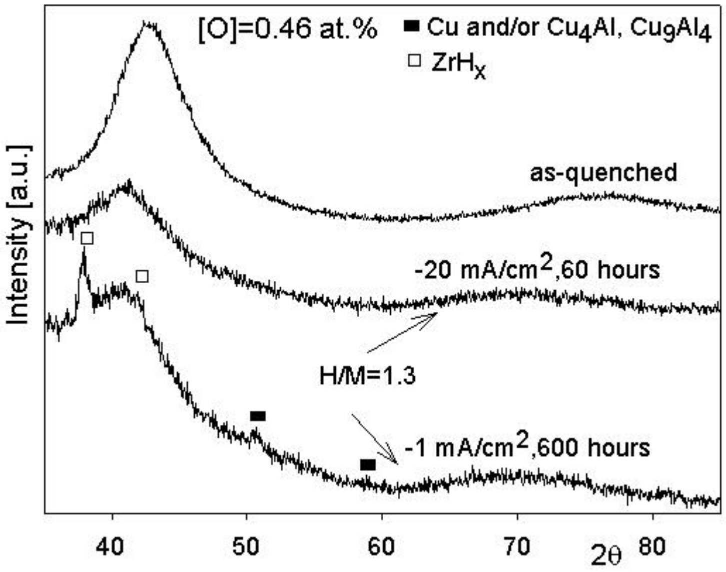

Figure 4.3: XRD patterns of as-prepared $Zr_{65}Cu_{17.5}Al_{7.5}Ni_{10}$, hydrogenated $Zr_{65}Cu_{17.5}Al_{7.5}Ni_{10}$ up to H/M=1.3 using $i = -20\,\mathrm{mA/cm^2}$ and $i = -1\,\mathrm{mA/cm^2}$.

hydrogen.

One can conclude from these results that at room temperature and at a very high hydrogen content, a rearrangement of the amorphous matrix takes place in a way that hydrogen induces a Cu-clustering and an Al enrichment on the alloy surface. Also a Zr-hydride formation is possible. This change in the amorphous matrix may assume that hydrogen tends to increase the number of sites of high affinity to it, i.e. number of Zr sites.

4.2 Thermal behaviour of hydrogenated $Zr_{55}Cu_{30}Al_{10}Ni_{5}$

4.2.1 Hydrogen desorption

The thermal hydrogen desorption behaviour of $Zr_{55}Cu_{30}Al_{10}Ni_{5}$ samples with different H/M values was investigated by TDA measurements and the results are displayed in Fig. 4.4. All samples show a distinct stepwise desorption behaviour, suggesting that different desorption processes occur in different temperature regimes.

The desorption can be divided into two different stages, one stage below 623 K and the second stage starts at about 673 K. The first stage is before Zr-hydride formation by thermal activation in the amorphous structure, while the second stage is characterised by the effusion of hydrogen due to decomposition of the different hydride phases, giving rise to sharp desorption peaks. These features will be discussed in detail in the following for selected samples charged to different H/M ratios, also in conjunction with the XRD data obtained for the samples upon heating to different characteristic temperatures (discussed in section 4.3).

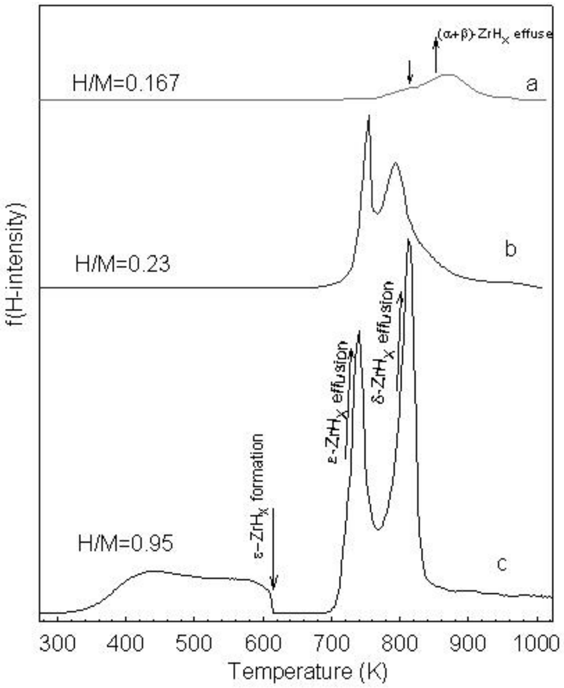

Figure 4.4: Hydrogen desorption analysis of hydrogenated $Zr_{55}Cu_{30}Al_{10}Ni_5$ metallic glass with different hydrogen contents using a heating rate of 20 K/min.

Ribbons with low H/M ratios of 0.167 and 0.23 (Fig. 4.4) do not show hydrogen effusion in the first temperature range *below 623 K*, indicating that the hydrogen is captured in interstitial sites with tetrahedral symmetry corresponding to low energy levels with high hydrogen affinity [28].

In contrast, the sample with the highest hydrogen content, H/M=0.95, shows a broad desorption maximum between 323 K and 618 K, which points to hydrogen desorption from interstitial sites with lower affinity to hydrogen [28]. At *618 K* a sharp drop of the curve occurs, reaching nearly the level of the baseline. At this temperature, the remaining hydrogen has reacted to crystalline Zr-hydride phases by thermal activation, as proved by structural analysis in the next section.

The second range at temperatures *above 673 K* is characterising the effusion of hydrogen due to a partial decomposition of the different crystalline Zr-hydride phases, so that each peak is followed by a transformation into another Zr-hydride phase with lower hydrogen content at higher temperatures. The different steps are systematically explained as follows:

The strongest TDA signals in this temperature regime are observed for the $Zr_{55}Cu_{30}Al_{10}Ni_5$ ribbon with H/M=0.95. At about *713 K* hydrogen effusion occurs due to partial decomposition of the tetragonal ε-Zr hydride phase which was formed at 618 K.
At about *743 K*, i.e. at the maximum of the first sharp desorption peak, effusion stops and a

distinct drop of the signal is visible which corresponds to the transformation of the tetragonal ε-Zr hydride to an fcc δ-Zr hydride phase.
At *773 K* further hydrogen effusion occurs by partial decomposition of the δ-Zr hydride phase, and at about *813 K*, i.e. at the maximum of the second sharp desorption peak, the effusion almost stops.

The subsequent drop of the hydrogen intensity signal indicates the transformation of other Zr hydride phases. Comparing with the hydrogen-zirconium phase diagram (Fig. 4.5) [83] these phases could be identified as a mixture of $(\alpha + \beta)$-Zr hydrides.

The final decomposition of the $(\alpha + \beta)$-Zr hydride mixture is more clearly visible for the sample with lower initial hydrogen content of H/M=0.167. In comparison with the hydrogen-zirconium phase diagram at low hydrogen contents the formation of the α hydrides or $(\alpha + \beta)$ hydrides is favoured in the temperature range higher than 573 K. As shown in Fig. 4.5, this mixture shows eutectoid decomposition at 823 K.

Comparing with the data obtained in Fig. 4.4 curve a, hydrogen effusion takes place at about *823 K* due to the decomposition of the $(\alpha + \beta)$-Zr hydride phase mixture.

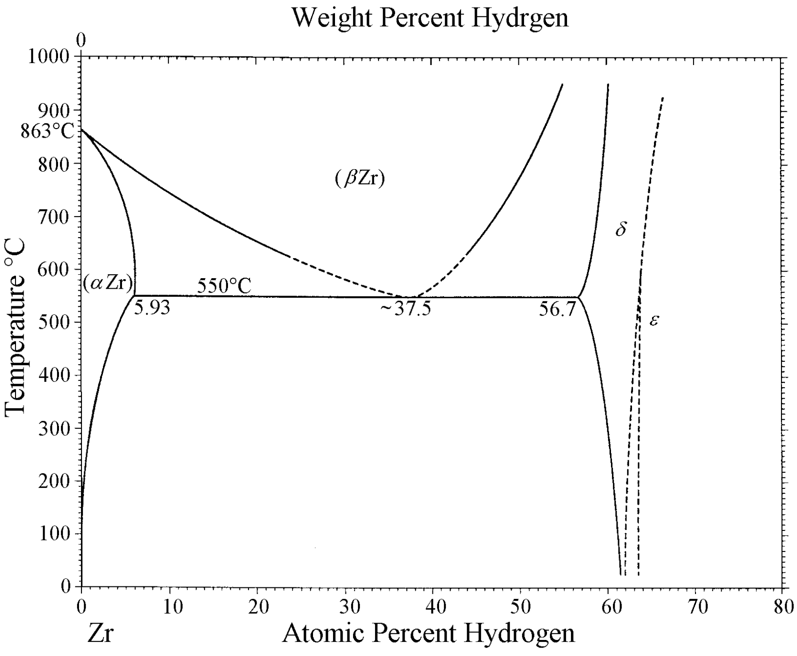

Figure 4.5: Hydrogen– Zirconium phase diagram. [83]

Comparing the TDA curves of the $Zr_{55}Cu_{30}Al_{10}Ni_5$ samples with different H/M ratios reveals that the decomposition of the ε-Zr hydride phase shifts to lower temperatures with increasing H/M ratio. This observation is also in agreement with the H-Zr phase diagram, and will be discussed in more details in the structural analysis (see section 4.3).

4.2.2 Thermal stability

The change in the thermal stability of the $Zr_{55}Cu_{30}Al_{10}Ni_5$ metallic glass alloy by the absorption of different amounts of hydrogen is shown in Fig. 4.6.

Curve (a) represents the thermal behaviour of the **uncharged** alloy. The DSC scan exhibits an endothermic heat effect due to the glass transition followed by a sharp exothermic peak corresponding to the simultaneous crystallisation of the material into intermetallic phases, discussed by structural analysis later. The glass transition temperature T_g is 707 K and the onset of crystallisation occurs at T_x=771 K, leading to a rather wide undercooled liquid region ΔT_x of 64 K for the heating rate of 20 K/min.

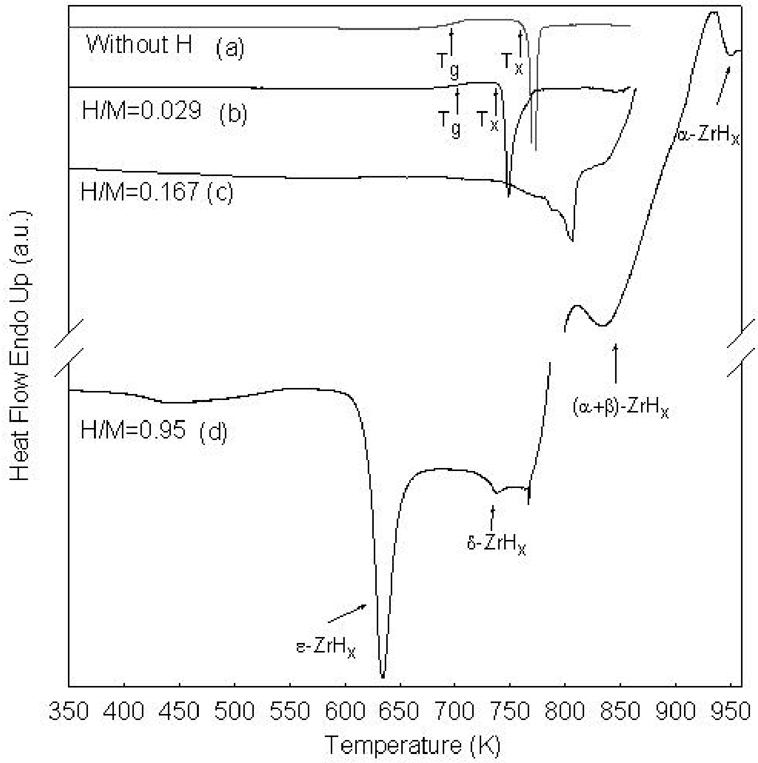

Figure 4.6: DSC measurements of hydrogen-charged $Zr_{55}Cu_{30}Al_{10}Ni_5$ metallic glass with different hydrogen contents using a heating rate of 20 K/min.

Absorption of an even small amount of hydrogen changes the thermal stability of the metallic glass significantly. This effect is obvious in curve (b) for a H/M value of **0.029**, the exothermic crystallisation peak broadens, T_x drops to 748 K and ΔT_x decreases to 44 K. This reduction of the undercooled liquid region may be due to the formation of very fine zirconium hydride crystals in the amorphous matrix in the temperature range from 573 K to 673 K (corresponding to the Zr-hydride formation temperature [83]), which may act as nucleation sites for the crystallisation of the alloy, explaining the decrease in the thermal stability compared to the uncharged metallic glass.

For the sample with **H/M=0.167** (curve c), no indication for a distinct glass transition or a significant undercooled liquid region was found. The crystallisation of the alloy occurs in several steps as confirmed by structural analysis (see next section). This may be due to an increased number of Zr-hydride crystals, which act as heterogeneous nucleation sites for further crystallisation. Moreover, precipitation of Zr-hydrides changes the composition of the residual amorphous phase towards an overall composition depleted in Zr. Presumably, both effects change the crystallisation behaviour from simultaneous formation of intermetallic phases in the case of the uncharged alloy to a stepwise phase transformation mode in the presence of Zr-hydrides.

At about 838 K, an endothermic reaction starts which is related to the decomposition of $(\alpha+\beta)$-Zr hydride and the effusion of hydrogen. No endothermic reaction occurs in the range from 713 K to 813 K for two reasons: the fraction of ε- and δ-Zr hydride phases formed is less than that of the $(\alpha+\beta)$-Zr hydride phases as it is clear from their decomposition by TDA (Fig. 4.4 curve a). Also at the same time, the crystallisation of the amorphous matrix takes place in this temperature region. The summation of these two effects is exothermic, as in this case the exothermic heat release is predominant.

For hydrogen contents as high as **H/M=0.95** (Fig. 4.6 curve d), only the formation and transformation of the different Zr-hydrides are detected as exothermic peaks in the DSC scans. The strong exothermic event starting at 613 K is due to the formation of ε-Zr hydride, most likely with different stoichiometries, which is also shown by TDA in Fig. 4.4 curve (c).

At 733 K another exothermic peak is visible which is related to the partial transformation of ε-Zr hydride to the δ- Zr hydride phase, followed by an exothermic peak at 818 K indicating the partial transformation to $(\alpha+\beta)$-Zr hydride phases. Finally at 938 K the transformation to the α-Zr hydride phase shows up as an exothermic event. Besides the exothermic transformations, a strong endothermic flow signal is present for temperatures above 773 K, being due to the decomposition of the δ-Zr hydride phase (1^{st} endothermic reaction) and the β-hydride phase (2^{nd} endothermic reaction).

There are no signs of exothermic reactions upon crystallisation of the amorphous matrix, although all the amorphous phase, in fact, crystallised around 873 K, as in this case the summation of the exothermic stepwise crystallisation and the endothermic reaction for decomposition of a large amount of Zr-hydride phases is endothermic.

It is noticed that the slope of the second endothermic reaction curve after the $(\alpha+\beta)$-Zr hydride transformation (from 850 K to 930 K) is smaller than the slope of the endothermic reaction curve after the peak resembling the δ-Zr hydride transformation (from 770 K till 800 K). This is due to the intensive crystallisation of the amorphous matrix around 873 K (discussed in structural analysis) as a result of the decomposition of the hydride. Hence, more Zr atoms are set free and more crystallisation of the amorphous matrix takes place.

Only at the transformation temperatures the decomposition of the hydride phases stops, so exothermic peaks occur due to transformation and perhaps accompanied by formation of a small amount of crystalline phase(s). At 513 K an endothermic reaction takes place before the formation of Zr-hydride due to effusion of hydrogen from the interstitial sites of high energy levels, as it is also clear from the TDA (Fig. 4.4 curve c).

From the DSC measurements at different heating rates from 2 to 120 K/min the activation energy of crystallisation of both uncharged $Zr_{55}Cu_{30}Al_{10}Ni_5$ ribbon and charged one to a ratio of H/M=0.9 were calculated using the Kissinger method [84]:

$$\ln\left(\frac{R}{T_x^2}\right) = -\frac{E_A}{k_B T_x} + C \tag{4.1}$$

Where R is the heating rate, E_A the effective activation energy of the crystallisation (transformation) reaction, T_x the temperature of the peak maximum, k_B Boltzmann constant.
The mean activation energy E_A of the uncharged alloy for the crystallisation of different intermetallic phases (Fig. 4.6 curve a) and of the charged material for the formation of ε-Zr hydride (Fig. 4.6, curve d) are 4.4 eV and 2.6 eV respectively. The lower value of the activation energy for the formation of hydrides agrees with the results of the DSC measurements.

4.3 Structural analysis of the $Zr_{55}Cu_{30}Al_{10}Ni_5$ alloy

Fig. 4.7 shows the X-ray diffraction patterns for $Zr_{55}Cu_{30}Al_{10}Ni_5$ ribbons uncharged and charged with a hydrogen content of H/M=0.95 after heating to 778 K, slightly higher than T_x of the uncharged alloy.

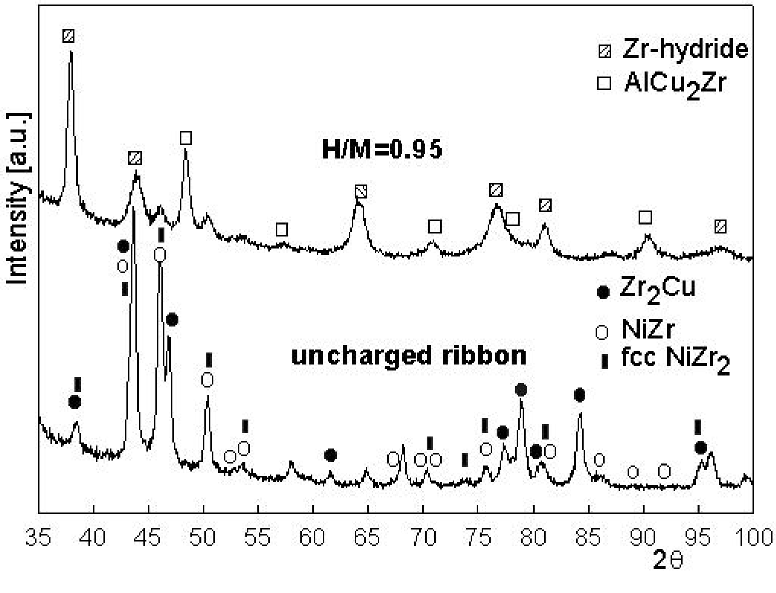

Figure 4.7: XRD analysis of $Zr_{55}Cu_{30}Al_{10}Ni_5$ metallic glass uncharged and hydrogen-charged to H/M=0.95, then heated to 778 K.

The pattern of the hydrogenated sample indicates a different mode of crystallisation than the uncharged metallic glass. The hydrogen-free amorphous ribbon crystallises by the formation of a mixture of intermetallic phases: metastable fcc-$NiZr_2$, tetragonal $CuZr_2$ and orthorhombic NiZr are found after annealing. In contrast, the phases formed upon crystallisation of the hydrogenated ribbon with H/M=0.9 are cubic δ-Zr hydride phases of different stoichiometries together with cubic $AlCu_2Zr$. This reveals that the presence of hydrogen completely changes the crystallisation behaviour of the $Zr_{55}Cu_{30}Al_{10}Ni_5$ matrix alloy by the formation of the zirconium hydride phase(s). The precipitation of Zr-hydrides leads to a depletion of Zr in the residual metallic glass, consequently causing a local enrichment of the amorphous phase by the other elements, especially copper.

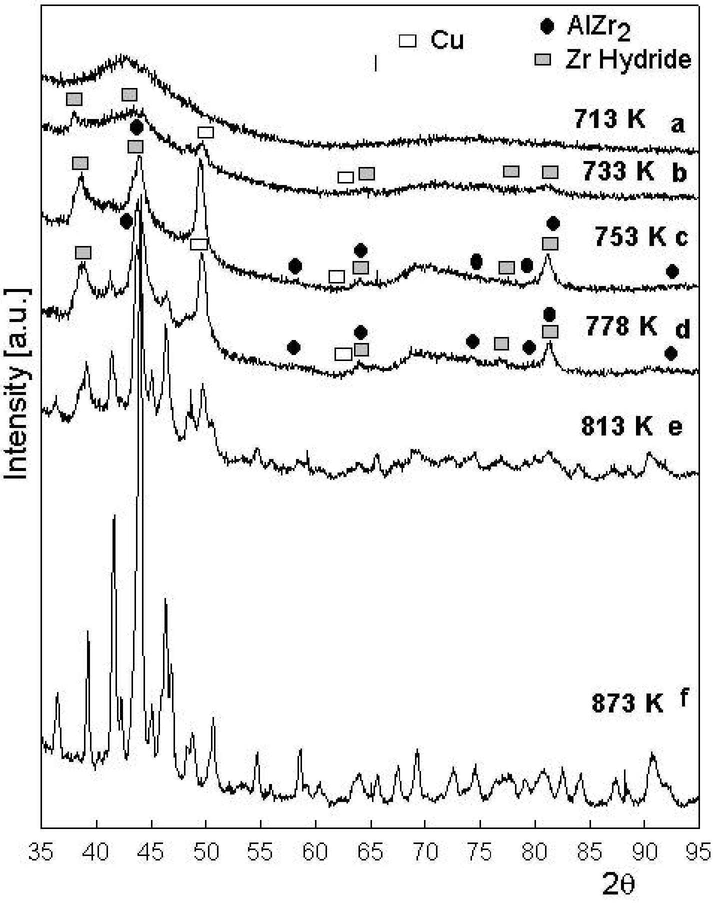

Figure 4.8: XRD analysis of hydrogen-charged $Zr_{55}Cu_{30}Al_{10}Ni_5$ metallic glass to H/M=0.37 then heated to different temperatures using a heating rate of 20 K/min.

To further study in more detail the crystallisation behaviour of the $Zr_{55}Cu_{30}Al_{10}Ni_5$ alloy after hydrogen charging, samples with different H/M ratios were heated to different selected temperatures.

Fig. 4.8 presents the XRD patterns of a charged ribbon with H/M=0.37 after heating to different temperatures. Up to *713 K (pattern a)*, the alloy shows only the broad diffraction maxima characteristic for the amorphous phase. Besides, a small amount of Zr-hydride might be present after annealing, as suggested by the TDA results (Fig. 4.4). However, the crystallites are very small and cannot be detected due to the limited resolution of XRD.
After heating to *733 K*, the diffraction pattern reveals the formation of a small volume fraction of cubic Zr-hydrides and the main peak of Cu and/or Cu-rich phase(s) (as discussed before in

Fig. 4.3 using i=-1mA/cm^2).
The diffraction patterns for samples heated to temperatures between *753 K and 778 K* show the formation of hexagonal $AlZr_2$ phase and cubic Zr-hydride phases coexisting with the Cu rich phase(s) and some residual amorphous phase as indicated by the broad diffuse intensity contribution still present after heating to this temperature.
After heating to *813 K (pattern e)*, massive crystallisation of the material with a residual hydrogen content of H/M=0.22 is observed, but the phases formed are different from those found for the uncharged ribbon as it was analysed in Fig. 4.7.
At *873 K (pattern f)*, corresponding to a residual H/M=0.12, further phases are observed which are similar to those found for the uncharged ribbon, but which could not be identified unambiguously.

The crystallisation behaviour of the $Zr_{55}Cu_{30}Al_{10}Ni_5$ ribbon hydrogenated up to H/M=0.37 using 20 K/min as heating rate can be summarised as follows:

amorphous phase → 733 K → ZrH_x + Cu clusters and/or Cu-rich phase → (753– 778 K) → hexagonal $AlZr_2$ + Cu clusters + ZrH_x → 813 K → unknown crystalline phases → 873 K → phases similar to crystalline uncharged ribbon.

Figure 4.9 shows the diffraction pattern after annealing for charged ribbons with high hydrogen contents in the range of $0.7 < H/M < 1$. Heating to *643 K* induces precipitation of tetragonal ε-Zr-hydride (pattern a). The rather broad crystalline diffraction peaks suggest the formation of very fine crystallites from the amorphous matrix.
At *713 K* (pattern b) the formation of cubic $AlCu_2Zr$ starts. This phase becomes more pronounced after annealing at 753 K (pattern d).
In addition, the diffraction pattern taken after heating to *733 K* reveals the start of the transformation of δ-Zr hydride as shown by the TDA scan (Fig.4.4, curve c) and the DSC scan (Fig. 4.6, curve d). Notice that the two peaks at 2θ=62 and 64.5^o seem to unify. At *753 K* (pattern d) the cubic δ-Zr hydride phase is clearly visible.
At *838 K*, the temperature of the third exothermic peak in the DSC scan (Fig. 4.6, curve d), the intensities of the hydride peaks decrease due to decomposition of the δ-Zr hydrides and hydrogen effusion accompanied by the formation of other crystalline phases caused by an increased number of Zr atoms provided by the decomposition of the δ-Zr hydrides. It is possible to assume from Fig. 4.6 (curve d) that the residual hydride peaks shown in Fig. 4.9 (curve f) at 838 K are due to partial decomposition of δ-Zr hydrides and transformation to $(\alpha + \beta)$-Zr hydrides.
After heating to *873 K* (pattern g), where the residual hydrogen content is H/M=0.18 most of the hydrides have decomposed and the sample consists of a mixture of crystalline phases which could not be identified unambiguously.

The crystallisation behaviour of the $Zr_{55}Cu_{30}Al_{10}Ni_5$ ribbon hydrogenated up to $0.7 < H/M < 1$ using 20 K/min as heating rate can be summarised as follows:

$(643\text{ K}) \rightarrow \varepsilon - ZrH_x \rightarrow (713\text{K}) \rightarrow \varepsilon - ZrH_x + AlCu_2Zr \rightarrow (733\text{K}) \rightarrow (\varepsilon \rightarrow \delta) - ZrH_x + AlCu_2Zr \rightarrow (753 - 778\text{K}) \rightarrow \delta - ZrH_x + AlCu_2Zr \rightarrow (\delta \rightarrow (\alpha + \beta)) - ZrH_x + AlCu_2Zr$.

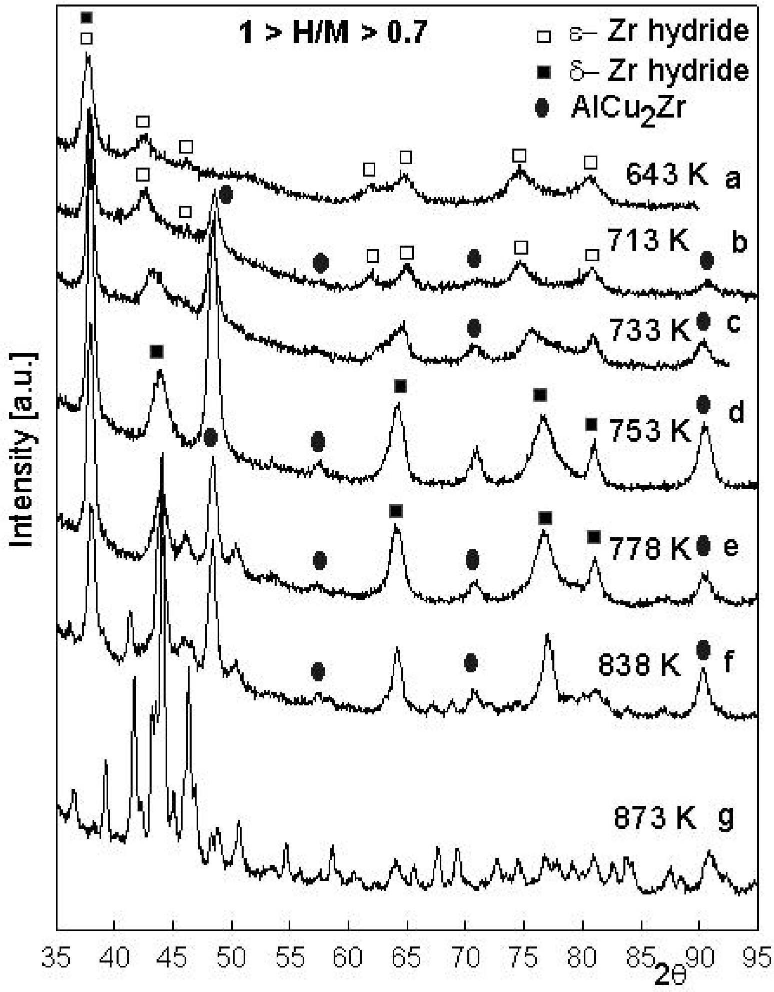

Figure 4.9: XRD analysis of the $Zr_{55}Cu_{30}Al_{10}Ni_5$ metallic glass hydrogen-charged to $0.7 < H/M < 1$ then heated to different temperatures using a heating rate of 20 K/min.

It is clear from Fig. 4.8 (pattern b) and Fig. 4.9 (pattern c) that, as the hydrogen content increases, crystallisation takes place at lower temperatures. Presumably, this is due to lower mean activation energies of the phases formed at higher H/M ratios compared to the mean activation energies of the phases formed at lower H/M ratios.

There is no sign of nickel hydride or zirconium nickel hydride compounds probably because of the low atomic percentage of nickel in the alloy or due to the low stability of nickel hydrides which decompose readily.

4.4 Influence of hydrogen in the presence of oxygen

A detailed studies of the effect of trace amounts of oxygen on the thermal stability, the crystallisation mode and the microstructure of bulk Zr-Cu-Al-Ni metallic glasses were presented by

Gebert et al [15, 17] as discussed in section 2.1.4. Since oxygen was found to have a pronounced effect on the $Zr_{65}Cu_{17.5}Al_{7.5}Ni_{10}$ alloy and no significant effect on the $Zr_{55}Cu_{30}Al_{10}Ni_5$ alloy, studies have been carried out in this work on the effect of hydrogen in the presence of trace amounts of oxygen in $Zr_{65}Cu_{17.5}Al_{7.5}Ni_{10}$ metallic glass ribbons.

4.4.1 Effect of hydrogen on $Zr_{65}Cu_{17.5}Al_{7.5}Ni_{10}$ with 0.13 at.% oxygen

The thermal hydrogen desorption behaviour of both the $(Zr_{0.65}Cu_{0.175}Al_{0.075}Ni_{0.1})_{99.87}O_{0.13}$ and the $(Zr_{0.65}Cu_{0.175}Al_{0.075}Ni_{0.1})_{99.54}O_{0.46}$ melt-spun ribbon samples with different hydrogen contents is similar to that measured for $Zr_{55}Cu_{30}Al_{10}Ni_5$ samples with similar H/M ratios (see Fig. 4.4).

DSC scans characterising the thermal stability of $(Zr_{0.65}Cu_{0.175}Al_{0.075}Ni_{0.1})_{99.87}O_{0.13}$ samples with different amounts of hydrogen are shown in Fig. 4.10. For the **uncharged** ribbon, a distinct endothermic heat effect starts at 643 K which is related to the glass transition of the amorphous alloy. This is followed by an exothermic heat event starting at 740 K which is due to the crystallisation from the undercooled liquid. The extension of the undercooled liquid region ($\Delta T_x = T_x - T_g$) at the applied heating rate of 20 K/min is 97 K, which corresponds to literature data reported for this alloy [15, 16].

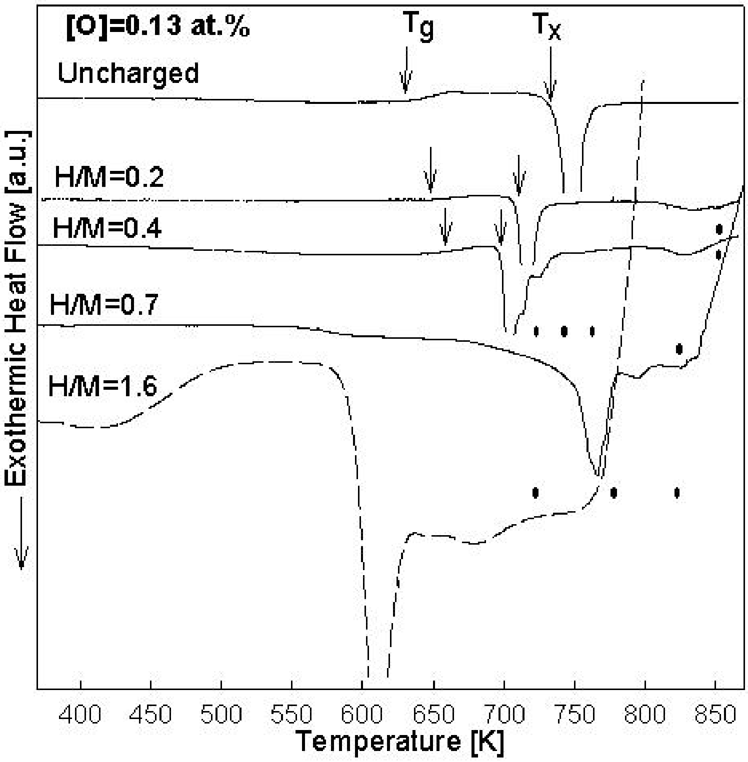

Figure 4.10: DSC scans of amorphous $(Zr_{0.65}Cu_{0.175}Al_{0.075}Ni_{0.1})_{99.87}O_{0.13}$ ribbons with different hydrogen contents using a heating rate of 20 K/min.

Absorption of small amounts of hydrogen significantly reduces the thermal stability of the ribbons. For **H/M=0.2**, T_x decreases to 709 K and T_g shifts slightly to higher temperatures resulting in a reduction of ΔT_x to 48 K. The XRD patterns shown in Fig. 4.11 give an explanation for this observed deterioration of the thermal stability. For the **uncharged** ribbon after heating to the onset temperature of crystallisation (T_x=740 K), the formation of a quasicrystalline phase was detected.

From the XRD pattern of the ribbon charged with **H/M=0.2** and heated to T_x=709 K, it is obvious that the crystallisation takes place via the formation of nanocrystalline Cu and/or Cu-rich phases, such as cubic Cu_4Al and Cu_9Al_4, a nanocrystalline fcc-type phase and the hexagonal Zr_6NiAl_2 equilibrium phase [16].

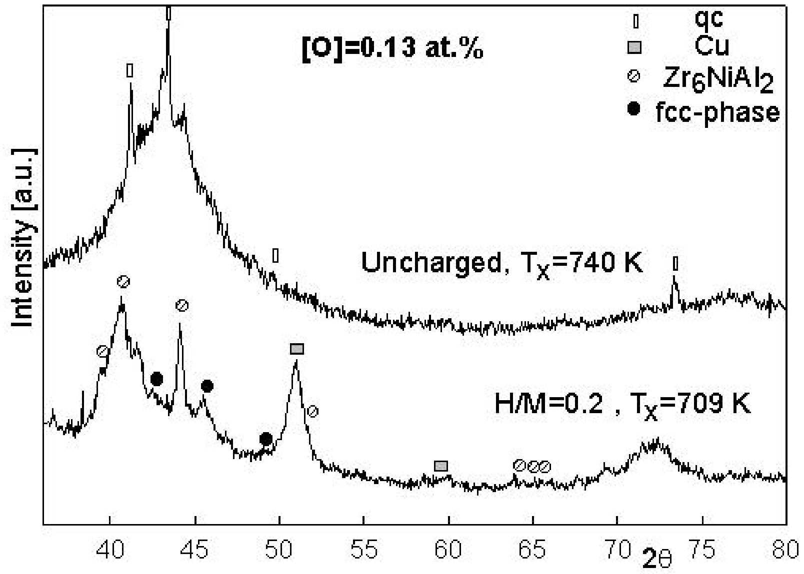

Figure 4.11: XRD patterns of uncharged and hydrogen-charged (H/M=0.2) $(Zr_{0.65}Cu_{0.175}Al_{0.075}Ni_{0.1})_{99.87}O_{0.13}$ samples after heating to the onset temperature for crystallisation (heating rate of 20 K/min) and subsequent annealing for 1 minute.

Since it is known that hydrogen atoms preferentially enter tetrahedral sites of the amorphous structure near to octahedral sites being occupied by oxygen [85] an interaction between hydrogen and oxygen atoms is assumed. Thus, upon heat treatment the stabilisation of the quasicrystalline phase by small amounts of oxygen (in that case) [16] may be prevented already by those comparatively low hydrogen concentrations. Furthermore, similar as it was observed upon charging of ribbons with very high amounts of hydrogen at room temperature and upon annealing $Zr_{55}Cu_{30}Al_{10}Ni_5$ with H/M=0.37, at higher temperatures even small amounts of hydrogen in the $(Zr_{0.65}Cu_{0.175}Al_{0.075}Ni_{0.1})_{99.87}O_{0.13}$ glassy alloy seem to induce Cu-clustering.

An increase in the hydrogen concentration to **H/M=0.4** lowers T_x to 697 K (Fig. 4.10) and an undercooled liquid region of only ΔT_x=39 K is calculated. Moreover, four distinguishable exothermic effects in the DSC scan indicate a significant change in the crystallisation process. The XRD pattern obtained after heating to the onset temperature of crystallisation (697 K), shown in Fig. 4.12, exhibits a peak indicated as the main peak of nanocrystalline Cu and/or Cu-rich phases, which occurs besides the broad maxima of the amorphous phase. At a temperature of 723 K, which corresponds to the third exothermic effect visible in the DSC scan in Fig. 4.10, peaks of another nanocrystalline phase, not yet identified by XRD analysis, occur beside the main peak of Cu and/or Cu-rich phases.

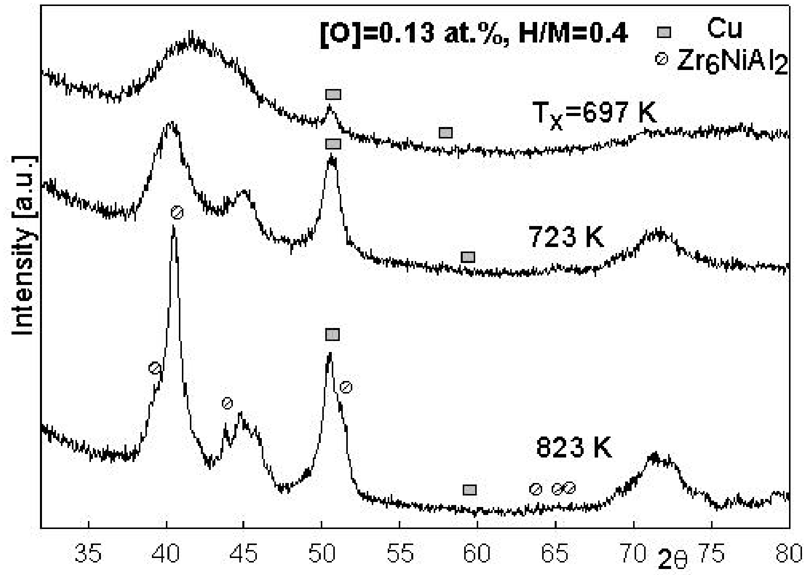

Figure 4.12: XRD patterns of hydrogenated $(Zr_{0.65}Cu_{0.175}Al_{0.075}Ni_{0.1})_{99.87}O_{0.13}$ samples (H/M=0.4) after heating to different temperatures.

Figure 4.13 shows a TEM bright-field image of the sample annealed under these conditions. Dark Cu-rich nanocrystals and bright Al-rich nanocrystals, both embedded in a contrastless amorphous matrix are visible.

After heating to 823 K, i.e. to the fourth exothermic peak, the hexagonal Zr_6NiAl_2 equilibrium phase was identified in addition to Cu and/or fcc Cu-rich phases. The tetragonal $Cu(Al,Ni)Zr_2$ phase, which was found to be another main crystalline equilibrium phase for $Zr_{65}Cu_{17.5}Al_{7.5}Ni_{10}$ alloy samples with different oxygen contents [16] , does not occur. This might suggest that under these heat treatment conditions the crystallisation process was not completed, yet. Furthermore, the preferential hydrogen-induced Cu-clustering may inhibit or even prevent the formation of this phase.

In summary, the crystallisation sequence, as indicated from the 20 K/min scan rate for the $(Zr_{0.65}Cu_{0.175}Al_{0.075}Ni_{0.1})_{99.87}O_{0.13}$ glassy alloy with **H/M= 0.4** is as follows :

(298 K): amorphous phase $\rightarrow$ (T_x= 697 K) $\rightarrow$ nc Cu/Cu-rich phase + amorphous phase(1) $\rightarrow$ (723 K) $\rightarrow$ nc Cu/Cu-rich phase + nc Al-rich phase + amorphous phase(2) $\rightarrow$ (823 K) $\rightarrow$ hexagonal Zr_6NiAl_2 phase + nc Cu/Cu-rich phase.

A hydride formation could not be detected up to a hydrogen concentration of H/M= 0.4.

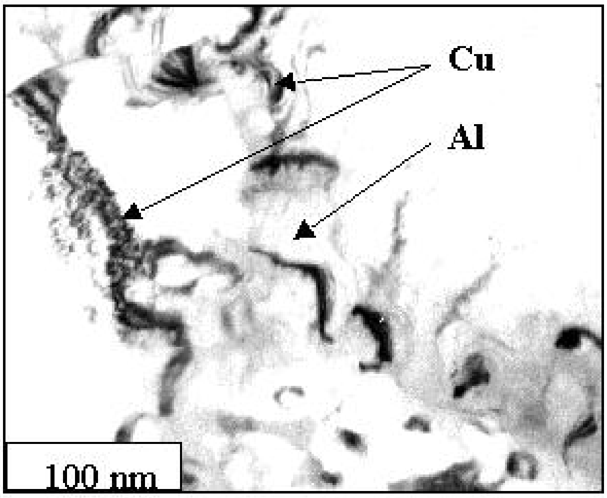

Figure 4.13: TEM bright-field image of a $(Zr_{0.65}Cu_{0.175}Al_{0.075}Ni_{0.1})_{99.87}O_{0.13}$ sample hydrogen charged to H/M=0.4 and heated to 723 K using a heating rate of 20 K/min.

The atomic ratio of hydrogen to zirconium is in this case only about 1:1 and so, the critical concentration for zirconium hydride formation is not reached, yet.

Upon increasing the amount of absorbed hydrogen to **H/M= 0.7**, the DSC curve shows no endothermic effect characteristic of a glass transition as it is visible in Fig. 4.10. Instead of this, a widely extended exothermic effect starts above 600 K. At $T_{(x)}$= 756 K a passover to a sharp exothermic peak occurs. Furthermore, a strong endothermic effect begins at 848 K.
After heating to 723 K, i.e. within the first exothermic region, $\varepsilon - ZrH_2$ is identified by XRD as the first phase formed upon crystallisation, as shown in Fig. 4.14. After heating to 743 K, i.e. slightly before the defined onset temperature of the sharp exothermic event (Fig. 4.10), mainly $\delta - ZrH_2$ is detected by XRD. At 763 K, i.e. slightly above the onset temperature, nanocrystalline Cu and/or Cu-rich phases are identified in addition to the hydride phase.

After heating to 823 K, the hexagonal Zr_6NiAl_2 phase was found in addition to Cu and/or Cu-rich phases and a smaller fraction of $\delta - ZrH_2$. After heating to 848 K, it is obvious from the XRD pattern shown in Fig. 4.14, that hydride phases do not occur anymore, but that Cu and/or Cu-rich phases are stable besides the hexagonal Zr_6NiAl_2 phase.

The indicated crystallisation sequence for the $(Zr_{0.65}Cu_{0.175}Al_{0.075}Ni_{0.1})_{99.87}O_{0.13}$ glassy alloy with **H/M= 0.7** can be expressed as follows :

298 K: amorphous phase → (723 K) → amorphous phase(I) + $\varepsilon - ZrH_2$ → (743 K) → $\delta - ZrH_2$ → (763 K) → $\delta - ZrH_2$ + nc Cu/Cu-rich phase → (823K) → $(\delta \rightarrow (\alpha + \beta)) - ZrH_x$ + nc Cu/Cu-rich phase + hexagonal Zr_6NiAl_2 phase → (848 K) → nc Cu/Cu-rich phase + hexagonal Zr_6NiAl_2 phase.

The detected primary ε-Zr-hydride formation and the transformation of this phase with

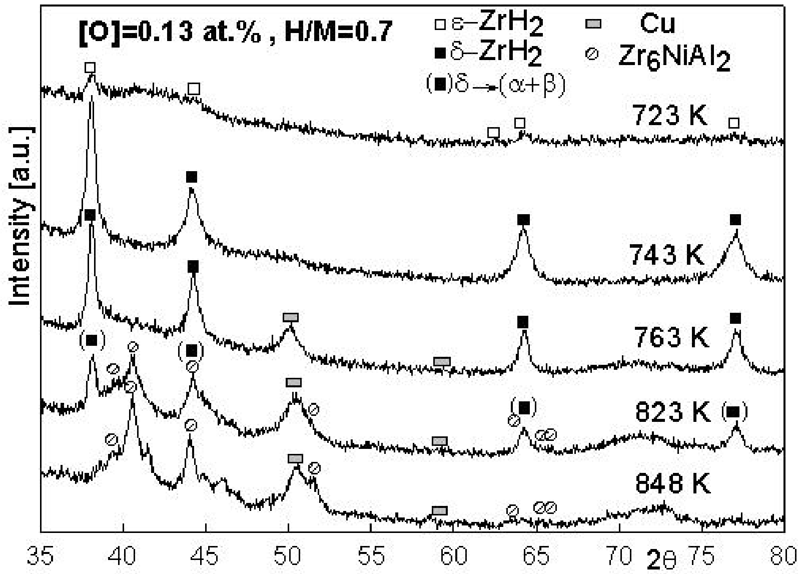

Figure 4.14: XRD patterns of the hydrogenated $(Zr_{0.65}Cu_{0.175}Al_{0.075}Ni_{0.1})_{99.87}O_{0.13}$ samples (H/M=0.7) after heating to different temperatures.

increasing temperature is in accordance to the Zr-H phase diagram [83] and was also studied in detail by thermal desorption analysis (TDA) in combination with mass spectrometry. The results are very similar to those obtained for the $Zr_{55}Cu_{30}Al_{10}Ni_5$ alloy with comparable H/M ratios [86]. The $\varepsilon - ZrH_2$, which forms at about 618 K, partially decomposes under effusion of hydrogen at temperatures above 673 K. This is followed by the transformation to crystalline Zr-hydride phases with lower hydrogen content: $\delta - ZrH_2$ at about 743 K, $(\alpha + \beta)$-Zr-H at about 813 K and complete decomposition at temperatures higher than 823 K. Zr-atoms, which are set free due to the hydride phase decomposition may be used to form the Zr_6NiAl_2 equilibrium phase. Furthermore, it is worth notifying that, at this high H/M ratio, Cu-clustering is detected the first time in the temperature region of the sharp exothermic peak visible in Fig. 4.10, i.e. after the primary $\varepsilon - ZrH_2$ formation and the beginning transformation to the δ-hydride.

The thermal behaviour of the $(Zr_{0.65}Cu_{0.175}Al_{0.075}Ni_{0.1})_{99.87}O_{0.13}$ alloy after absorption of a large amount of hydrogen **(H/M= 1.6)** is shown in Figure 4.10. An endothermic effect starts at 433 K due to hydrogen desorption from the interstitial sites with a lower affinity to hydrogen in the amorphous structure [86]. A strong exothermic peak occurs at T_x= 598 K which is - in accordance to TDA measurements and the Zr-H phase diagram - due to the formation of $\varepsilon - ZrH_2$. At higher temperatures, $\varepsilon - ZrH_2$ decomposes and partially transforms into the $\delta - ZrH_2$ phase, which, at 760 K, begins to decompose as indicated by a strong endothermic effect. Corresponding to earlier investigations [86], the $\varepsilon - ZrH_2$ decomposition shifts to lower temperatures with increasing H/M ratio.

Figure 4.15 shows XRD patterns for samples with **H/M= 1.6** taken after heating to selected temperatures above the $\varepsilon - ZrH_2$ formation temperature. At 723 K only nanocrystalline $\varepsilon - ZrH_2$ is found, while at 773 K $\delta - ZrH_2$ is the only phase identified in the pattern. This

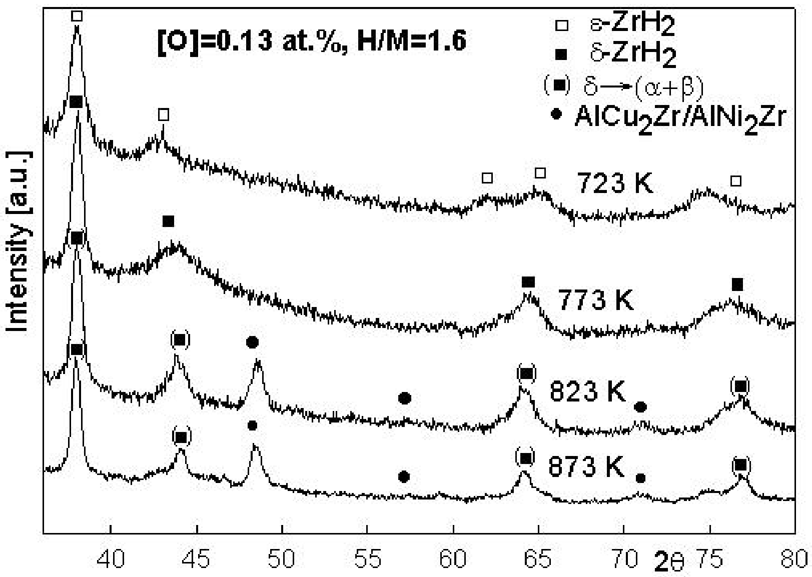

Figure 4.15: XRD patterns of hydrogenated $(Zr_{0.65}Cu_{0.175}Al_{0.075}Ni_{0.1})_{99.87}O_{0.13}$ samples (H/M=1.6) after heating to different temperatures using a heating rate of 20 K/min.

confirms the above described transformation processes.

In contrast to investigations on the $(Zr_{0.65}Cu_{0.175}Al_{0.075}Ni_{0.1})_{99.87}O_{0.13}$ alloy samples with lower hydrogen content, at 823 K new nanocrystalline Cu-rich phases, cubic $AlCu_2Zr$ and $AlNi_2Zr$, are formed in addition to the hydride phase instead of Cu and/or the Cu_4Al and Cu_9Al_4 phases and Zr_6NiAl_2. These new phases are stable also at 873 K.

It is assumed that, since most of the Zr-atoms are bound initially in hydrides, the composition of the residual amorphous matrix shifts to high concentrations of Cu, Ni and Al. A partial decomposition of hydrides at higher temperatures sets a certain number of Zr atoms free resulting in the formation of the Cu- and Ni-rich stable phases, $AlCu_2Zr$ and $AlNi_2Zr$, respectively. However, under the given heating conditions, the hydride decomposition process is not finished, yet, when 873 K are reached. This observation leads to the conclusion that when the initial hydrogen concentration increases in the amorphous alloy, the stability of the hydrides formed by annealing increases.

The crystallisation sequence for $(Zr_{0.65}Cu_{0.175}Al_{0.075}Ni_{0.1})_{99.87}O_{0.13}$ glassy alloy samples with **H/M= 1.6** can be expressed as follows:

298 K: amorphous phase $\rightarrow$ (723 K) $\rightarrow \varepsilon - ZrH_2 \rightarrow$ (773 K) $\rightarrow \delta - ZrH_2 \rightarrow$ (823 K) $\rightarrow (\delta \rightarrow (\alpha + \beta)) - ZrH_x$ + cubic $AlCu_2Zr/AlNi_2Zr$ phases $\rightarrow$ (873 K) $\rightarrow (\delta - ZrH_2 \rightarrow (\alpha + \beta)) - ZrH_x)$ + cubic $AlCu_2Zr/AlNi_2Zr$ phases.

4.4.2 Effect of hydrogen on $Zr_{65}Cu_{17.5}Al_{7.5}Ni_{10}$ with 0.46 at.% oxygen

Increasing the oxygen content of $Zr_{65}Cu_{17.5}Al_{7.5}Ni_{10}$ amorphous ribbons extends the existence region of metastable intermediate phases [16] (see section 2.1.4). DSC scans of $(Zr_{0.65}Cu_{0.175}Al_{0.075}Ni_{0.1})_{99.54}O_{0.46}$ alloy samples recorded before and after absorption of hydrogen are shown in Fig. 4.16 [87].

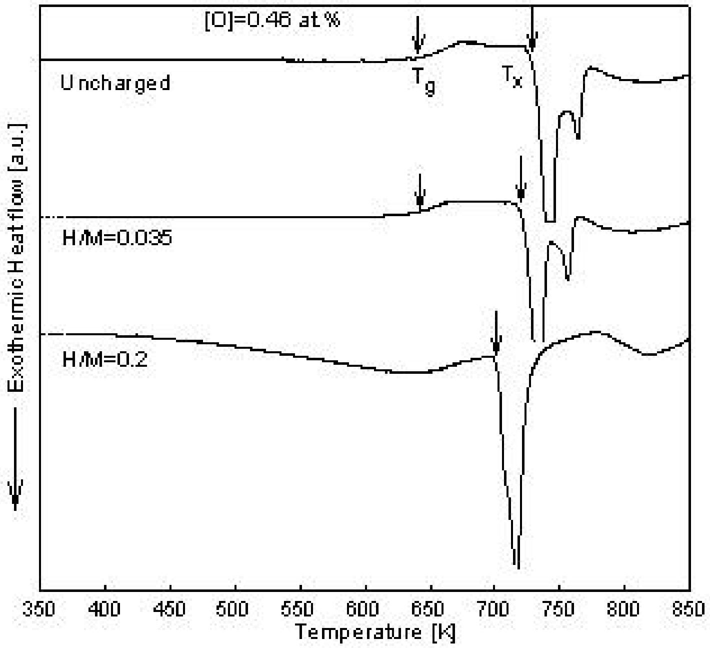

Figure 4.16: DSC scans of amorphous $(Zr_{0.65}Cu_{0.175}Al_{0.075}Ni_{0.1})_{99.54}O_{0.46}$ ribbons with different hydrogen contents using a heating rate of 20 K/min.

The **uncharged** alloy shows an undercooled liquid region of ΔT_x = 74 K, which is smaller than that for the alloy sample with 0.13 at.% oxygen content. This is followed by two characteristic successive crystallisation peaks corresponding to a primary oxygen-triggered formation of metastable phases, i.e. a quasicrystalline phase and a fcc $NiZr_2$-type phase, and their subsequent transformation to the equilibrium phases, i.e. tetragonal $CuZr_2$ and hexagonal Zr_6NiAl_2 [16].

Absorption of very small amounts of hydrogen, **H/M= 0.035**, does not lead to a significant change of the T_g onset in the DSC scan, however, the onset of the crystallisation temperature shifts to a lower temperature as observed in Fig. 4.16.

After charging the ribbon to a hydrogen content of **H/M= 0.2**, no endothermic region is visible in the DSC scan anymore and the crystallisation temperature shifts to even lower values. Only one broad crystallisation peak with a small shoulder appears at this hydrogen concentration.

The XRD pattern taken from the **uncharged** ribbon after heating to T_x= 728 K (Fig. 4.17) confirms the primary formation of the quasicrystalline and the fcc-type phase.

After heating the ribbon with **H/M= 0.035** to the onset temperature of crystallisation (T_x= 721 K), both metastable phases are also observed. However, comparing the intensities of the two phases in these two XRD patterns suggests, that for the hydrogen-charged sample the fraction of the quasicrystalline phase is reduced in comparison to that of the fcc-type phase.

After heating the sample with **H/M= 0.2** to the onset crystallisation temperature (T_x= 703 K), the metastable phases can not be identified by XRD (Fig. 4.17). Instead, similar as observed for hydrogen-charged $Zr_{65}Cu_{17.5}Al_{7.5}Ni_{10}$ samples with lower oxygen content (Fig. 4.11,4.12), nanocrystalline Cu and/or Cu- rich phases were identified as the primary phases of the crystallisation process.
At 740 K, the metastable fcc-type phase and the hexagonal Zr_6NiAl_2 equilibrium phase were detected in addition to Cu and/or Cu rich phases (Fig. 4.17).

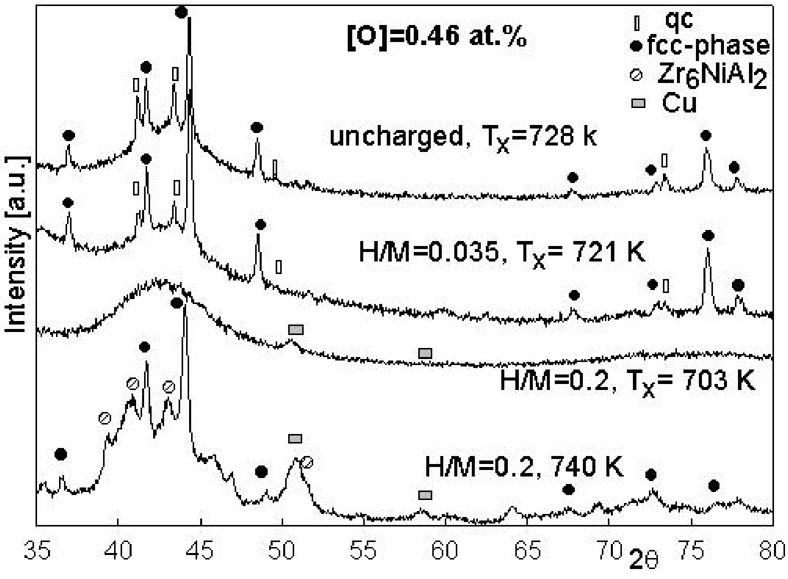

Figure 4.17: XRD patterns of $(Zr_{0.65}Cu_{0.175}Al_{0.075}Ni_{0.1})_{99.54}O_{0.46}$ samples with different hydrogen contents after heating to different temperatures using a heating rate of 20 K/min.

These results indicate, that hydrogen inhibits the oxygen-triggered formation of the quasicrystalline phase in $Zr_{65}Cu_{17.5}Al_{7.5}Ni_{10}$ samples with 0.46 at.% oxygen similar as it was already shown for $Zr_{65}Cu_{17.5}Al_{7.5}Ni_{10}$ ribbons with 0.13 at.% oxygen. In contrast, the formation of the fcc-type phase, also triggered by oxygen, is obviously less affected by hydrogen.

The addition of a very small amount of hydrogen (H/M= 0.035), corresponding to a hydrogen-to-oxygen atomic concentration ratio of 7.5:1, is not sufficient to completely suppress the quasicrystalline phase formation. This suggests, that not all tetrahedral sites in the amorphous structure near to octahedral sites being occupied by oxygen atoms are entered by interacting hydrogen atoms. Only for an excess of hydrogen atoms at H/M= 0.2, the hydrogen-to-oxygen atomic concentration ratio of 44:1 is high enough to completely prevent the formation of the complex-structured quasicrystals. Alternatively, hydrogen-induced Cu-clustering processes appear as primary crystallisation step.

For higher hydrogen contents, $0.2 < H/M \leq 1.6$, the thermal behaviour and the crystallisation processes of the $Zr_{65}Cu_{17.5}Al_{7.5}Ni_{10}$ alloy samples with 0.46 at.% oxygen were found to be very similar to those described for alloy samples with 0.13 at.% oxygen [87].

4.5 Conclusions

- In all of the investigated amorphous compositions $Zr_{55}Cu_{30}Al_{10}Ni_5$ and $Zr_{65}Cu_{17.5}Al_{7.5}Ni_{10}$ alloys, hydrogen reduces the number of zirconium atoms by preferential formation and transformation of crystalline Zr-hydride phases above 623 K causing an enrichment in the other elements (Al, Cu, Ni) in the amorphous matrix.
- The thermal stability and the crystallisation behaviour of $Zr_{55}Cu_{30}Al_{10}Ni_5$ and $Zr_{65}Cu_{17.5}Al_{7.5}Ni_{10}$ metallic glasses strongly depend on the amount of hydrogen in the alloy. Already small amounts of hydrogen in the amorphous alloy cause a deterioration of its thermal stability, i.e a diminution of the undercooled liquid region mostly resulting from a decrease of the crystallisation temperature.
- At higher hydrogen contents the thermal stability of $Zr_{55}Cu_{30}Al_{10}Ni_5$ and $Zr_{65}Cu_{17.5}Al_{7.5}Ni_{10}$ alloys is determined by the Zr-hydride formation and transformation to hydrogen-poorer phases accompanied by hydrogen effusion. The transformation of different hydride phases takes place in the order of tetragonal ε-Zr-hydride, cubic δ-Zr hydride and a mixture of $(\alpha + \beta)$-Zr-hydride.
- The $Zr_{55}Cu_{30}Al_{10}Ni_5$ amorphous alloy charged by hydrogen to a low H/M-ratio of 0.37 crystallises via the formation of the hexagonal $AlZr_2$ phase accompanied by the formation of Cu clusters at 753 K. For high hydrogen contents of $0.7 < H/M < 1$, the cubic $AlCu_2Zr$ phase forms already at 713 K. In contrast, the uncharged $Zr_{55}Cu_{30}Al_{10}Ni_5$ ribbon crystallises at 771 K by the formation of a mixture of fcc $NiZr_2$ type metastable phase, orthorhombic NiZr and tetragonal $CuZr_2$ phases.

Investigations on the effect of hydrogen ($H/M \leq 1.6$) on the thermal behaviour of amorphous $Zr_{65}Cu_{17.5}Al_{7.5}Ni_{10}$ alloy samples with 0.13 and 0.46 at.% oxygen show that the phase transformation processes upon heating of these Zr-Al-Cu-Ni-O-H samples are of a very complex nature. However, the following conclusions can be drawn [87]:

- Hydrogen deteriorates the thermal stability of glassy $Zr_{65}Cu_{17.5}Al_{7.5}Ni_{10}$ alloy samples. With increasing hydrogen content a reduction of the undercooled liquid region mainly resulting from a decrease of the crystallisation temperature is observed. At very high hydrogen concentrations, the Zr-hydride formation and a subsequent decomposition dominate the thermal characteristics (DSC scan) of the alloy samples.
- Similarly, as it was detected for other alloy compositions [38], hydrogen suppresses the oxygen-triggered formation of the quasicrystalline intermediate phase upon heating. However, a significant excess of hydrogen atoms in the amorphous phase compared to the

number of oxygen atoms present is necessary to completely prevent the stabilisation of quasicrystals. In contrast, the metastable fcc-type phase formation is obviously not affected by hydrogen.

- For low hydrogen concentrations (H/M $\leq$ 0.4) in the $Zr_{65}Cu_{17.5}Al_{7.5}Ni_{10}$ alloy and upon annealing the hydrogenated alloy samples, hydrogen supports Cu-segregation processes similar to that for high hydrogen contents of H/M=1.3 at room temperature (Fig. 4.3), so that, nanocrystalline Cu and/or Cu-rich phases (such as Cu_4Al or Cu_9Al_4) are detected as primary phases in the crystallisation process being stable also at higher temperatures for alloy samples with both investigated oxygen contents.
- At higher H/M ratios, after severe Zr-hydride formation and a beginning decomposition, new stable Cu(Ni)-rich phases (cubic $AlCu_2Zr$/$AlNi_2Zr$) appear. Obviously, the preferential Zr-hydride formation causes an enrichment of Cu, Ni and Al in the residual amorphous phase, which results in the crystallisation of new intermetallic compounds.
- The presence of oxygen in trace amounts (0.13 and 0.46 at.%) does not affect the formation/transformation or decomposition of hydride phases under the used detection limits.

Chapter 5

Cathodic characteristics of Zr-based alloys

5.1 Hydrogen reactions on the surface of Zr-based alloys

Electrochemical tests were carried out to study the cathodic hydrogen reactions on the surface of the glassy Zr-Cu-Al-Ni ribbons in alkaline electrolyte. Both, the $Zr_{55}Cu_{30}Al_{10}Ni_5$ and the $Zr_{65}Cu_{17.5}Al_{7.5}Ni_{10}$ alloys exhibited a similar electrochemical behaviour. So, in this section, cathodic hydrogen reactions will be discussed only for the $Zr_{55}Cu_{30}Al_{10}Ni_5$ alloy as an example for both compositions.

A characteristic polarisation curve for a freshly polished $Zr_{55}Cu_{30}Al_{10}Ni_5$ alloy sample recorded at a potential scan of 2 mV/sec in deaerated 0.1M NaOH electrolyte containing $5 * 10^{-5}$ mol/l arsenic trioxide as hydrogen promoter at pH= 13 is displayed in Fig. 5.1. The cathodic region of the semi-logarithmic current density-potential plot, the so-called "Tafel plot", corresponds mainly to the hydrogen discharge reaction on the ribbon sample surface without any other considered contributions to side reactions or other effects that may arise on the surface, e.g. oxide layer formation.

The cathodic current density-potential plot displays an increase of the cathodic current density (i_c) immediately after the mixed potential (E'). This increase is followed by a plateau which is characterised by an insignificant variation of i_c over a wide range of the potential. After the plateau region, i_c increases once again.

According to the i_c behaviour, it is possible to divide the cathodic potential region to three regions. The *Tafel region* is the region where i_c increases from E' till the beginning of the plateau. The end of this region is indicated by the potential at point (a), at the intersection of the extrapolated tangent of the increasing i_c slope and the extrapolated tangent of the plateau (see Fig. 5.1).

The *second cathodic region* is the region of the current density plateau, i.e. i_c is almost independent on the potential. It begins from point (a) and ends at point (b) as illustrated in Fig. 5.1. Point (b) is defined by the intersection of the extrapolated tangent of the plateau and the slope of the second increasing i_c curve. The cathodic current density at point (b) is defined

as the limiting cathodic current density ($i_{l,c}$).
The third cathodic region corresponds to the second increasing i_c region starting at point (b). This cathodic polarisation plot is reproducible for the $Zr_{55}Cu_{30}Al_{10}Ni_5$ alloy as well as for the $Zr_{65}Cu_{17.5}Al_{7.5}Ni_{10}$ alloy.

Since the electrolytic medium used in these investigations is alkaline, 0.1 M NaOH+5 $* 10^{-5}$ mol/l As_2O_3, at pH=13, hydrogen discharge and adsorption take place in the cathodic potential region by the reduction of water molecules (Volmer reaction in alkaline medium, reaction [2.7]), expressed as:

$$H_2O + e^- \rightarrow H_{ads} + OH^- \tag{5.1}$$

Also, since Zr has the highest affinity towards hydrogen with respect to the other alloy elements, Cu, Al and Ni, it is assumed that hydrogen discharge and adsorption on the alloy surface take place initially on the Zr sites.

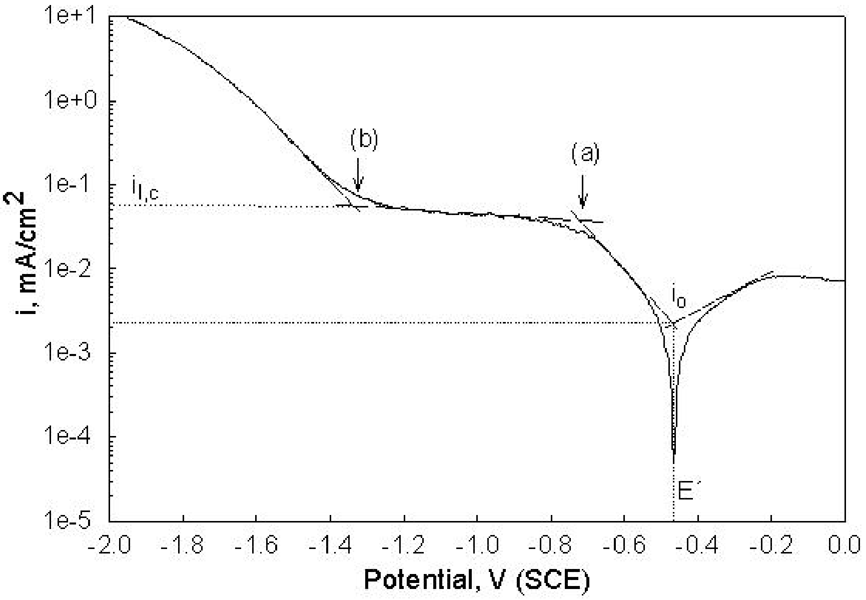

Figure 5.1: Potentiodynamic polarisation plot of the uncharged $Zr_{55}Cu_{30}Al_{10}Ni_5$ sample recorded in deaerated 0.1 M NaOH+5 $* 10^{-5}$ mol/l As_2O_3 solution using a scan rate of 2 mV/s.

The E' of the $Zr_{55}Cu_{30}Al_{10}Ni_5$ alloy is -0.468 V versus the saturated calomel electrode (SCE), and according to the standard potential–pH equilibrium diagram (Pourbaix diagram) for hydrogen at pH=13 [88], the hydrogen evolution reaction (line (a) in Pourbaix diagrams) takes place at -0.527 V versus SCE as follows:

$$2H^+ + 2e^- \rightleftharpoons H_2 \tag{5.2}$$

This means that the measured mixed potential E' of the $Zr_{55}Cu_{30}Al_{10}Ni_5$ alloy is very close to the equilibrium potential (E_{eq}) of the hydrogen evolution reaction, thus the possibility of hydrogen evolution to occur is taking place almost from the beginning of the cathodic polarisation region.

In the **Tafel region** (first cathodic region) and from the cathodic Tafel slope, it is possible to give a proposal for the mechanism of hydrogen reactions which may take place in this region. In Fig. 5.1, the estimated cathodic Tafel slope of the amorphous $Zr_{55}Cu_{30}Al_{10}Ni_5$ alloy is equal to **0.14 V/dec**.

From Butler-Volmer equation, Bockris et al [89] have derived estimated values of the transfer coefficient (α_t), and hence the Tafel slope from which one can predict the rate-determining step of the hydrogen evolution reaction as tabulated in table 5.1:

Table 5.1: Kinetic derivatives for mechanisms of the hydrogen evolution reaction.

Mechanism	α_t	Tafel slope
Rate-determining *hydrogen discharge* followed by chemical desorption	0.5	$\frac{2RT}{F} \equiv 0.44$ V
Hydrogen discharge followed by rate-determining *chemical desorption*	2	$\frac{RT}{2F} \equiv 0.11$ V
Hydrogen discharge followed by rate-determining *electrodic desorption*	1.5	$\frac{2RT}{3F} \equiv$ **0.147 V**

Comparing the Tafel slope derivatives for hydrogen evolution reaction mechanisms and the Tafel slope calculated from the polarisation curve of the $Zr_{55}Cu_{30}Al_{10}Ni_5$ alloy in Fig. 5.1, one may propose that the mechanism of the hydrogen reactions in the Tafel region is the hydrogen discharge and adsorption on the sample surface (D), Volmer reaction, followed by a rate-determining *electrodic desorption* reaction step (ED), *Heyrowsky reaction* (2.9). This mechanism is convenient since the amorphous Zr-based alloy has a high affinity towards hydrogen, hence it is expected that hydrogen discharge is a fast step. This mechanism can be expressed as follows;

$$H_2O + e^- \overset{D}{\rightleftharpoons} H_{ads} + OH^- \qquad \text{fast step} \tag{5.3}$$

$$H_{ads} + H_2O + e^- \overset{ED}{\rightarrow} H_2 + OH^- \qquad \text{rate} - \text{determining step} \tag{5.4}$$

Bockris et al [90, 91] proposed a model for the hydrogen entry into the metal. In this model, which was mainly developed for steel, the hydrogen absorption and the hydrogen recombination reactions (chemical and electrodic desorption) are competing, and the absorption reaction is a fast step meaning that equilibrium is attained rapidly and the step proceeds with a small activation energy. According to this model, and since the amorphous Zr-based alloy has a high affinity towards hydrogen absorption, it is proposed that the hydrogen absorption reaction occurs in the Tafel region of the $Zr_{55}Cu_{30}Al_{10}Ni_5$ alloy, and it is a fast competing reaction to the rate-determining electrodic desorption step.

Therefore the mechanism of hydrogen reactions in the *Tafel region* (Fig. 5.1) can be summarised in the following sequence:

$$H_2O + e^- \overset{D}{\rightleftharpoons} H_{ads} + OH^- \qquad \text{fast step} \tag{5.5}$$

$$\mathrm{H_{ads} + H_2O + e^-} \overset{\mathrm{ED}}{\rightarrow} \mathrm{H_2 + OH^-} \qquad \text{rate} - \text{determining step} \tag{5.6}$$

$$\downarrow$$

$$\mathrm{H_{ads}} \rightarrow \mathrm{H_{abs}} \qquad \text{fast competing step} \tag{5.7}$$

For the **plateau region** (second potential region), sample rotation at different speeds was carried out to study the effect of mass transfer. Fig. 5.2 illustrates the convection effect on the cathodic polarisation behaviour using 1000 and 2000 rpm in comparison with stagnant solution conditions. It is obvious in Fig. 5.2 that convection has no significant effect on the Tafel region, and for all rotation speeds a Tafel slope of 0.14 V/dec was estimated.

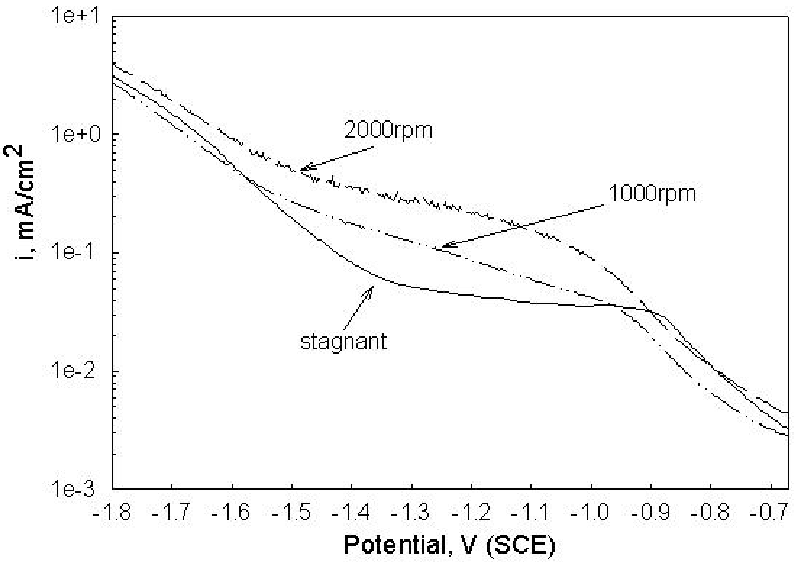

Figure 5.2: Potentiodynamic polarisation curves of a glassy $Zr_{55}Cu_{30}Al_{10}Ni_5$ sample measured in deaerated 0.1 M NaOH+5 $*\ 10^{-5}$ mol/l As_2O_3 solution using a scan rate of 2 mV/s; under stagnant conditions; sample rotation at 1000 rpm and sample rotation at 2000 rpm.

On the other hand, the plateau region has been significantly affected by rotation in a way that the plateau current density increases by increasing the rotating speed. It is also noticed that after applying rotation (curve b and c), the current density of the plateau region is not parallel to the current density plateau under stagnant conditions (curve a), but rather shows a positive increasing slope (see Fig. 5.2). From this observation, one can deduce that the plateau is due to that both reaction steps (5.3, 5.4) take place at the same rate. Furthermore, the rate-determining step becomes the mass transfer of the protons from the solution to the sample surface. Rotation increases the number of protons reaching the electrode surface and getting discharged, i.e. the rate of reaction (5.3) increases, therefore the current density increases. At the same time, when the rate of reaction (5.3) increases, reactions [5.3, 5.4] are no longer taking place at the same rate. This results in the noticed positive increase of the current density slope in the plateau region by rotation (curve b and c) in comparison with the current density plateau under stagnant condition (curve a) under these polarisation conditions.

The mechanism of hydrogen reactions in the plateau region in Fig. 5.1 is mainly diffusion-controlled where step reactions (5.3, 5.4) are occurring at the *same rate*, and the hydrogen absorption reaction (5.7) is still a competing reaction for the electrodic desorption reaction.

Fig. 5.3 elucidates the diffusion-controlled mechanism occurring in the cathodic current density plateau region by forward and backward scan cycles. The experiment started under stagnant conditions passing by the plateau of the second region. At -1 V, lying in the plateau region (point a), sample rotation was applied at 1000 rpm. It is obvious from Fig. 5.3 that i_c immediately increases at point (a) due to the rotation exhibiting a small positive current density slope after point (a), i.e. the current density plateau after point (a) is not parallel to the current density plateau before point (a) but rather shows a small slope. At -1.15 V (point b), still lying in the i_c plateau region, the rotation speed was raised to 2000 rpm. This results in a further increase in i_c. During the backward cycle scan, the rotation was stopped at -1.24 V (point c) which lies in the plateau region. When the rotation stops, i_c exhibits a continuous decrease till it almost attains the plateau current density level of the forward stagnant condition curve at -0.98 V, (before point a), and forms a plateau similar to the stagnant condition curve. This means that by stopping the rotation, the rate of hydrogen discharge reaction (5.3) is gradually attaining the rate of hydrogen electrodic desorption (5.4) and the hydrogen reactions once again are taking place under the diffusion-controlled mechanism in this region as discussed above.

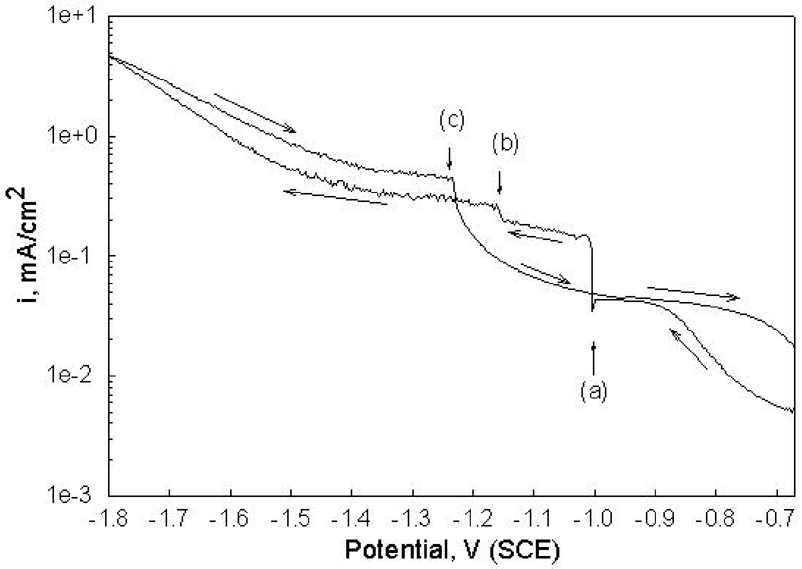

Figure 5.3: Potentiodynamic cyclic polarisation of glassy $Zr_{55}Cu_{30}Al_{10}Ni_5$ sample recorded in deaerated 0.1 M NaOH+$5 * 10^{-5}$ mol/l As_2O_3 solution using a scan rate of 2 mV/s.

In the **third cathodic region** (Fig. 5.1), i_c increases with increasing negative potential. This means that either the hydrogen discharge reaction (5.3) or the hydrogen electrodic desorption reaction (5.4) is occurring at a higher rate than the other. The mechanism in this region is no longer diffusion-controlled, but it is difficult to propose which reaction (5.3 or 5.4) is predominant. In general, at such high negative potentials all the reactions (5.5, 5.6 and 5.7) are taking place at higher rates than in the first and the second cathodic potential regions. Interestingly the slope of the increasing i_c curve in the third region is equal to the Tafel slope of the first cathodic region.

The two sides of the $Zr_{55}Cu_{30}Al_{10}Ni_5$ and $Zr_{65}Cu_{17.5}Al_{7.5}Ni_{10}$ metallic glass ribbons are a) the *dull side* which was in contact with the copper wheel during the preparation process and b) the *shiny side* which was not in contact with the wheel. The polarisation behaviour of both sides shows no significant difference, and the AES analysis gives no difference in the atomic concentration of the alloy elements for both sides.

5.1.1 Comparison between multi-phase crystalline and amorphous phases

A comparison between the polarisation behaviour of both a freshly polished amorphous $Zr_{55}Cu_{30}Al_{10}Ni_5$ ribbon and a fully multi-phase crystalline $Zr_{55}Cu_{30}Al_{10}Ni_5$ plate is shown in Fig. 5.4. Besides, the polarisation curve of the amorphous $Zr_{65}Cu_{17.5}Al_{7.5}Ni_{10}$ alloy is also displayed in the same figure. All the samples shown in the plot contain a low oxygen amount of 0.13 at.%. It is obvious that all the samples exhibit similar general features of the polarisation plot. The cathodic Tafel slope of all the samples is almost the same, meaning that the hydrogen reaction mechanism of the three samples is similar to that discussed before for the amorphous $Zr_{55}Cu_{30}Al_{10}Ni_5$ alloy.

Comparing the polarisation curves of the multi-phase crystalline and the amorphous $Zr_{55}Cu_{30}Al_{10}Ni_5$ alloys, the cathodic current density of the amorphous alloy is higher than that of the multi-phase crystalline alloy. The $E^{'}$ of the crystalline material as well as the i_o value are lower than the $E^{'}$ and the i_o value of the amorphous phase (see table 5.2), indicating a higher surface reactivity of the amorphous alloy.
The parameters estimated from the cathodic polarisation plot, shown in table 5.2, reveal that the limiting cathodic current density ($i_{l,c}$) of the amorphous phase is higher than that of the crystalline one. The width of the second cathodic region for both multi-crystalline and the amorphous phases is almost equal ($\simeq$ 0.6 V).
From these results, one may deduce that the electrochemical reactivity of the hydrogen reduction is higher on the surface of the Zr-based amorphous alloy than on the surface of the multi-crystalline Zr-based alloy. Since the electrodic desorption of hydrogen is the rate-determining step for both phases and also, since the exchange current density i_o of the amorphous sample is higher than the exchange current density of the multi-crystalline one, the hydrogen evolution reaction rate is enhanced on the amorphous alloy surface [89]. This may be due to the fact that the amorphous alloy is a single phase homogeneous material. Also, the amorphous phase has a higher number of coordinative unsaturated surface atoms. Thus it can provide a high number of electrons for the hydrogen reduction and shows a high electrocatalytic activity.

Comparing the polarisation plots of the glassy $Zr_{55}Cu_{30}Al_{10}Ni_5$ and $Zr_{65}Cu_{17.5}Al_{7.5}Ni_{10}$ ribbons as shown in Fig. 5.4, it is obvious that the i_c, i_o and $i_{l,c}$ (see table 5.2) of the $Zr_{65}Cu_{17.5}Al_{7.5}Ni_{10}$ alloy composition are higher than those of $Zr_{55}Cu_{30}Al_{10}Ni_5$, but the difference in $E^{'}$ between them is too small to be considered ($\Delta E^{'}$=0.016 V) as tabulated in table 5.2. From these re-

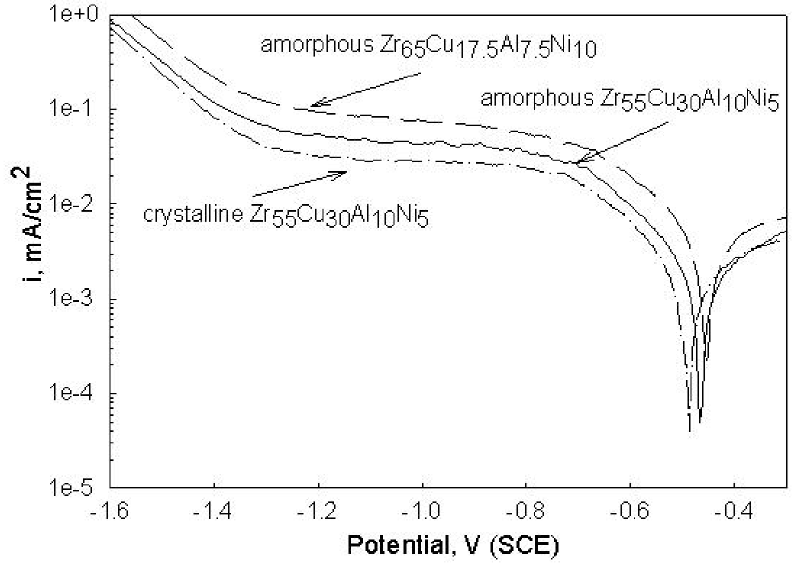

Figure 5.4: Potentiodynamic polarisation curves of the $Zr_{55}Cu_{30}Al_{10}Ni_5$ metallic glass, the $Zr_{65}Cu_{17.5}Al_{7.5}Ni_{10}$ metallic glass and the crystalline $Zr_{55}Cu_{30}Al_{10}Ni_5$ alloy recorded in deaerated 0.1 M NaOH+$5 * 10^{-5}$ mol/l As_2O_3 solution using a scan rate of 2 mV/s.

sults, one may conclude that the electrochemical reactivity of the hydrogen reduction and the hydrogen evolution reaction rate on the $Zr_{65}Cu_{17.5}Al_{7.5}Ni_{10}$ alloy is higher than that on the $Zr_{55}Cu_{30}Al_{10}Ni_5$ alloy. This may be the reason for the observed slow hydrogen absorption rate of the $Zr_{65}Cu_{17.5}Al_{7.5}Ni_{10}$ ribbon compared with the $Zr_{55}Cu_{30}Al_{10}Ni_5$ one in Fig. 4.2.

One may speculate whether the stoichiometric difference and/or the surface packing density are playing a role for the observed slow hydrogen absorption rate and high hydrogen electrocatalytic reactivity of the $Zr_{65}Cu_{17.5}Al_{7.5}Ni_{10}$ alloy in comparison with the $Zr_{55}Cu_{30}Al_{10}Ni_5$ alloy. Since the $Zr_{65}Cu_{17.5}Al_{7.5}Ni_{10}$ alloy contains more Zr and Ni, the surface coverage with adsorbed hydrogen atoms is higher than for the $Zr_{55}Cu_{30}Al_{10}Ni_5$ alloy which may increase the probability of recombination of the adsorbed hydrogen atoms.

Table 5.2: Parameters estimated from Tafel plots of crystalline and amorphous $Zr_{55}Cu_{30}Al_{10}Ni_5$ alloys and amorphous $Zr_{65}Cu_{17.5}Al_{7.5}Ni_{10}$ alloy

Tafel parameters	A55	C55	A65
i_o (mA/cm^2 $* 10^{-2}$)	2.4	1.5	3.6
E' (V) vs SCE	-0.468	-0.484	-0.454
$i_{l,c}$ (mA/cm^2 $* 10^{-2}$)	4.8	3.4	12

A55 *is amorphous* $Zr_{55}Cu_{30}Al_{10}Ni_5$ *alloy;* **C55** *is multi-crystalline* $Zr_{55}Cu_{30}Al_{10}Ni_5$ *alloy and* **A65** *is amorphous* $Zr_{65}Cu_{17.5}Al_{7.5}Ni_{10}$ *alloy.*

5.1.2 Effect of oxygen in Zr-based alloys

The polarisation curves of $Zr_{55}Cu_{30}Al_{10}Ni_5$ metallic glass ribbons with different oxygen contents (0.13 and 0.58 at.%) are displayed in Fig. 5.5. It is observed that E' is shifted to a higher value for the sample with lower oxygen content. Fig. 5.6 shows that E' exhibits a first order increase by lowering the oxygen content for samples containing less than 1 at.% oxygen. This means that the presence of the oxygen decreases the alloy resistance to the alkaline medium.

Tafel slope does not change for the samples containing oxygen less than one atomic percent.

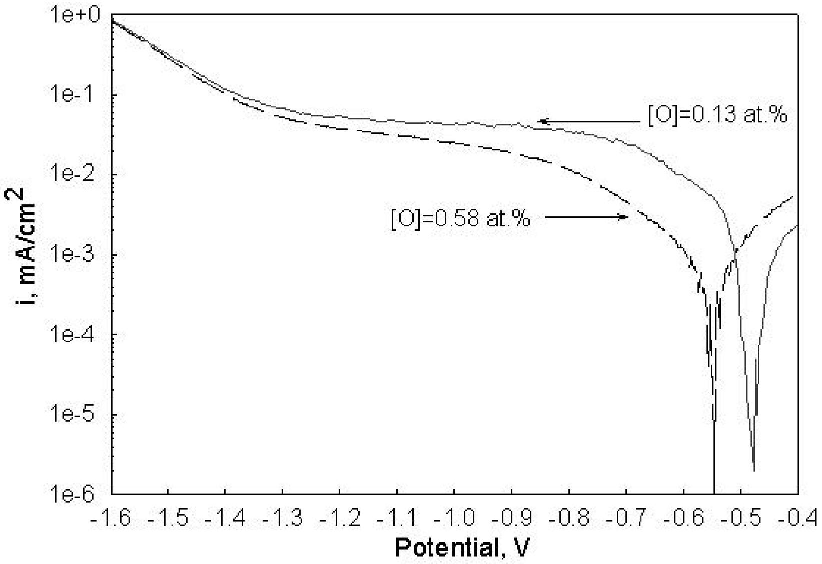

Figure 5.5: Tafel plots of $Zr_{55}Cu_{30}Al_{10}Ni_5$ metallic glasses with different oxygen content measured in deaerated 0.1 M NaOH+$5 * 10^{-5}$ mol/l As_2O_3 solution using a scan rate of 2 mV/s.

This means that the mechanism of hydrogen reactions on the amorphous Zr-based alloy is not affected by such small oxygen concentrations. On the other hand, the cathodic current density of the sample with 0.13 at.% oxygen is higher than that of the sample of 0.58 at.% in the first and the second cathodic regions. Maybe oxygen has a small effect on the atomic arrangement or /and the atomic concentration of the surface in a way that the hydrogen discharge decreases by increasing the oxygen concentration.

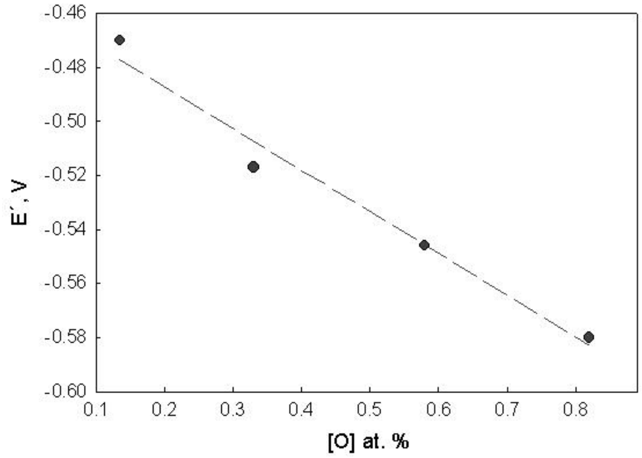

Figure 5.6: Relation between E' and oxygen content of $Zr_{55}Cu_{30}Al_{10}Ni_5$ metallic glass ribbons.

5.1.3 Conclusions

- The cathodic polarisation behaviour, as-expressed in terms of semi-logarithmic current density-potential plots (Tafel-plots), of amorphous $Zr_{55}Cu_{30}Al_{10}Ni_5$ and $Zr_{65}Cu_{17.5}Al_{7.5}Ni_{10}$ alloys reveals three characteristic regions :
  1 . In the Tafel region, hydrogen discharge and adsorption (Volmer reaction) take place on the surface of the alloy as a fast step followed by the rate-determining electrodic desorption step (Heyrowsky reaction) in competition with hydrogen absorption as a fast step.
  2 . In the second region, a current density plateau occurs, i.e. the current density is independent of the potential as both the Volmer and the Heyrowsky reactions take place at the same rate and the hydrogen mass transfer from the solution to the electrode surface is the rate-determining step, i.e. the mechanism is diffusion controlled.
  3 . In the third region, the cathodic current density increases, and the mechanism is no longer diffusion-controlled. It is proposed that all the processes (hydrogen discharge, hydrogen electrodic desorption, hydrogen absorption and maybe also hydrogen chemical desorption) take place intensively but it is difficult to define which reaction (Volmer reaction or Heyrowsky reaction) is predominant.

- Multi-phase crystalline and amorphous Zr-based quaternary alloys exhibit the same hydrogen reaction mechanism. But the electrochemical activity of the surface of the amorphous alloy is higher than that of the multi-phase crystalline alloy. Since the exchange current density of the amorphous sample is higher than that of the multi-phase crystalline sample, the hydrogen evolution, i.e. the Heyrowsky reaction, is enhanced on the amorphous alloy. This maybe due to the fact that the amorphous alloy is a single phase homogeneous material. Also, the amorphous alloy has a higher number of coordinative unsaturated surface atoms, thus it can provide a high number of electrons for the hydrogen reduction and shows a high electrocatalytic activity.

- Similar hydrogen reactions mechanism takes place on the surface of the $Zr_{55}Cu_{30}Al_{10}Ni_5$

and $Zr_{65}Cu_{17.5}Al_{7.5}Ni_{10}$ alloys. But the electrochemical activity of the surface of the amorphous $Zr_{65}Cu_{17.5}Al_{7.5}Ni_{10}$ alloy is higher than that of the $Zr_{55}Cu_{30}Al_{10}Ni_5$ alloy in a way, that the cathodic current density and the exchange current density of the amorphous $Zr_{65}Cu_{17.5}Al_{7.5}Ni_{10}$ alloy are higher than those of $Zr_{55}Cu_{30}Al_{10}Ni_5$ alloy. In combination with the observed slow hydrogen absorption rate of $Zr_{65}Cu_{17.5}Al_{7.5}Ni_{10}$ alloy in subchapter 4.1 (Fig. 4.2), one may assume that since the $Zr_{65}Cu_{17.5}Al_{7.5}Ni_{10}$ alloy has a higher Zr and Ni content, it has a higher surface coverage of adsorbed hydrogen atoms and this may increase the probability of the adsorbed hydrogen atoms to recombine.

- The presence of trace amounts of oxygen (less than 1 at.%) in the amorphous Zr-based alloys does not influence the mechanism of hydrogen reactions on the alloy surface, but it decreases the resistance of the alloy to the surrounding medium.

5.2 Influence of hydrogen absorption on hydrogen reactions

5.2.1 Hydrogen reactions on the surface of hydrogenated-samples

The polarisation curves of differently hydrogenated $Zr_{55}Cu_{30}Al_{10}Ni_5$ alloy ribbons of H/M=0.17 and H/M=1.2 and of the equivalent uncharged sample ribbon for comparison are displayed in Fig. 5.7; all the curves in the plot are for samples containing 0.33 at.% oxygen.

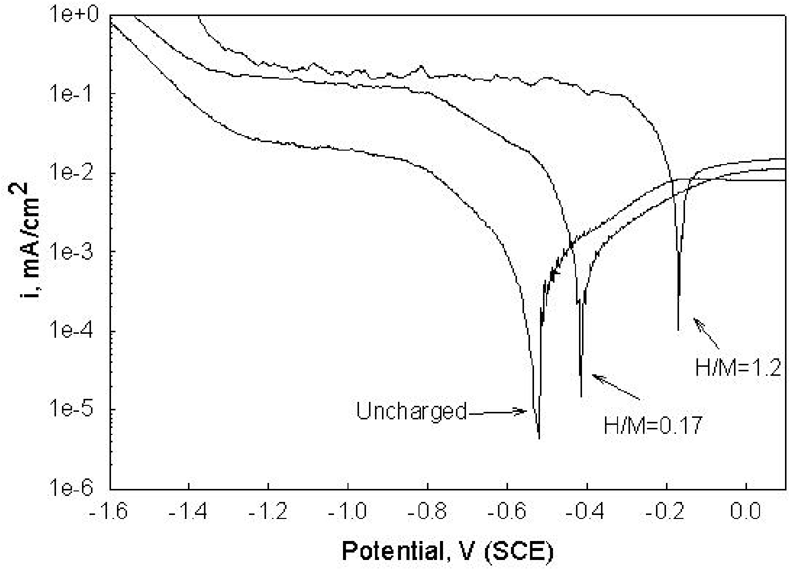

Figure 5.7: Potentiodynamic polarisation curves of uncharged and hydrogenated $Zr_{55}Cu_{30}Al_{10}Ni_5$ metallic glass samples with different hydrogen concentrations recorded in deaerated 0.1 M NaOH+$5 * 10^{-5}$ mol/l As_2O_3 solution using a scan rate of 2 mV/s.

Obviously, there are significant changes in the Tafel plot due to the presence of hydrogen in the ribbon. The mixed potential E' shifts to higher values by increasing the hydrogen concentration in the samples, the cathodic current density i_c increases over the whole cathodic potential range, and the exchange current density i_o increases too.

The increase of the E' and of the i_o with increasing hydrogen concentration in the amorphous $Zr_{55}Cu_{30}Al_{10}Ni_5$ alloy is shown in Fig. 5.8. The mixed potential exhibits a linear increase by increasing the hydrogen content, while the exchange current density exhibits a non-linear increase by increasing the hydrogen content.

The increase of i_o means that the hydrogen evolution reaction increases on the alloy surface, so one may conclude that the presence of hydrogen in the amorphous Zr-based alloy increases the surface reactivity for the hydrogen evolution reaction. This may be due to the filling of hydrogen into the interstitial sites in the amorphous phase which may reduce the rate of hydrogen absorption reaction (5.7) and, by its turn, hydrogen evolution reaction is enhanced.

Hydrogen absorption by the amorphous Zr-based alloy rearranges the amorphous matrix in a way that mainly Zr is depleted on the surface and a Cu enrichment takes place as was discussed before in subchapter 4.1. These changes of the amorphous surface may also play a role to enhance the hydrogen evolution reaction on the precharged sample surface since it is known that the hydrogen evolution reaction is induced on the Cu surface rather than on the Zr surface [92].

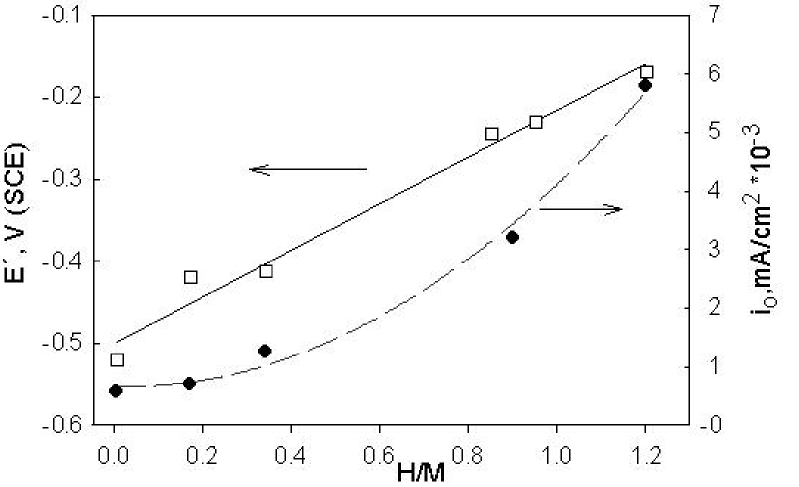

Figure 5.8: Variation of mixed potential E' (left Y-axis); exchange current density i_o (right Y-axis) with hydrogen content in the amorphous $Zr_{55}Cu_{30}Al_{10}Ni_5$ metallic glass.

The Cu enrichment on the surface is also the reason for the observed shift of the E'. This is proved by measuring the open circuit potential of the uncharged and hydrogenated $Zr_{55}Cu_{30}Al_{10}Ni_5$ samples in comparison to a crystalline copper rod sample in 0.1M NaOH solution with arsenic trioxide as shown in Fig. 5.9. It is obvious that the open circuit potentials of the hydrogenated samples are more positive than that of the uncharged sample. Besides, the open circuit potential of the precharged sample up to H/M=0.9 is closer to the open circuit potential

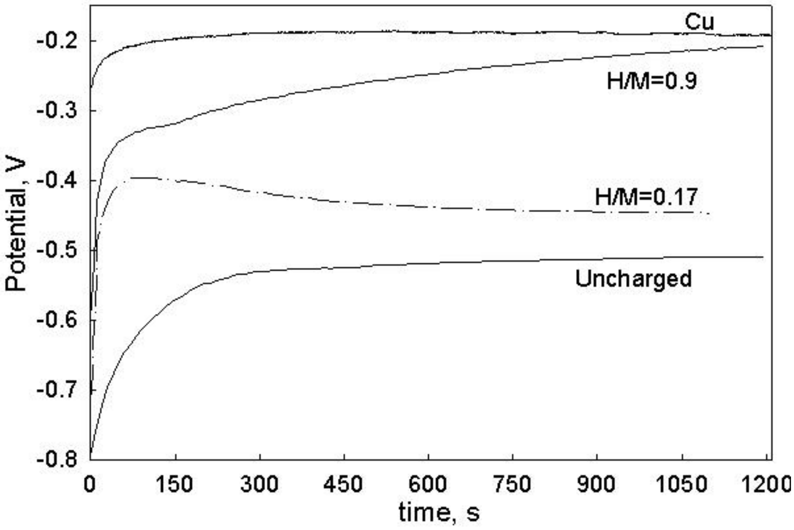

Figure 5.9: The open circuit potential curves of uncharged and hydrogenated $Zr_{55}Cu_{30}Al_{10}Ni_5$ samples and a crystalline copper rod in deaerated 0.1 M NaOH+$5 * 10^{-5}$ mol/l As_2O_3.

of the crystalline Cu sample. A similar behaviour was obtained for the $Zr_{65}Cu_{17.5}Al_{7.5}Ni_{10}$ alloy.

In Fig. 5.7, in the first cathodic region (Tafel region), the estimated Tafel slopes of the precharged samples change, as tabulated in table 5.3, indicating that there is a change in the hydrogen reaction mechanism due to the presence of hydrogen. The Tafel slope decreases after charging the samples with hydrogen. By comparing these values (0.1 and 0.085 V/dec) with the values of the kinetic derivatives for mechanisms of the hydrogen evolution reaction (table 5.1), it was found that the Tafel slope of precharged samples are comparable with the 0.11 V value in table 5.1. Hence, it is proposed that the hydrogen reactions mechanism on the surface of the hydrogenated samples is a fast hydrogen discharge reaction followed by a rate-determining chemical desorption (CD) step. This can be expressed in the following sequence:

$$\mathrm{H_2O + e^-} \overset{\mathrm{D}}{\rightleftharpoons} \mathrm{H_{ads} + OH^-} \qquad \text{fast step} \tag{5.8}$$

$$\mathrm{H_{ads} + H_{ads}} \overset{\mathrm{CD}}{\rightarrow} \mathrm{H_2} \qquad \text{rate} - \text{determining step} \tag{5.9}$$

The Tafel potential region (ΔE_T) of the hydrogenated samples is smaller than that of the uncharged sample, e.g. ΔE_T of the uncharged sample and the sample hydrogenated up to H/M=1.2 are 0.252 and 0.156 V, respectively. This means that the steady state, where reactions (5.8) and (5.9) occur at the same rate, is attained faster on the surface of the precharged sample.

In the second cathodic region, the hydrogenated samples exhibit a wider plateau than the uncharged sample (see table 5.1). This means that the mass transfer of hydrogen protons from the solution to the sample surface is the rate-determining step and that reactions (5.8) and (5.9) take place at the same rate. The observed disturbance of the current plateau of the sample precharged with H/M=1.2 may be due to the increase of the surface roughness when hydrogen

is absorbed as observed before by SEM (see Fig. 4.1). Also the fine precipitation of Zr-hydride in the hydrogenated sample, as discussed before in subchapter 4.1, may show a disturbed current density curve in the plateau region.
Cyclic voltamograms performed on the highly precharged $Zr_{55}Cu_{30}Al_{10}Ni_5$ sample (H/M= 1.2) and on the uncharged one ensure the reproducibility of the wide disturbed i_c plateau region in the case of hydrogenated $Zr_{55}Cu_{30}Al_{10}Ni_5$ for five cycles.

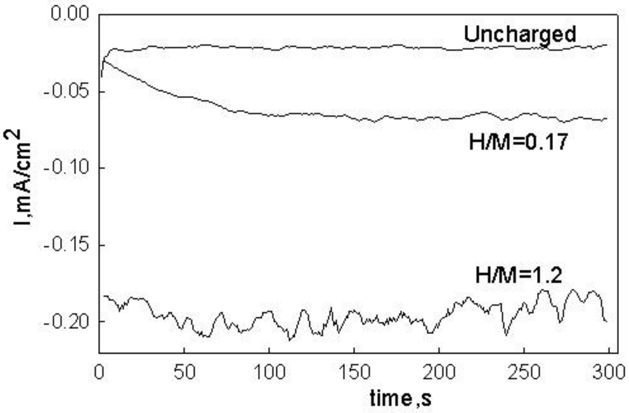

Figure 5.10: Current-time curves during cathodic potentiostatic charging at -1.2 V of uncharged $Zr_{55}Cu_{30}Al_{10}Ni_5$ metallic glass sample and hydrogenated samples up to H/M=0.17 and H/M=1.2.

Table 5.3: Parameters estimated from Tafel plots of amorphous $Zr_{55}Cu_{30}Al_{10}Ni_5$ alloys with different hydrogen contents

Polarisation parameters	H(0)	H (0.17)	H (1.2)
Tafel slope (V/dec)	0.148	0.1	0.085
Plateau width (V)	0.5	0.58	1

H(0) *is the uncharged amorphous* $Zr_{55}Cu_{30}Al_{10}Ni_5$ *alloy;* **H(0.17)** *is the sample containing H/M=0.17 and* **H(1.2)** *is the sample containing H/M=1.2*

In Fig. 5.10, as-prepared $Zr_{55}Cu_{30}Al_{10}Ni_5$ sample and precharged samples up to H/M=0.17 and 1.2 are potentiostatically charged at -1.2 V. Fig. 5.10 reveals that the precharged samples display more negative current densities and the current density decreases by increasing the amount of hydrogen in the Zr-based ribbons. This confirms that the hydrogen discharge reaction is induced on the surface of the precharged samples. Also the displayed current density of the highly hydrogenated sample is disturbed.

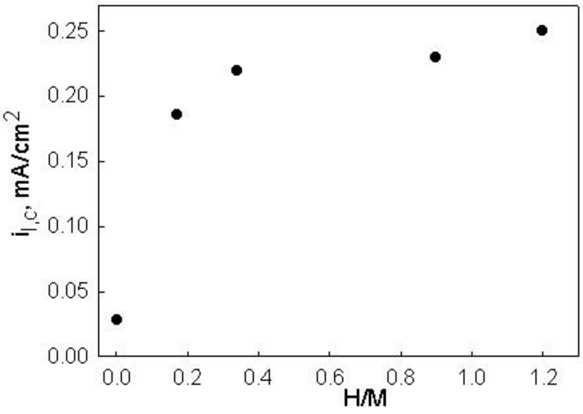

Figure 5.11: Variation of ($i_{l,c}$) with H/M of $Zr_{55}Cu_{30}Al_{10}Ni_5$ metallic glass.

The increase of the limiting cathodic current density ($i_{l,c}$) with the hydrogen concentration in the alloy is displayed in Fig. 5.11. It is clear that the presence of even small amounts of hydrogen in the alloy, for example H/M=0.17, results in a significant increase of $i_{l,c}$. On the other hand, the increase of the $i_{l,c}$ values from H/M=0.17 up to H/M=1.2 exhibit a small influence. In other words, the $i_{l,c}$ difference between the uncharged sample and the sample with H/M=0.17 is 0.158 mA/cm^2 and the $i_{l,c}$ difference between the sample of H/M=0.17 and the sample of H/M=1.2 is 0.064 mA/cm^2. Since a lot of events take place by introducing hydrogen in the amorphous Zr-based alloys, it is difficult to define which one can be responsible for this observation.

5.2.2 Conclusions

- The polarisation behaviour of the hydrogen-precharged amorphous $Zr_{55}Cu_{30}Al_{10}Ni_5$ alloy shows a significant change of the Tafel parameters compared with the uncharged alloy. The mixed potential increases as Cu segregates on the alloy surface. The electrochemical reactivity also increases by increasing the hydrogen concentration in the amorphous Zr-based alloy. It might be that the filling of hydrogen into the interstitial sites in the amorphous phase reduces the affinity of the precharged samples towards hydrogen absorption and consequently enhances the hydrogen evolution reaction on the alloy surface. Also, as discussed in subchapter 4.1, the presence of hydrogen in the amorphous Zr-based alloy changes the atomic concentration of the alloying elements on the alloy surface and may also change the atomic arrangement in a way that the Zr concentration is reduced on the surface, while a Cu enrichment takes place. This may induce the hydrogen evolution reaction on the alloy surface, since the hydrogen evolution reaction is induced on the Cu-rich surface rather than on the Zr-rich surface.

- The Tafel slope of the hydrogenated samples is smaller than that of the uncharged sample, in a way that the mechanism tends to change from a hydrogen discharge step followed by a rate-determining hydrogen electrodic desorption step (Volmer-Heyrowsky reaction mechanism) for the uncharged Zr-based alloy to a hydrogen discharge step followed by a rate-determining hydrogen chemical desorption step (Volmer-Tafel reaction mechanism) for the precharged Zr-based alloy.

- In the cathodic polarisation plot, the first cathodic potential region of the precharged alloy curve is smaller than that of the uncharged alloy curve, while the second potential region (current density plateau region) of the precharged alloy curve is wider than that of the uncharged alloy curve. This means that the steady state, where both reaction steps take place at the same rate, of the precharged alloy (Volmer-Tafel reaction mechanism) is attained faster on the hydrogenated samples than on the uncharged one (Volmer-Heyrowsky reaction mechanism) and that the mass transfer of the protons from the solution to the sample surface (rate-determining step) is applied over a wider potential range in case of hydrogen precharged samples.
  The disturbance of the current density plateau in the second cathodic region in case of the highly charged sample (H/M=1.2) is maybe due to the increase of the surface roughness or the precipitation of Zr-hydrides.

- The limiting cathodic current density $i_{l,c}$ increases significantly upon precharging the Zr-based alloy with even low hydrogen concentrations (H/M=0.17). While the increase in $i_{l,c}$ from the sample with H/M=0.17 to the sample of H/M=1.2 is not significant. It is difficult to find the reason for this $i_{l,c}$ behaviour since a lot of events take place due to the presence of hydrogen in the alloy.

5.3 Reversibility of hydrogen absorption

The reversibility of absorbed hydrogen atoms was studied by means of the potentiostatic double pulse technique for both the $Zr_{55}Cu_{30}Al_{10}Ni_5$ and the $Zr_{65}Cu_{17.5}Al_{7.5}Ni_{10}$ metallic glasses. The method is described in details in subchapter 3.5.2.
For the Zr-based alloy ribbons the selected applied charging potentials (E_c) were -1 and -1.2 V lying in the plateau region of the Tafel plot, and -1.5 V lying in the third potential region. Both studied metallic glass alloy compositions exhibit the same general behaviour. Therefore, the $Zr_{55}Cu_{30}Al_{10}Ni_5$ ribbon containing 0.33 at.% oxygen will be discussed in detail in this section as an example for both alloy compositions.

After charging an amorphous $Zr_{55}Cu_{30}Al_{10}Ni_5$ alloy sample by hydrogen at **-1 V** for **one minute** charging time (t_c) and then discharge it, the developed current density transient i_d for one pulse is shown in Fig. 5.12. The first 50 seconds of the transient time (t_d) is displayed in Fig. 5.12. i_d decreases till it is nearly equal to zero.

By solving Fick's second law considering the surface charging conditions, a relation between i_d and the diffusion coefficient D_* is drawn as expressed before by equation (3.2) in suchapter 3.5.3. The dependence of the *transient current density* i_d on the *time term*, $\mathrm{t_d^{-1/2}} - (\mathrm{t_c} + \mathrm{t_d})^{-1/2}$, for one minute charging time (t_c) at -1 V is represented in Fig. 5.13. Selected curves are revealed in Fig. 5.13 for the second, third, eighth and tenth pulse named as P2, P3, P8 and P10, respectively. P2 and P3 display a linear dependence of i_d on the time term. On the other

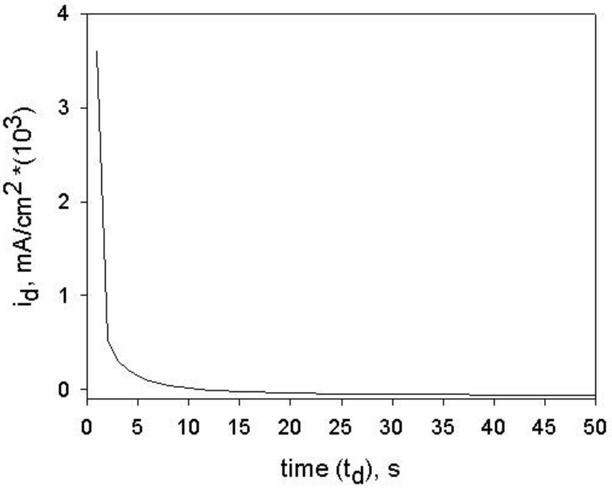

Figure 5.12: Part of the current/time transients for $Zr_{55}Cu_{30}Al_{10}Ni_5$ metallic glass ribbons after charging at -1 V for 1 min.

hand, P8 and P10 display non-linear dependence.

To summarise the dependence of i_d on the time term $\mathrm{t_d^{-1/2}} - (\mathrm{t_c} + \mathrm{t_d})^{-1/2}$ for 15 hydrogen charging pulses at -1 V for one minute, it is found that i_d shows a linear dependence on the time term from the first till the sixth pulse, and a non-linear dependence from the seventh till the fifteenth pulse.

According to a statistical model derived for hydrogen diffusion and trapping in metals [79, 93], the linear dependence of i_d on the time term is due to hydrogen desorption and oxidation from non-trapped sites, while the non-linear dependence of i_d on the time term is due to hydrogen desorption and oxidation from trapped interstitial sites.
One may assume that after applying 15 hydrogen charging/discharging pulses for charging conditions of -1 V for one minute, the linear dependence of i_d on the time term from P1 to P6 can be discussed in terms of the hydrogen desorption from the non-trapping reversible sites and the non-linear relation given from P7 to P15 can be discussed as the desorption of the hydrogen from the trapping reversible sites.
In case of the hydrogen desorption from the non-trapping reversible sites, it is assumed that the reversibly absorbed hydrogen atoms were mainly located in the material close to the entry side. while, in case of the hydrogen desorption from the trapping reversible sites, it is assumed that the reversibly absorbed hydrogen atoms were mainly occupying a fraction of the high energy trapping units in the amorphous phase.
On the other hand, there was no detected increase in the residual hydrogen in the amorphous $Zr_{55}Cu_{30}Al_{10}Ni_5$ sample after 15 absorption/desorption pulses at -1 V for 1 minute charging time when it is compared with the as-prepared sample as tabulated in table 5.4. This indicates that there are no detected irreversibly absorbed hydrogen atoms under these detection limit.

Increasing the charging pulse time to **3 minutes** at **-1 V**, the current/time transients for 15

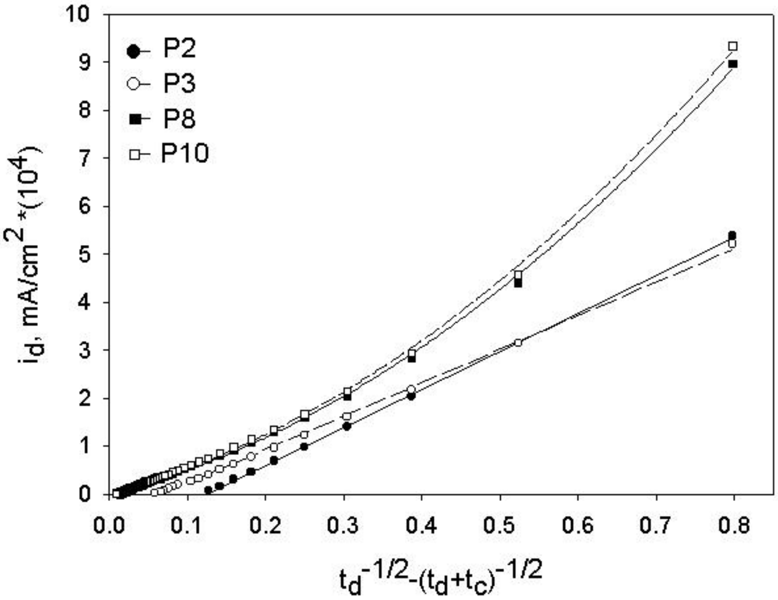

Figure 5.13: Dependence of i_d on the time term $(\mathrm{t_d^{-1/2}} - (\mathrm{t_c} + \mathrm{t_d})^{-1/2})$ for $Zr_{55}Cu_{30}Al_{10}Ni_5$ metallic glass ribbons after charging at -1V for 1 min.

pulses exhibit a similar behaviour as in Fig. 5.12 but it shows higher i_d values. The first and the second pulse (P1 and P2) give a linear dependence of i_d on the time term and from P3 till P15, exhibit a non-linear relation. In table 5.4, the residual hydrogen increases after this test in comparison to the as-prepared sample.

This means that, by increasing the charging time the amount of hydrogen absorbed increases which increases the possibility of hydrogen to diffuse and to occupy reversible trapping sites as well as irreversible trapping sites.

Table 5.4: The estimated residual hydrogen for the as-prepared amorphous $Zr_{55}Cu_{30}Al_{10}Ni_5$ sample and the samples after applying 15 absorption/desorption pulses for different charging pulse conditions

Charging pulse conditions	Residual H/M values
as-prepared sample (reference)	0.0025
At -1 V for 1 minute	0.0017
At -1 V for 3 minutes	0.006
At -1.2 V for 1 minutes	0.004
At -1.5 V for 1 minute	0.008

Applying a charging pulse of **-1.2 V** for **two minutes** charging time, the current/time transients exhibit a reproducible "hump" for the 15 pulses. This hump is also reproducible when a charging pulse of -1.2 V is applied from 3 to 5 minutes. Additionally, the hump occurs in the case of a -1.5 V charging pulse for 1 minute till 5 minutes. Fig 5.14 shows part of the transients for different pulse conditions where the hump appears for $Zr_{55}Cu_{30}Al_{10}Ni_5$ samples. Similarly, the hump was detected for amorphous $Zr_{65}Cu_{17.5}Al_{7.5}Ni_{10}$ samples.

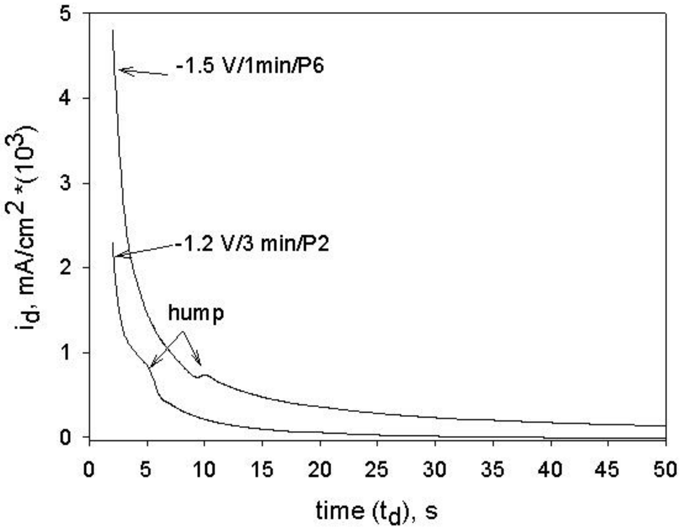

Figure 5.14: Part of the current/time transients for $Zr_{55}Cu_{30}Al_{10}Ni_5$ metallic glass ribbons for different charging pulse conditions.

The reproducibility of the "hump" at relatively high charging pulse conditions is speculated to be due to the desorption and oxidation of the hydrogen atoms from different types of reversible trapping sites which might be energetically different.

The residual hydrogen left in the samples increases by lowering the applied charging potential pulse, meaning that more hydrogen is trapped in irreversible trapping sites by increasing the amount of absorbed hydrogen during the charging pulse (see table 5.4).

5.3.1 Estimation of the anodic charge

The anodic charge (q_a), which is equivalent to the amount of the diffused hydrogen back to the entry side and oxidised at the surface of the amorphous $Zr_{55}Cu_{30}Al_{10}Ni_5$ sample during the discharging pulse, was estimated from the current-time transients for ten pulses at different hydrogen charging potentials (E_c), -1, -1.2 and -1.5 V for 1 minute charging duration. The anodic charge q_a is plotted versus the pulse number in Fig. 5.15. It is clear that the anodic charge q_a increases by lowering the applied hydrogen charging potential E_c, meaning that more hydrogen is absorbed during the hydrogen charging pulse and consequently desorbed during the hydrogen discharging pulse. For all hydrogen charging potentials shown in Fig. 5.15, q_a increases in the beginning, then it remains almost constant at higher pulse numbers. It is assumed that by applying successive hydrogen charging pulses the thin oxide layer, which is readily formed

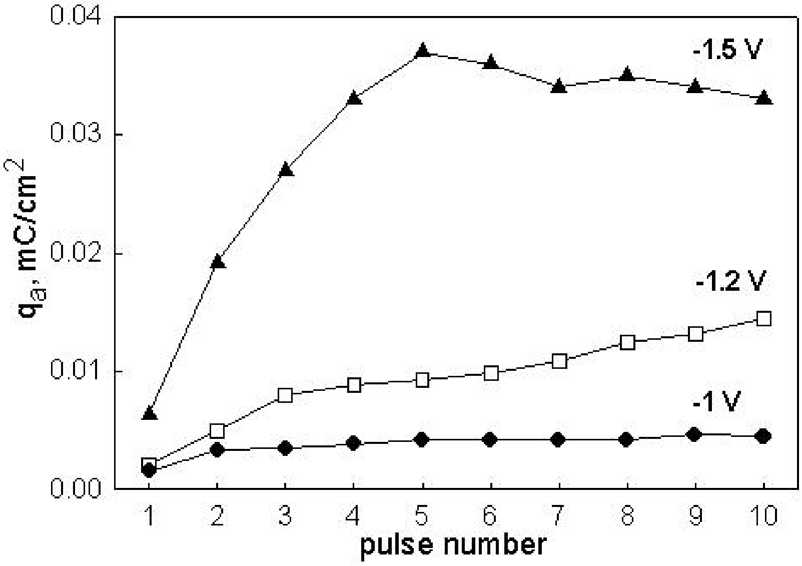

Figure 5.15: Relation between q_a and the number of charging pulses at E_c= -1, -1.2 and -1.5 V for 1 minute duration for the amorphous $Zr_{55}Cu_{30}Al_{10}Ni_5$ samples.

on the sample surface, is reduced. After that, the amount of the reversibly absorbed hydrogen that can be attained from the hydrogen charge/discharge pulses is almost constant.

A relation between the hydrogen charging duration from 1 to 4 minutes and the average anodic charge q_a calculated for ten pulses at different charging potentials, -1 and -1.5 V is plotted in Fig. 5.16. It is obvious that the average anodic charge q_a increases by prolonging the hydrogen charging duration till 3 minutes, while for 4 minutes duration the average anodic charge q_a decreases. Besides, the residual hydrogen in the samples after applying the test increases by prolonging the charging duration.
This can be interpreted in a way that, as the hydrogen charging duration increases more hydrogen is absorbed by the samples during the hydrogen charging pulse. A longer charging time gives the chance for more fractions of the absorbed hydrogen atoms to diffuse into the sample and to occupy the irreversible trapping sites which is energetically favourable for hydrogen. This is proposed to be the reason for the observed decrease in the average anodic charge q_a when the charging time increases.

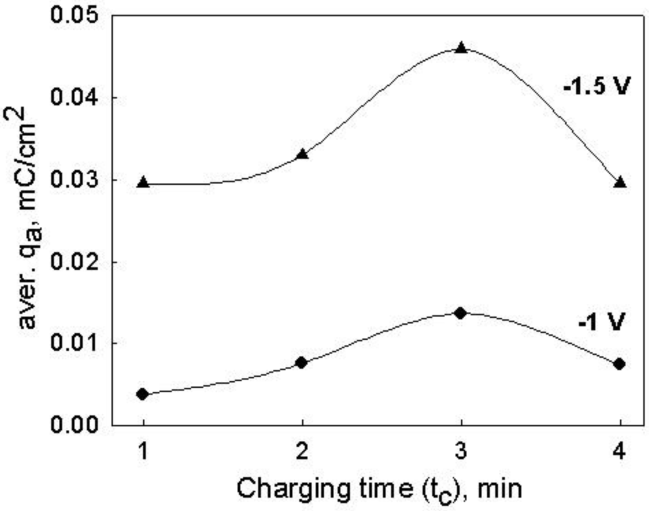

Figure 5.16: Relation between the average q_a of ten pulses and the charging duration for charging pulse at -1 and -1.5 V.

5.3.2 Anodic charge of crystalline and amorphous samples

A comparison between the anodic charge q_a of the amorphous $Zr_{55}Cu_{30}Al_{10}Ni_5$ alloy, the multicrystalline $Zr_{55}Cu_{30}Al_{10}Ni_5$ alloy and the amorphous $Zr_{65}Cu_{17.5}Al_{7.5}Ni_{10}$ alloy is illustrated in Fig. 5.17. All the samples contained 0.13 at.% oxygen.

The multicrystalline $Zr_{55}Cu_{30}Al_{10}Ni_5$ alloy has the highest q_a followed by the amorphous $Zr_{55}Cu_{30}Al_{10}Ni_5$ alloy and then the amorphous $Zr_{65}Cu_{17.5}Al_{7.5}Ni_{10}$ alloy. This means that the multicrystalline phase is able to absorb and consequently desorb more hydrogen than the amorphous phase for the Zr-based alloys. Also the amorphous $Zr_{55}Cu_{30}Al_{10}Ni_5$ alloy has a higher ability to absorb/desorb hydrogen than the amorphous $Zr_{65}Cu_{17.5}Al_{7.5}Ni_{10}$ alloy.

These results are in agreement with the results discussed in subchapter 4.1, Fig. 4.2, which show that the rate of the hydrogen absorption of the amorphous $Zr_{65}Cu_{17.5}Al_{7.5}Ni_{10}$ alloy is slower than the rate of the hydrogen absorption of the amorphous $Zr_{55}Cu_{30}Al_{10}Ni_5$ alloy, although the $Zr_{65}Cu_{17.5}Al_{7.5}Ni_{10}$ composition contains more Zr and Ni (good hydrogen absorbers) and less Cu (good hydrogen evolution catalyst) than the $Zr_{55}Cu_{30}Al_{10}Ni_5$ composition.
Also the potentiodynamic polarisation in Fig. 5.4 proposes that the hydrogen evolution reaction on the surface of the amorphous $Zr_{65}Cu_{17.5}Al_{7.5}Ni_{10}$ alloy is higher than the hydrogen evolution reaction on the surface of the amorphous $Zr_{55}Cu_{30}Al_{10}Ni_5$ alloy. The presence of more Zr and Ni on the surface of the amorphous $Zr_{65}Cu_{17.5}Al_{7.5}Ni_{10}$ alloy increases the surface coverage with discharged hydrogen atoms, maybe this increases the probability of recombination of the discharged hydrogen atoms on the surface.

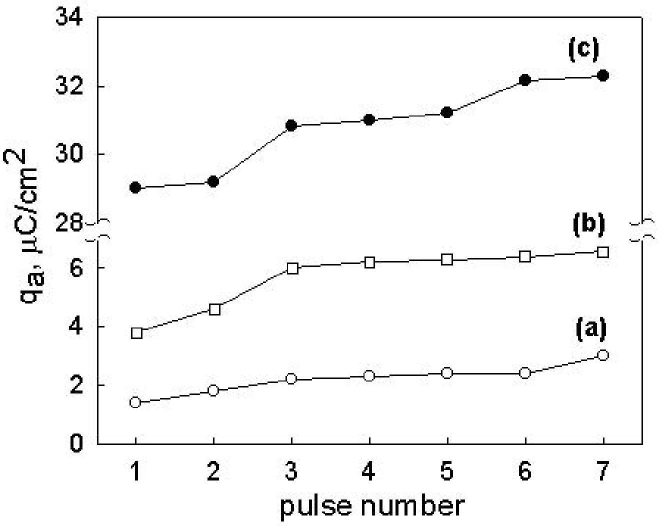

Figure 5.17: Relation between the anodic charge q_a and the pulse number for (a) the amorphous $Zr_{65}Cu_{17.5}Al_{7.5}Ni_{10}$; (b) the amorphous $Zr_{55}Cu_{30}Al_{10}Ni_5$ and (c) the multicrystalline $Zr_{55}Cu_{30}Al_{10}Ni_5$ for a charging pulse of -1 V applied for 1 minute.

5.3.3 Effect of the presence of oxygen

Samples of $Zr_{65}Cu_{17.5}Al_{7.5}Ni_{10}$ metallic glass ribbons with low and high oxygen content (0.13 at.% and 0.82 at.% oxygen) were used to study the effect of oxygen on the anodic charge q_a for different hydrogen charging conditions (E_c= -1 V for 1 minute hydrogen charging duration and E_c= -1.2 V for 3 minutes hydrogen charging duration) as shown in Fig. 5.18. It is clear that for the same charging conditions, the anodic charge q_a is higher for the samples with the lower oxygen content.

These results support the assumption that oxygen is hindering the absorption of hydrogen as it occupies some interstitial sites which hydrogen prefers to occupy in the amorphous phase and/or the presence of oxygen in the alloy reduces the surface activity of the alloy towards hydrogen absorption.

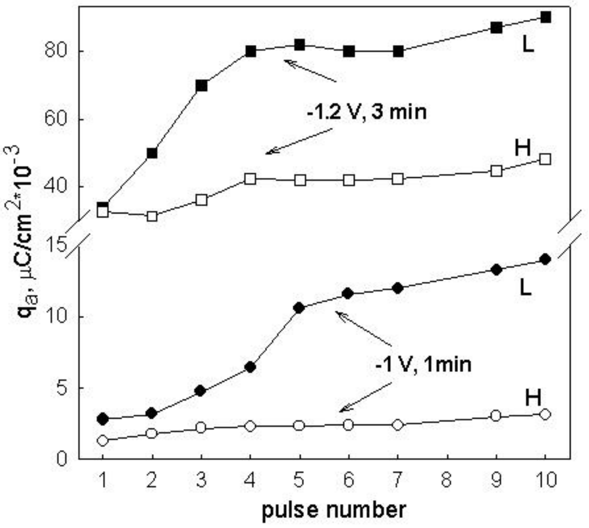

Figure 5.18: Relation between q_a and the pulse number for amorphous $Zr_{65}Cu_{17.5}Al_{7.5}Ni_{10}$ samples with 0.13 at.% oxygen (L-symbol) and 0.82 at.% oxygen (H-symbol) for charging pulses at -1 V for 1 minute and at -1.2 V for 3 minutes.

5.3.4 Conclusions

- The reversibility of the hydrogen absorption by the amorphous $Zr_{55}Cu_{30}Al_{10}Ni_5$ and $Zr_{65}Cu_{17.5}Al_{7.5}Ni_{10}$ alloys was studied by means of the potentiostatic double pulse technique.
  Under low charging pulse conditions, e.g. -1 V for 1 minute, hydrogen is reversibly desorbed from non-trapping sites possibly located close to the entry sample surface. Increasing the number of pulses more reversible hydrogen is desorbed (q_a increases), maybe due to the reduction of the thin oxide layer. This increases the possibility for the absorbed hydrogen to occupy reversible trapping sites in the sample. After that, the anodic charge q_a is almost constant till the fifteenth pulse i.e. the amount of desorbed hydrogen becomes constant. No increase in the residual hydrogen is detected in the sample after applying these charging conditions which indicates that there are no detected irreversibly absorbed hydrogen atoms under the detection limits of the hot extraction analyser.

- Increasing the charging duration to 3 minutes, the reversibly as well as the irreversibly trapped hydrogen atoms increase.

- Lowering the charging pulse potential to -1.2 V and -1.5 V, a highly reproducible hump appears in the current/time transients. This is may be due to the desorption of hydrogen from two different reversible trapping sites. Also, the reversibly absorbed hydrogen increases by lowering the applied charging pulse potential. At the same time, more hydrogen is irreversibly trapped in the amorphous Zr-based alloy.

- The amount of the reversible hydrogen of the multi-phase crystalline alloy is higher than that of the amorphous alloy. Maybe hydrogen absorption is more induced on the surface of the multi-phase crystalline alloy than on the amorphous alloy, since the amorphous alloy has a high electrocatalytic activity towards the hydrogen evolution reaction as was discussed before from the potentiodynamic polarisation measurements (see 5.1.1).

- The amount of the reversible hydrogen (q_a) of the amorphous $Zr_{55}Cu_{30}Al_{10}Ni_5$ is higher than that of the amorphous $Zr_{65}Cu_{17.5}Al_{7.5}Ni_{10}$. The $Zr_{65}Cu_{17.5}Al_{7.5}Ni_{10}$ alloy showed before (subchapter 4.1) slower hydrogen absorption rate and in subchapter 5.1.1 a higher electrocatalytic activity towards the hydrogen evolution reaction than the $Zr_{55}Cu_{30}Al_{10}Ni_5$ alloy, although it contains more Zr and Ni (good hydrogen absorbers) and less Cu (high electrocatalyst for hydrogen evolution) than the $Zr_{55}Cu_{30}Al_{10}Ni_5$ alloy.
- The presence of oxygen reduces the amount of the reversible hydrogen. This may be due to the occupation of some interstitial sites by oxygen which also hydrogen may prefer to occupy. Therefore, it hinders the absorption of more hydrogen and/or it reduces the surface activity towards hydrogen absorption.

5.4 Hydrogen diffusion

5.4.1 Diffusion in amorphous and crystalline phases

The diffusivity of hydrogen in Zr-Cu-Ni-Al metallic glasses was measured by means of the permeation test discussed in subchapter 3.5.3. The diffusion coefficient of hydrogen (D_*) was estimated for $Zr_{55}Cu_{30}Al_{10}Ni_5$ and $Zr_{65}Cu_{17.5}Al_{7.5}Ni_{10}$ ribbons containing 0.13 at.% oxygen. The values are tabulated in table 5.5. Those values of D_* reveal the high mobility of hydrogen in the Zr-Cu-Al-Ni metallic glasses, when they are compared with the D_* of hydrogen in pure crystalline palladium [19], and they are even higher than the D_* of hydrogen in metallic glass palladium alloys, e.g. $Pd_{77.5}Cu_6Si_{6.5}$ metallic glass [18] (see table 5.5).

Table 5.5: The diffusion coefficient estimated by means of the permeation technique of amorphous $Zr_{55}Cu_{30}Al_{10}Ni_5$ and $Zr_{65}Cu_{17.5}Al_{7.5}Ni_{10}$ samples for different conditions and compared with palladium alloys.

Alloy	D_** 10^{-11}, m^2/s
$[Zr_{55}Cu_{30}Al_{10}Ni_5]_{99.87}O_{0.13}$	2.6
$[Zr_{65}Cu_{17.5}Al_{7.5}Ni_{10}]_{99.87}O_{0.13}$	2.1
pure crystalline Pd	3.3
amorphous $Pd_{77.5}Cu_6Si_{6.5}$	0.2
$Zr_{55}Cu_{30}Al_{10}Ni_5$ precharged at -1 mA/cm^2 for 11 minutes	0.66
$[Zr_{65}Cu_{17.5}Al_{7.5}Ni_{10}]_{99.18}O_{0.82}$	1.3

For the two amorphous alloy compositions, $Zr_{55}Cu_{30}Al_{10}Ni_5$ and $Zr_{65}Cu_{17.5}Al_{7.5}Ni_{10}$ with the same oxygen content, the hydrogen diffusivity of $Zr_{55}Cu_{30}Al_{10}Ni_5$ alloy is slightly higher than that of $Zr_{65}Cu_{17.5}Al_{7.5}Ni_{10}$ alloy. This reveals the similarity of the structure of the amorphous ribbons and the similarity of interstitial sites for both Zr-Cu-Al-Ni compositions.

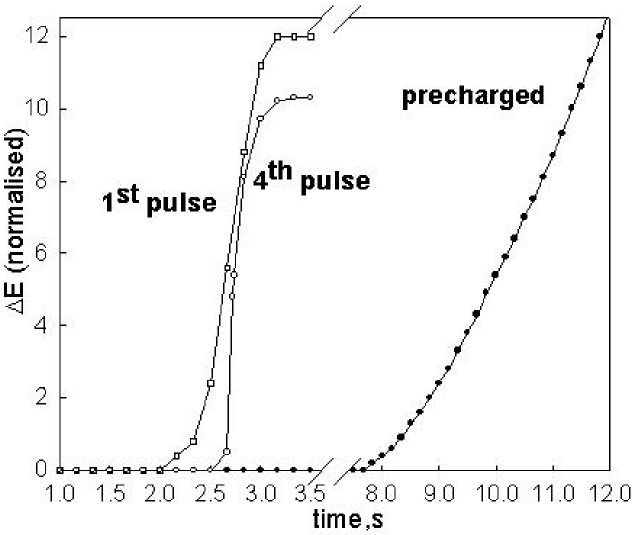

Figure 5.19: Voltage transients measured at the detection side for different charging current pulses and for a precharged sample, the scale of the change of potential (ΔE) has been normalised.

After applying several charging pulses of two to five seconds, the time lag for hydrogen to reach the detection side increases. Also the $Zr_{55}Cu_{30}Al_{10}Ni_5$ hydrogen-precharged sample at -1 mA/cm^2 for 11 minutes exhibits a longer time lag. This behaviour is observed for both compositions. Fig. 5.19 shows the voltage transients measured for uncharged $Zr_{55}Cu_{30}Al_{10}Ni_5$ samples at the detection side for the first and the fifth current pulses and also for the precharged sample. According to table 5.5, D_* of the precharged sample is lower than the uncharged sample. This reduction in the D_* value after several pulses and after precharging can be understood in terms of presence of the residual hydrogen in the amorphous phase. In a way that, by applying several hydrogen charging pulses or by hydrogen precharging the sample hydrogen atoms are trapped in some interstitial units. This trapped hydrogen hinders the diffusing hydrogen atoms to diffuse through the amorphous structure. The occupation of some interstitial sites blocks these sites for further diffusing hydrogen atoms and/or may lead to a repulsive interaction between the diffusing hydrogen atoms and the hydrogen atoms occupying interstitial sites. Hence, both reasons may let the diffusing hydrogen atoms change their paths or to reduce their rate of diffusion in the sample.

One should mention reults by Berry and Pritchet [21] obtained for amorphous $Ni_{40}Zr_{60}$ metallic glass ribbons after charging to H/M=0.78. In this work, the diffusion coefficient of the charged sample was found to be higher than that of the uncharged sample. The authors related this increase in the hydrogen mobility in the charged sample to the volume expansion at such a high hydrogen concentration which was found to result in a 9 % volume increase. This dilatation of the amorphous $Ni_{40}Zr_{60}$ structure is available as free-volume promoting host diffusion.
In our case, the hydrogen in the precharged sample is sufficient only to occupy some of the

interstitial sites and does not result in a detectable volume expansion of the amorphous structure as the hydrogen concentration is too low.

The effect of oxygen on the mobility of hydrogen in the amorphous ribbon was studied by estimating the diffusion coefficient of $Zr_{65}Cu_{17.5}Al_{7.5}Ni_{10}$ metallic glass ribbons containing 0.82 at.% oxygen and comparing it to the estimated D_* of the $Zr_{65}Cu_{17.5}Al_{7.5}Ni_{10}$ sample containing 0.13 at.% oxygen. D_* of the sample with the high oxygen content was found to be lower than D_* of the sample with the low oxygen content (see table 5.5). It is assumed that such small concentrations of oxygen may occupy some interstitial sites in the amorphous structure and, hence, block or hinder the diffusion of hydrogen through these sites.

The product of the diffusion coefficient and the concentration of hydrogen atoms at the sample surface ($D_*^{1/2}C_0$) was estimated from the potentiostatic double pulse technique for the multi-crystalline phase and the amorphous $Zr_{55}Cu_{30}Al_{10}Ni_5$ samples at different charging potentials. A relation between the applied charging potential and $D_*^{1/2}C_0$ is shown in Fig. 5.20 for the multi-crystalline phase and the amorphous alloy. It is obvious that $D_*^{1/2}C_0$ for the amorphous sample is significantly higher than that of the crystalline sample.
This shows that the hydrogen diffusion in the amorphous alloy is higher than that in the crystalline alloy.

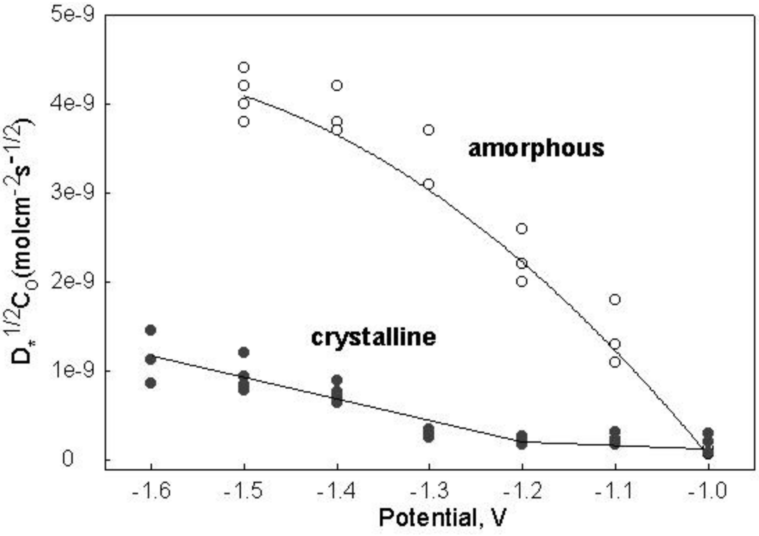

Figure 5.20: Relation between the applied charging potential and the product $D_*^{1/2}C_0$ for amorphous and multi-phase crystalline $Zr_{55}Cu_{30}Al_{10}Ni_5$ samples.

5.4.2 Conclusions

- The diffusivity of hydrogen in $Zr_{55}Cu_{30}Al_{10}Ni_5$ and $Zr_{65}Cu_{17.5}Al_{7.5}Ni_{10}$ metallic glass ribbons is high and shows no significant difference revealing the similarity in the amorphous structure and in the energy site distribution for both compositions.

- The diffusivity of hydrogen is reduced in the hydrogen precharged ribbons due to the occupation of some interstitial sites by hydrogen which hinders the diffusion of the diffusing hydrogen atoms to diffuse through the amorphous structure due to the blocking of these occupied sites and/or due to the repulsive interaction between the hydrogen atoms occupying the interstitial sites and the diffusing hydrogen atoms. This may reduce the mobility of the diffusing hydrogen atoms.
- Similarly, the presence of trace amounts of oxygen in the amorphous Zr-Cu-Al-Ni alloy lowers the diffusivity of hydrogen probably due to the blocking of some interstitial sites by oxygen atoms.
- The diffusion of hydrogen in the amorphous phase is significantly faster than the diffusion of hydrogen in the multi-crystalline phase.

Chapter 6

Conclusions

The glass forming Zr-Cu-Al-Ni alloy system is of great interest due to its high thermal stability (extended undercooled liquid region) and its ease of casting into bulk glassy shape. It contains early transition metals (Zr) and late transition metals (Ni), hence distorted short range order tetrahedra exist in the amorphous phase which are energetically favourable for hydrogen to occupy. All of these advantages make it a good target for hydrogen studies. The filling of these tetrahedral sites is according to its affinity to hydrogen in the following order : Zr_4, Zr_3Ni, Zr_2Ni_2, $ZrNi_3$ and finally Ni_4. From this point of view, hydrogen can be used as a sensitive probe to explore the amorphous structure.

In this work, electrochemically absorbed hydrogen was studied on amorphous $\mathrm{Zr_{55}Cu_{30}Al_{10}Ni_5}$ and $\mathrm{Zr_{65}Cu_{17.5}Al_{7.5}Ni_{10}}$ alloys at room temperature and the influence of the absorbed hydrogen on the stability of the amorphous phase, the thermal desorption and the crystallisation behaviour were investigated. Additionally, the cathodic hydrogen reaction mechanism on the surface of the amorphous alloy was investigated by cathodic polarisation tests. The reversibility of the absorbed hydrogen was studied by means of the absorption/desorption pulse technique and the mobility of hydrogen in the melt-spun material was studied. The effect of absorbed hydrogen on the crystallisation behaviour and the thermal stability of amorphous Zr-based alloys with different oxygen content was investigated.

It was found that multicomponent amorphous Zr-based alloys have the ability to absorb electrochemically large amounts of hydrogen exceeding a 1:1 hydrogen-to-metal ratio. But, hydrogen absorption induces a rearrangement in the amorphous matrix in a way that it increases the number of sites of high affinity to hydrogen. Therefore, at high hydrogen concentrations, copper-rich areas are detected on the surface. At the same time a depletion in the zirconium content on the surface due to the precipitation of fine zirconium hydride(s) takes place.

The thermal stability and the crystallisation behaviour of the Zr-based metallic glass strongly depend on the amount of hydrogen in the alloy. Already small amounts of hydrogen in the amorphous alloy cause a deterioration of its thermal stability, i.e. a diminution of the undercooled liquid region mostly resulting from a decrease of the crystallisation temperature.

The uncharged ribbons crystallise at 771 K by the formation of a mixture of a fcc-$\mathrm{NiZr_2}$ type metastable phase, orthorhombic NiZr and tetragonal $\mathrm{CuZr_2}$ phases. For a low H/M ratio of 0.37, a Cu and/or Cu-rich phase and a hexagonal $\mathrm{AlZr_2}$ phase form at 753 K, whereas for high

hydrogen contents of $0.7 < H/M < 1$ a cubic $AlCu_2Zr$ phase forms already at 713 K.
At high hydrogen contents ($H/M \geq 0.7$) the thermal stability of the alloy is determined by Zr-hydride formation and transformation to hydrogen-poorer phases accompanied by hydrogen effusion. The transformation to different hydride phases takes place in the order; tetragonal ε-Zr-hydride, cubic δ-Zr-hydride and a mixture of $(\alpha + \beta)$-Zr-hydrides.

For the $Zr_{65}Cu_{17.5}Al_{7.5}Ni_{10}$ alloy hydrogen suppresses the oxygen-triggered formation of the quasicrystalline intermediate phase upon heating. However, a significant excess of hydrogen atoms in the amorphous phase compared to the number of oxygen atoms is necessary to completely prevent the stabilisation of quasicrystals. This is maybe due to a sort of interaction which takes place between hydrogen and oxygen in the neighbouring interstitial sites. In contrast, the metastable fcc-type phase formation is obviously less affected by hydrogen.

The cathodic polarisation behaviour of amorphous Zr-Cu-Al-Ni alloys as derived from Tafel plots reveals three characteristic regions :
1 . In the Tafel region (low polarisation region), hydrogen discharge and adsorption (Volmer reaction) take place on the surface of the alloy as a fast step reaction followed by the rate-determining electrodic desorption step (Heyrowsky reaction) in competition with hydrogen absorption as a fast step.
2 . In the plateau region, the current density is independent of the potential as both the Volmer and the Heyrowsky reactions take place at the same rate and the hydrogen mass transfer from the solution to the electrode surface is the rate-determining step, i.e. the mechanism is diffusion controlled.
3 . In the high polarisation region, the cathodic current density increases. All the partial hydrogen reactions (hydrogen discharge, hydrogen electrodic desorption, hydrogen absorption and maybe also hydrogen chemical desorption) take place intensively, but it is difficult to define which reaction (Volmer reaction or Heyrowsky reaction) is predominant.
Multi-phase crystalline and single-phase amorphous Zr-based quaternary alloys exhibit the same hydrogen reaction mechanism. But the electrochemical activity of the amorphous alloy surface is higher than that of the multi-phase crystalline alloy. This maybe due to the fact that the amorphous alloy is a single-phase homogeneous material. Also, the amorphous alloy has a higher number of coordinatively unsaturated surface atoms. Thus, it can provide a high number of electrons for the hydrogen reduction and consequently, show a higher electrocatalytic activity.
The electrochemical activity of the surface of the amorphous $Zr_{65}Cu_{17.5}Al_{7.5}Ni_{10}$ alloy is higher than that of the $Zr_{55}Cu_{30}Al_{10}Ni_5$ alloy, as expressed in a way that the cathodic current density and the exchange current density of the amorphous $Zr_{65}Cu_{17.5}Al_{7.5}Ni_{10}$ are higher than those of the $Zr_{55}Cu_{30}Al_{10}Ni_5$ alloy. Also, the initial hydrogen absorption rate of the $Zr_{65}Cu_{17.5}Al_{7.5}Ni_{10}$ alloy is slower than that of the $Zr_{55}Cu_{30}Al_{10}Ni_5$ alloy and the estimated anodic charge from absorption/desorption tests is low in the case of the $Zr_{65}Cu_{17.5}Al_{7.5}Ni_{10}$ alloy, although the $Zr_{65}Cu_{17.5}Al_{7.5}Ni_{10}$ alloy has a higher Zr content (good hydrogen absorbers) and lower Cu content (good catalyst for hydrogen evolution reaction). It is assumed that, since the $Zr_{65}Cu_{17.5}Al_{7.5}Ni_{10}$ alloy has a higher Zr and Ni content, it has a higher surface coverage of adsorbed hydrogen atoms and this may increase the probability of the adsorbed hydrogen atoms to recombine.

The presence of less than 1 at.% of oxygen in the amorphous Zr-based alloys does not influence the mechanism of hydrogen reactions on the alloy surface, but it decreases the resistance of the alloy to the surrounding medium. The anodic charge of the absorption/desorption pulse test is significantly reduced when oxygen is present in the alloy maybe due to the occupation of oxygen to some interstitial sites which are favourable for hydrogen to occupy.

The polarisation behaviour of hydrogen precharged amorphous Zr-Cu-Al-Ni alloys shows a significant change of the Tafel parameters compared with the uncharged alloy. The mixed potential increases as Cu segregates on the alloy surface. The electrochemical reactivity also increases by increasing the hydrogen concentration in the amorphous Zr-based alloy. It might be that the filling of the interstitial sites in the amorphous phase by hydrogen reduces the affinity of the precharged samples towards hydrogen absorption and consequently enhances the hydrogen evolution reaction on the alloy surface. Also, Cu enrichment on the precharged samples can enhance the hydrogen evolution reaction rate.

The mechanism of the cathodic hydrogen reduction after hydrogen precharging changes in a way that in the Tafel region the fast hydrogen discharge step is followed by a rate-determining chemical desorption step and the current density plateau region, where the diffusion control mechanism takes place, is attained faster on the pre-hydrogenated samples than on the uncharged ones. In case of hydrogen precharged samples, the diffusion control mechanism is applied over a wider range of potential, i.e. the plateau region is more enhanced.

The reversibility of the absorbed hydrogen depends on the amount of hydrogen absorbed and the charging conditions. Under low charging pulse conditions, e.g. -1 V for 1 minute, hydrogen is reversibly desorbed from non-trapping sites possibly located very close to the entry sample surface. Increasing the number of pulses, more hydrogen is reversibly desorbed (q_a increases), possibly due to the reduction of a thin oxide layer. This increases the possibility of the absorbed hydrogen to occupy reversible trapping sites in the sample. After that the amount of the reversibly absorbed hydrogen that can be attained from the charge/discharge pulses is almost constant. No increase in the residual hydrogen was detected in the sample after applying these charging conditions. This indicates that there are no detected irreversibly absorbed hydrogen atoms under the detection limits of the hot extraction method.

Increasing the charging duration, the reversibility of the absorbed hydrogen increases and also irreversible trapping sites are occupied. Lowering the charging pulse potential to -1.2 V or -1.5 V, a highly reproducible hump appears in the current/time transients. This is maybe due to the desorption of hydrogen from two different reversible trapping sites. Also the amount of reversible hydrogen increases by lowering the applied charging pulse potential. At the same time, more hydrogen is irreversibly trapped in the amorphous Zr-based alloy.

The diffusivity of hydrogen in Zr-Cu-Al-Ni metallic glasses is high and shows no significant difference between the two studied alloy compositions revealing the similarity in the amorphous structure and the energy site distribution in both compositions.

The diffusivity of hydrogen is reduced in the pre-hydrogenated samples due to the occupation of some interstitial sites by hydrogen which hinders the diffusion of the diffusing hydrogen atoms to diffuse through the amorphous structure due to a blocking of these occupied sites and/or due to a repulsive interaction between the hydrogen atoms occupying the interstitial sites and the diffused hydrogen atoms. This may reduce the mobility of the diffusing hydrogen atoms.

Similarly, the presence of trace amounts of oxygen in the amorphous Zr-Cu-Al-Ni alloy lowers the diffusivity of the hydrogen probably due to the blocking of some interstitial sites by oxygen atoms.

The diffusion of hydrogen in the amorphous phase is significantly higher than the diffusion of hydrogen in the multi-crystalline phase.

Outlook

- More detailed investigations are needed to study the effect of hydrogen sorption on the Zr-Cu-Al-Ni metallic glasses. For example, the critical hydrogen concentration in the amorphous matrix at which volume expansion and rearrangement of the amorphous phase take place should be determined.
- A study of the gas phase sorption by means of pressure-composition isotherms should be performed.
- More detailed thermal desorption tests are needed. Also, the thermal stability and the crystallisation behaviour of the amorphous phase after hydrogen desorption should be performed.
- To reduce the effect of the readily formed oxide layer, the samples should be coated with a thin Pd layer before sorption tests. The effect of this coating needs to be studied.
- To increase the hydrogen absorption ability and the efficiency of hydrogen desorption of the Zr-Cu-Al-Ni metallic glasses, addition of other elements to the alloy is recommended, e.g. Pd.
- The corrosion behaviour in neutral and alkaline media needs to be carried out for the as-prepared ribbons and the hydrogen precharged samples.

Acknowledgements

This work would have not been possible to carry out without the help and the support of numerous people, scientists and technicians, from the Institut für Festkörper- und Werstofforschung Dresden (IFW). I would like to thank:

Specially and deeply Prof. Ludwig Schultz for suggesting and supporting such an interesting topic, his interest in this work and stimulating discussions.
Dr. Annett Gebert for supervision of this work, her help in experimental concerns specially melt-spun ribbons preparation and the useful discussions.
Dr. Margitta Uhlemann for effective cooperation, intensive discussions, good team work and good atmosphere.
Dr. Jürgen Eckert for the rich and fruitful discussions that have been decisive for this work.
Dr. Kurt Mummert for his support, help and discussion contribution.
Dr. Frank Schneider for his wealthy discussions.
Frank Schurack for his good advises and his help with all possible problems with the DSC and XRD. To Birgit Bartusch for her help and pleasant atmosphere.

I would like to thank my colleagues who are and also who were in the IFW Dresden, Dr. Ulrike Wolff, Britta Schlüter, Dr. Gabriele Barkleit, Dr. Martin Heilmaier, Dr. Ahmed Aziz, Dr. Norbert Mattern, Dr. Heike Schlörb, Dr. Oliver Gutfleisch, Dr. Alexandera Leonhard, Kirstin Buchholz, Stefano Deledda, Alberto Bollero, Uta Kühn, Holger Saage, Andreas Gümbel, Dr. Uta Grundmann, Michel Nganbe, Dr. Jens Freudenberger, Dr. Nicole Schlorke-de Boer, Dr. Bernd de Boer, Monika Herrich, Dr. Gert Jaeger, Golden Kumar, Ines Börner, Julia Lyubina and Nadja Kozlova.

I want to thank the persons who helped in carrying out some measurements: Dr. Stefan Baunack for AES measurements. Dr. Albert Güth for SEM measurements; Dr. Jürgen Thomas and Christine Mickel for TEM measurements; Dr. Wolfgang Gruner for oxygen analysis.

I am grateful to the technicians: deeply and specially Kerstin Hennig; Gesine Kreutzer; Marion Johne; Heike Kempe; Heiko Schulze and Heike Busskamp.

I want to thank all the people who supported me in the National Research Center Cairo (NRC) specially Prof. Sayed Mostafa, Prof. Kowther el Sobki and Dr. Neveen Abdel Latif.

Finally I am deeply grateful to my nice parents and good sisters and brother for their support and looking after my son during my stay in Germany and my lovely son Mahmoud for his patience and good understanding in spite of his young age.

References

[1] *Materials Science of Amorphous Metals*, ed. by T. Masumoto (Ohm Pub., Tokyo 1982).

[2] *Rapidly Solidified Alloys*, ed. by H. Liebermann (Marcel Dekker, Inc., New York 1993).

[3] H. A. Davies, in *Amorphous Metallic Alloys*, ed. by F. Luborsky (Butterworth Monographs in Materials, London 1983).

[4] H. Chen, Non-crystalline structure in solidified gold-silicon alloys, Rep. Prog. Phys. **43**, 353 (1980).

[5] W. Klement Jr., R. Willens, and P. Duwez, Non-crystalline structure in solidified gold-silicon alloys, Nature **187**, 869 (1960).

[6] A. Inoue, M. Kohinata, A. Tsai, and T. Masumoto, Mg-Ni-La amorphous alloys with a wide supercooled liquid region, Mater. Trans. JIM **30**, 378 (1989).

[7] A. Inoue, T. Zhang, and T. Masumoto, Zr-Al-Ni amorphous alloys with high glass transition temperature and significant supercooled liquid region, Mater. Trans. JIM **31**, 177 (1990).

[8] T. Zhang, A. Inoue, and T. Masumoto, Amorphous Zr-Al-TM (TM=Co, Ni, Cu) alloys with significant supercooled liquid region of over 100 K, Mater. Trans. JIM **32**, 1005 (1991).

[9] W. L. Johnson, Bulk glass-forming metallic alloys: Science and technology, MRS Bulletin **24**, 42 (1999).

[10] A. Inoue, High strength bulk amorphous alloys with low critical cooling rates (overview), Mater. Trans. JIM **36**, 866 (1995).

[11] H. Choi-Yim, R. Busch, and W. L. Johnson, The effect of silicon on the glass forming ability of the $Cu_{47}Ti_{34}Zr_{11}Ni_8$ bulk metallic glass forming alloy during processing of composites, J. Appl. Phys. **83**, 7993 (1998).

[12] A. Inoue, T. Shibata, and T. Zhang, Effect of additional elements on glass transition behavior and glass formation tendency of Zr-Al-Cu-Ni alloys, Mater. Trans. JIM **36**, 1420 (1995).

[13] A. Inoue and T. Zhang, Fabrication of bulk glassy $Zr_{55}Al_{10}Cu_{30}Ni_5$ alloy of 30 mm diameter by a suction casting method, Mater. Trans. JIM **37**, 185 (1996).

[14] N. Mattern, J. Eckert, M. Seidel, U. Kühn, S. Doyle, and I. Bächer, Relaxation and crystallisation of amorphous $Zr_{65}Al_{7.5}Cu_{17.5}Ni_{10}$, Mater. Sci. Eng. **A226-228**, 468 (1997).

[15] A. Gebert, J. Eckert, and L. Schultz, Effect of oxygen on phase formation and thermal stability of slowly cooled $Zr_{65}Al_{7.5}Cu_{17.5}Ni_{10}$ metallic glass, Acta mater. **46**, 5475 (1998).

[16] J. Eckert, N. Mattern, M. Zinkevitch, and M. Seidel, Crystallisation behavior and phase formation in Zr-Al-Cu-Ni metallic glass containing oxygen, Mater. Trans. JIM **39**, 623 (1998).

[17] A. Gebert, J. Eckert, H. D. Bauer, and L. Schultz, Characteristics of slowly cooled Zr-Al-Cu-Ni bulk samples with different oxygen content, Mater. Sci. Forum **269-272**, 797 (1998).

[18] R. Kirchheim, F. Sommer, and G. Schluckebier, Hydrogen in amorphous metals-I, Acta Metall. **30**, 1059 (1982).

[19] R. Kirchheim, Solubility, diffusivity and trapping of hydrogen in dilute alloys, deformed and amorphous metals-II, Acta Metall. **30**, 1069 (1982).

[20] J. O. Ström-Olsen, Y. Zhao, D. H. Ryan, Y. Huai, and R. W. Cochrane, Hydrogen diffusion in amorphous Ni-Zr, J. Less-Common Metals **167**, 923 (1991).

[21] B. S. Berry and W. C. Pritchet, Host and hydrogen diffusion in an Ni-Zr metallic glass, Mater. Sci. Eng. **97**, 419 (1988).

[22] M. Ciureanu, D. H. Ryan, J. O. Ström-Olsen, and M. L. Trudeau, Electrochemical studies of hydrogen storage in amorphous $Ni_{64}Zr_{36}$ alloy, J. Electrochem. Soc. **140**, 579 (1993).

[23] A. J. Maeland, in *Comparison of Hydrogen Absorption in Glassy and Crystalline Structures, in Hydrides for energy storage*, ed. by A. F. Andresen, A. J. Maeland, and Jr. (Pergamon, Oxford 1978).

[24] F. Spit, K. Blok, G. Hendriks, W. Turkenburg, J. W. Drijver, and S. Radelaar, Kinetics of hydrogen sorption in some metallic glasses and surface investigation of the metallic glass $Ni_{64} - Zr_{36}$, Proc. 4th Int. Conf. on Rapidly Quenched Metals 1635 (1981).

[25] K. Aoki, M. Kamachi, and T. Masumoto, Thermodynamics of hydrogen absorption in amorphous Zr-Ni alloys, J. Non-Cryst. Solids **61/62**, 679 (1984).

[26] K. Suzuki, N. Hayashi, Y. Tomisuza, T. Fukunaga, and K. Kai, Hydrogen atom environments in a hydrogenated Zr-Ni glass, J. Non-Cryst. Solids **61/62**, 637 (1984).

[27] E. Batalla, Z. Altounian, D. B. Boothroyd, R. Harris, and J. O. Ström-Oslen, in *Hydrogen in disordered and amorphous solids*, ed. by G. Bambakidis, R. C. Bowman, and Jr. (Plenum Press, New York 1986).

[28] J. H. Harris, W. A. Curtin, and M. A. Tenhover, Universal features of hydrogen absorption in amorphous transition-metal alloys, Phys. Rev. B **36**, 5784 (1987).

[29] J. H. Harris, W. A. Curtin, and L. Schultz, Hydrogen storage characteristics of mechanically alloyed amorphous metals, J. Mater. Res. **3**, 872 (1988).

[30] T. Jang, S. M. Lee, and J. Y. Lee, The change of hydrogen distribution behaviour in amorphous $Ni_{64}Zr_{36}$ resulting from the hydrogen absorption, Scripta Metall. **25**, 659 (1991).

[31] T. Araki, T. Abe, and K. Tanaka, Site energy distribution of hydrogen in Ni-Zr alloy studied by thermal desorption spectrometry, Mater. Trans. JIM **30**, 748 (1989).

[32] I. Nagy, I. Bakonyi, A. Lovas, E. Tòth-Kàdàr, K. Tompa, M. Hossò, À. Cziràki, and B. Fogarassy, Hydrogen sorption and hydrogen-induced phase separation in a nearly equiatomic Ni-Zr amorphous alloy, J. Less-Common Metals **167**, 283 (1991).

[33] I. Bakonyi, E. Tòth-Kàdàr, I. Nagy, K. Tòth, K. Tompa, A. Lovas, À. Cziràki, B. Fogarassy, and G. Wiesinger, Hydrogen absorption and hydrogen-induced phase-separation in amorphous $Zr_{50}Ni_{50-x}Cu_x$ alloys, Z. Phys. Chem. **183**, 87 (1994).

[34] S. Spriano, M. Baricco, C. Antonione, F. Rosalbino, and P. Spinelli, Electrocatalytic behaviour of $Zr_{64}Ni_{36}$ and $Zr_{48}Ni_{27}Al_{25}$ amorphous alloys, Electrochimica Acta **39**, 1781 (1994).

[35] N. Eliaz, D. Eliezer, E. Abramov, D. Zander, and U. Köster, Hydrogen evolution from Zr-based amorphous and quasicrystalline alloys, J. Alloys Comps. **305**, 272 (2000).

[36] J. Tòth, J. Garaguly, K. Tompa, A. Lovas, and L. K. Varga, Hydrogen uptake monitored by resistance change in amorphous $Zr_{33}Ni_{67}$ alloy, Int. J. Hydrogen Energy **21**, 1039 (1996).

[37] Y. Yamada and K. Tanaka, Electrical resistivity during hydrogen charging and subsequent heating in Zr-Ni alloy glasses, Trans. Japan Inst. Metals **27**, 409 (1986).

[38] D. Zander, U. Köster, N. Eliaz, D. Eliezer, and D. Plachke, Influence of hydrogen on the thermal stability of Zr-based quasicrystals, Mat. Res. Soc. Symp. Proc. **553**, 49 (1999).

[39] B. I. Wehner, J. Meinhardt, U. Köster, H. Alves, N. Eliaz, and D. Eliezer, Oxidation and hydrogenation of quasicrystals, Mater. Sci. Eng. **A226/228**, 1008 (1997).

[40] D. A. Porter and K. E. Easterling, *Phase Transformations in Metals and Alloys*, 2nd ed. (Chapman and Hall 1992).

[41] C. Janot, *Quasicrystals*, 2nd ed. (Clarendon Press, Oxford 1994).

[42] D. R. Uhlmann, A kinetic treatment of glass formation, J. Non-Cryst. Solids **7**, 337 (1972).

[43] J. Zarzycki, in *Glasses and Amorphous Materials (Materials Science and Technology, Vol. 9)*, ed. by R. W. Cahn, P. Haasen, and E. J. Kramer (1991).

[44] P. Ramachandrarao, B. Cantor, and R. W. Cahn, Viscous behaviour of undercooled liquid melts, Acta Metall. **24**, 109 (1977).

[45] H. Scholze, *Glas : Natur, Struktur, und Eigenschaften* (Spring-Verlag 1988).

[46] S. R. Elliott, *Physics of Amorphous Materials*, 2nd ed. (Longman Scientific and Technical, Inc., New York 1990).

[47] C. A. Angell, Relaxation in liquid, polymers and plastic crystals-strong/fragile patterns and problems, J. Non-Cryst. Solids **131-133**, 13 (1991).

[48] C. A. Angell, Formation of glasses from liquids and biopolymers, Front. Mater. Sci. **276**, 1924 (1995).

[49] A. Inoue, Recent progress of Zr-based amorphous alloys, Sci. Rep. RITU **A42**, 1 (1996).

[50] M. H. Cohen and D. Turnbull, Composition requirements for glass formation in metallic and ionic systems, Nature **189**, 131 (1961).

[51] P. J. Desrè, On the effect of the number of components on glass-forming ability of alloys from the liquid states: Application of the new generation of multicomponent bulk glasses, Mater. Trans. JIM **38**, 583 (1997).

[52] A. Inoue, H. Yamaguchi, T. Zhang, and T. Masumoto, Al-La-Cu amorphous alloys with a wide supercooled liquid region, Mater. Trans. JIM **31**, 104 (1990).

[53] A. Peker and W. L. Johnson, A highly processable metallic glass: $Zr_{41.2}Ti_{13.8}Cu_{12.5}Ni_{10.0}Be_{22.5}$, Appl. Phys. Lett. **63**, 2342 (1993).

[54] H. H. Liebermann, The dependence of the geometry of glassy alloy ribbons on the chill block melt-spinning process parameters, Mater. Sci. Eng. **43**, 203 (1980).

[55] P. Ramachandrarao, M. Laridjani, and R. W. Cahn, Diamond as a splat-cooling substrate, Z. Metallk. **63**, 43 (1972).

[56] S. Miller and R. Murphy, A gas-water atomization process for producing amorphous powders, Scripta Metall. **13**, 673 (1979).

[57] J. S. Benjamin and T. E. Volin, The mechanism of mechanical alloying, Mater. Sci. Forum **5**, 1929 (1974).

[58] E. Hellstern and L. Schultz, Amorphization of transition metal Zr alloys by mechanical alloying, Appl. Phys. Lett. **48**, 124 (1986).

[59] J. Eckert and L. Schultz, in *Topics in Applied Physics*, ed. by C. Beck and H. J. Güntherodt (Spring-Verlag Berlin 1994).

[60] J. Eckert, Mechanical alloying of bulk metallic glass forming systems, Mater. Sci. Forum **312-314**, 3 (1999).

[61] G. K. Wehner and G. S. Anderson, *Handbook of Thin Film Technology* (McGraw-Hill, New York 1970).

[62] H. J. Leamy and A. G. Dirks, The microstructure of amorphous rare-earth/transition-metal thin films, J. Phys. D **10**, L95 (1977).

[63] T. Watanabe and Y. Tanabe, Formation and morphology of Ni-B amorphous alloy deposited by electroless plating, Mater. Sci. Eng. **23**, 97 (1976).

[64] *The Metal-Hydrogen System*, ed. by U. Gonser (Springer-Verlag 1992).

[65] A. Sieverts, , Z. Phys. Chem. **60**, 129 (1907).

[66] G. G. Libowlitz, *Sloid-State Chemistry of Binary Metal Hydrides* (Benjamin, New York 1965).

[67] K. M. Mackey, *Hydrogen compounds of metallic elements* (Spon, London 1965).

[68] H. Kaneko, T. Kajtani, M. Hirabayashi, M. Ueno, and K. Suzuki, Hydrogen and deuterium atoms in amorphous Zr-Ni alloys, J. Less-Common Metals **89**, 237 (1983).

[69] K. Suzuki, Structures and properties of amorphous metal hydrides, J. Less-Common Metals **89**, 183 (1983).

[70] K. Samwer and W. L. Johnson, Structure of glassy early-transition-metal–late-transition-metal hydrides, Phys. Rev. B **28**, 2907 (1983).

[71] R. Kirchheim, Hydrogen solubility and diffusivity in defective and amorphous metals, Prog. Mater. Sci. **32**, 261 (1988).

[72] C. Wagner, The activity coefficient of oxygen and other nonmetallic elements in binary liquid alloys as a function of alloy composition, Acta Metall. **21**, 1297 (1973).

[73] C. M. A. Brett and A. M. O. Brett, *Electrochemistry Principles, Methods, and Applications* (Oxford University Press 1992).

[74] R. Kirchheim, Influence of disorder on the diffusion of alkali ions in SiO_2- and GeO_2-glasses, J. Non-Cryst. Solids **55**, 243 (1983).

[75] R. Kirchheim and U. Stolz, Monte-carlo simulations of interstitial diffusion and trapping-II. amorphous metals, Acta Metall. **35**, 291 (1987).

[76] R. C. Brouwer, E. Salomons, and R. Griessen, Diffusion of hydrogen in $Nb_{1-y}V_y$ alloys, Phys. Rev. B **38**, 10217 (1988).

[77] H. J. Güntherodt, Introduction to rapidly solidified materials, Proc. 5th Int. Conf. on Rapidly Quenched Metals 1591 (1984).

[78] B. G. Pound, in *Modern Aspects of Electrochemistry*, ed. by J. O. M. Bockris et al. (Plenum Press, New York 1993).

[79] R. McKibben, R. M. Sharp, D. A. Harrington, B. G. Pound, and G. A. Wright, A potentiostatic double-step method for measuring hydrogen atom diffusion and trapping in metal electrodes –I. theory, Acta Metall. **35**, 253 (1987).

[80] J. O. M. Bockris, M. A. Genshaw, and M. Fullenwider, The electro-permeation of hydrogen into metals, Electrochimica Acta **15**, 47 (1970).

[81] M. A. V. Devanathan and Z. Stachurski, The adsorption and diffusion of electrolytic hydrogen in palladium, Proc. R. Soc. London **A270**, 90 (1962).

[82] B. D. Cullity, *Elements of X-Ray Diffraction*, 2nd ed. (Addison-Wesley Publishing Company, Inc. 1978).

[83] E. Zuzek, J. Abriata, A. San-Martin, and F. Manchester, in *Binary Alloy Phase Diagrams, Vol. 2*, 2nd ed., ed. by T. B. Massalski, H. Okamoto, P. Subramanian, and L. Kacprzak (William W. Scott, Jr. 1990).

[84] H. E. Kissinger, Reaction kinetics in differential thermal analysis, Anal. Chem. **29**, 1702 (1957).

[85] S. Yamanaka, Y. Fujita, M. Uno, and M. Katsura, Influence of interstitial oxygen on hydrogen solubility in metals, J. Alloys Comps. **293-295**, 42 (1999).

[86] N. Ismail, M. Uhlemann, A. Gebert, and J. Eckert, Hydrogenation and its effect on the crystallisation behaviour of $Zr_{55}Cu_{30}Al_{10}Ni_5$ metallic glass, J. Alloys Comps. **298**, 146 (2000).

[87] N. Ismail, A. Gebert, M. Uhlemann, J. Eckert, and L. Schultz, Effect of hydrogen on $Zr_{65}Cu_{17.5}Al_{7.5}Ni_{10}$ metallic glass, J. Alloys Comps. **314**, 170 (2001).

[88] M. Pourbaix, *Atlas of electrochemical equilibria in aqueous solutions* (Pergamon Press 1966).

[89] J. O. M. Bockris and A. K. N. Reddy, *Modern Electrochemistry . 2* (Plenum Press, New York 1970).

[90] J. O. M. Bockris and R. Thacker, Tech. Report #3, NR 036-028 **ONR 551 (22)**, Office of Naval Research (December 31, 1959).

[91] J. O. M. Bockris and M. A. V. Devanathan, The determination of the coverage of nickel and steel during electrolytic hydrogen evolution, Tech. Report #4, NR 036-028 Office of Naval Research (February 28, 1961).

[92] M. Naka, K. Hashimoto, T. Masumoto, and I. Okamoto, Cathodic characteristics of amorphous metal-metal alloys in sulfuric acid solution, Proc. 4th Int. Conf. on Rapidly Quenched Metals 1431 (1981).

[93] B. G. Pound, G. A. Wright, and R. M. Sharp, A potentiostatic double-step method for measuring hydrogen atom diffusion and trapping in metal electrodes–II. experimental, Acta Metall. **35**, 263 (1987).